Important Notice

This copy may be used only for the purposes of research and private study, and any use of the copy for a purpose other than research or private study may require the authorization of the copyright owner of the work in question. Responsibility regarding questions of copyright that may arise in the use of this copy is assumed by the recipient.

UNIVERSITY OF CALGARY

Processing and simulation of Distributed Acoustic Sensing (DAS) data acquired from a multicomponent fiberoptic sensor

by

Carla Daniela Acosta Sira

A THESIS

SUBMITTED TO THE FACULTY OF GRADUATE STUDIES IN PARTIAL FULFILMENT OF THE REQUIREMENTS FOR THE DEGREE OF MASTER OF SCIENCE

GRADUATE PROGRAM IN GEOSCIENCE

CALGARY, ALBERTA

SEPTEMBER, 2025

© Carla Daniela Acosta Sira 2025

Abstract

This thesis explores the feasibility, performance, and interpretability of Distributed Acoustic Sensing (DAS) seismic data, acquired in an experimental, shaped, deployment. This research addresses one of the main limitations of DAS—its directionality and lack of sensitivity to broadside seismic energy—by testing a novel, low-cost, permanent, multi-component DAS sensor array referred to as the Croissant. The Croissant consists of three sensors, each consisting of fiber wrapped around two 1x1m vertical plastic frames set at right angles. In this thesis I investigate whether the integration of compact, point-based multicomponent sensors of this kind into otherwise single-component DAS systems can overcome directional limitations and enhance seismic monitoring, while preserving the cost-effectiveness of the technology. The study is based on multi-year field data recorded between 2023 and 2025 at the Carbon Management Canada (CMC) Newell County facility using a P-wave vibrator along a circular source line. This experimental dataset enables the analysis of the Croissant's response to a wide range of azimuths and offsets, allowing for an evaluation of its directional sensitivity. Initial observations showed consistently strong vertical responses, leading to the hypothesis that refracted waves may be arriving with dominant vertical energy. To test this hypothesis, a geometric DAS model was developed by parameterizing the Croissant's fiber trajectory according to its physical design and wrapping pattern. Synthetic shot gathers were generated using both an analytical model and a 3D elastic finite-difference simulation (ElasWave3D) and compared with co-located geophone measurements for validation. Results showed strong agreement between synthetic and field data: the Croissant reliably captured vertical and horizontal strain, and amplitude decay followed expected trends. Synthetic geophone data supported the interpretation of refracted energy in the experimental DAS recordings. The findings support the Croissant's effectiveness as a point-based, multicomponent DAS sensor. Improvements in signal clarity observed from 2023 to 2025 likely reflect improved sensor coupling due to soil compaction. While each sensor currently uses ~28 meters of fiber using a gauge length of 7 meters, early results suggest that could be reduced to ~14 meters under certain conditions. Co-located geophones provided critical reference data, reinforcing the directional trends and validating the Croissant DAS wave field interpretations.

Acknowledgements

Firstly, I want to thank God for guide, enlighten, and protect my path. Thanks for putting the right people and circumstances to serve, help, learn, reflect, and achieve my goals. Thanks for my family, my friends, people I have met, the journey and dreams that have brought me here. It has been amazing!

I want to thank my mother and father for all they have done. All that you are, makes who I am. I am proud of you and grateful, always, because despite the difficulties, you did and are doing your best. Thank you for your energy, for supporting me, believing in me and being with me. I love you.

I want to thank my brother, Carlos, for existing and motivate me everyday to be a better person. I love you.

I want to thank my lovely partner, Amilcar, for being unconditionally during this journey. These two years have been lighter with your presence, love and energy. Thank you for having my home full of beautiful flowers all year round, even in the harsh winters. I love you.

I want to thank my uncles, and cousins for their invaluable support and love, all of you recharge and inspire me every day. I love you.

I want to thank my friends for their support, love, energy, and joy! I love you.

I want to thank Kris Innanen for give me the opportunity to be part of CREWES. It has been a valuable and enriching experience. Thank you for trusting me; I will be always grateful to you.

I want to thank Kevin Hall for all the contributions on this work, his time, suggestions, guidance, and willingness to help during this journey. I will be always grateful to you.

I want to thank Iván Sánchez, for all the contributions in this work, the valuable conversations and insights on seismology and numerical methods, and his willingness to teach and help. Thank you for your patience, for guiding and supporting me; I appreciate it always. Your contributions wherever you are, I am sure, exceed expectations and help others to give the best of themselves. I will always be grateful to you.

I want to thank Joe Wong for his wiliness to help, guide, teach and contribute positively to my project. I will always be grateful to you.

I want to thank David Henley for reviewing and editing my project. Thank you for your valuable time, your knowledge and your willingness to help. Your curiosity and questions helped me to improve my work. I will always be grateful to you.

Kevin Beltram, thank you for always say hi when you passed in front of my desk, your daily small talks, and energy! I appreciate it.

I want to thank Jan Dettmer, Daniel Trad, Brandon Karchewski, Marc Strous and Christopher Clarkson for the valuable classes taught and the willingness to support. Daniel Trad, thank you for your responsiveness, willingness to listen and help. I appreciate it.

I want to thank Hersh Gilbert, and Daniel Trad again for being part of the thesis committee, for your time reviewing my project and your insightful questions. I appreciate it.

I want to thank my CREWES-colleagues, Angel Ramos, Ziguang Su, Arvin Karpiah, Anton Ziegon, David Emery, Kim Pike, Paloma Lira, Tianze Zhang, Jinji Li, Xiaohui Cai, Chioma Chineke, Scott Hess, and Christina Schumacher for their good energy, insightful conversations, the invaluable support, and willingness to help.

I want to thank to Bernabe Aguado, Lee Hunt, Meaghan Wright, my valuable mentors. Bernabe, thank you for making me believe in myself and encourage me to follow my dreams as a geophysicist; which needed to be abroad being a dreamer in Venezuela; thank you for your support, willingness to help and your words. Lee, many thanks for your guidance, help, and support throughout this year; it has been invaluable. I truly appreciate your time and your curiosity about my project. Your thoughtful questions and insights challenged me to explore new perspectives. Meaghan, thank you for your time and support my first year in Calgary; you were a safe place for me during those times. Bernabe, Lee and Meaghan, I will always be grateful to you.

To my Venezuelan colleagues, Marivi, Raul, Gabriel, Adriana, Mariana, Oscar, Joaquin, Ninoska, Michelle, Patricia, Virginia, Reinaldo, and Mafer, thanks for the good energy, the support and the willingness to help. I will always be grateful to you.

I want to thank Joanna Cooper, and Carbon Management Canada staff for the data provided and the responsiveness.

I want to thank all the CREWES sponsors for their continuing support.

Thanks for all the contributions!

Dedication

To my past,

To my present,

To my future!

Table of Contents

Abstract	ii
Acknowledgements	. iii
Dedication	v
Table of Contents	. vi
List of Figures	. ix
List of Tables	XX
1. CHAPTER 1 – INTRODUCTION	21
1.1 Conventional sensors – geophones and seismometers	21
1.2 Fiberoptic sensor – Distributed Acoustic Sensing (DAS)	22
1.3 Challenges with DAS	23
1.4 DAS in seismic	24
1.5 Thesis overview and objectives	25
2. CHAPTER 2: DAS Foundations and Principles	29
2.1 Fiber optics in the telecommunications industry	29
2.2 DAS Principles	30
2.3 DAS System Components	31
2.3.1 The fiber	31
2.3.2 Fiber Deployment Methods – Surface	32
2.3.3 Interrogator unit and gauge length	33
2.3.4 Measurement of the fiber	35
2.4 Mathematical definition of strain	36
2.5 Strain and strain rate measured by the fiber	39
2.6 DAS spatial parameters	41

	2.6.1	Spatial Sample Location / Sample Location Number	41
	2.6.2	Fiber Distance and Spatial Sampling Interval	41
	2.6.3	Gauge Length and spatial resolution	41
	2.6.4	Supporting DAS signal parameters	42
	2.6.5	Sample Rate & Sample number	42
	2.6.6	Time Series	42
2.	.7 D	AS directionality and multicomponent sensing: previous work	43
3.	CHAP	TER 3. The seismic waves and events in surface datasets	49
3.	.1 B	ody waves	50
3.	.2 S	urface waves	52
3.	.3 R	efracted waves	52
3.	.4 G	seometric spreading and attenuation	55
4.	CHAP	TER 4: Experimental data Location and Acquisition	57
4.	.1 P	roject Location	57
4.	.2 G	eological Setting of the Study Area	57
4.	.3 Ir	ntroduction to data, acquisition, setting	59
	4.3.1	Croissant Data: Line 41 – P-Vibe	61
	4.3.2	Geophone Data: Line 41 – P-Vibe	63
4.	.4 D	Pata Processing	64
4.	.5 Q	Qualitative observations for Croissant data L41 - Hypothesis	64
5.	CHAP	TER 5. Analytical, geometrical and numerical model of the Croissan	t -
synthetic se	eismogra	ams	67
5.	.1 N	Methods for computing synthetic shot gathers	68
5.	.2 A	analytical Model – Homogeneous and isotropic medium (Innanen, 2017a)	69
	Experi	ment of broadside sensitivity – Straight and Helical fibers	70
			3 /11

5.3 Geometrical Model of the Croissant	72
5.4 Geometrical Model of the Croissant in 2-	layers medium
5.5 Numerical Model – Finite Difference 3D	Elastic Model 84
5.5.1 1st Simulation: Homogeneous half-spa	ce model (Ricker wavelet) 88
5.5.2 2 nd Simulation: homogeneous layered correlated wavelet)	• ,
6. CHAPTER 6: Amplitude response of the Croi	ssant97
6.1 Establish consistency of model and exper	rimental data97
6.2 Automatic first break picking for amplitu	nde analysis workflow 102
6.3 Amplitude analysis of the Croissant	104
6.3.1 Amplitude analysis from Finite Differen	ence Model109
6.3.2 Amplitude analysis from Experimenta	l data120
6.5 Signal to Noise Ratio Analysis	
6.5.1 Effects of Soil Compaction and Sweep	Count on SNR Improvement 133
6.5.2 Stacked traces vs SNR	
7. CHAPTER 7: Co-Located Geophone data	142
7.1 Amplitude Analysis for Co-located Geop	ohones 144
i. First Arrival Analysis – Co-located Geop	phone data145
ii. Surface Wave Analysis – Co-located Geo	ophone data148
Conclusions	
Future work	153
Bibliography	154
Appendix	162
Croissant Loop Path Function	162

List of Figures

FIG 2.1 Operation principle of distributed acoustic sensing (Shatalin et al., 2021) 30
FIG 2.2. Structure of a classical, cylindrically symmetric, glass-based optical fiber (extracted from SEAFOM, 2024)
FIG 2.3 Reflection at the core-cladding interface is total (extracted from Thevenaz, 2011)
FIG 2.4. Typical DAS strain measurement, over gauge length (Terra15, 2024) 34
FIG 2.5. Diagram to define strain. (a) It is a bar with length L at the beginning. (b) It is the
bar which has been altered by an applied stress P and is now length L+ δ (Mechanics of Slender
Structures, 2020)
FIG 2.6. Diagram to define shear strain. Deformation of an object is response to a shear
stress (i.e. parallel to a surface) (Mechanics of Slender Structures, 2020)
FIG 2.7. Displacement and strain in 3D (extracted from Krebes, 2019)
FIG 2.8. Straight optical fiber embedded in a cable (obtained from Kuvshinov, 2016) 39
FIG 2.9. DAS interrogator unit test arrangement (extracted from SEAFOM, 2024) 41
FIG 2.10. Signal parameters relating to Time Series and their Spatial Location
Identification (extracted from SEAFOM, 2024)
FIG 2.11. DAS with linear optical cable is more sensitive to P-wave in VSP configuration
and to S-wave in microseismic events (modified from Shatalin et al., 2021)
FIG 2.12. Overview of the developed DAS sensor: (a) photo of the DAS sensor. The frame
size is about 20–25 cm; the pipe diameter was 32 mm (extracted from Takekawa et al., 2022) . 47

FIG 3.1. Elastic deformations and ground particle motions associated with the passage of
body waves: (left) a P-wave; (right) an S-wave (extracted and modified from Kearey and Brooks
1987)50
FIG 3.2. Displacement (particle motion) for P-, SV-, and SH-waves with respect to the
propagation (ray) direction of the wave. P-wave particle motion is aligned with the ray direction;
SV and SH motion is orthogonal to the ray direction. SV motion occurs within a vertical plane
through the propagation vector (extracted from Shearer, 2019)
FIG 3.3. Elastic deformations and ground particle motions associated with the passage of
surface waves: (left) a Rayleigh wave; (right) a Love wave (extracted and modified from Kearey
and Brooks, 1987)
FIG 3.4. Successive positions of the expanding wavefronts for direct and refracted waves
through a two-layer model. Individual ray paths from source A to detector D are shown (Kearey
and Brooks 1987)
FIG 3.5. Travel-time curves for direct wave and the head wave from a single horizontal
refractor (Kearey and Brooks 1987) 55
FIG 3.6 Amplitude decay associated with geometric spreading (a) in a uniform material (b)
in a material whose velocity increases with depth (Obtained from O'DOHERTY and ANSTEY,
1971)
FIG 4.1. Geological Legend: 1) Pleistocene and Holocene (4.9 m KB) 2) Dinosaur Park
Formation/Bedrock Surface (29.5 m) 2a) Dinosaur Park Formation, Lethbridge coal zone top (29.5
m) 3) Dinosaur Park Formation, Lethbridge coal zone base (41.5 m) 4) Dinosaur Park, sandy zone
(46 m) 5) Oldman Formation (99 m)
FIG 4.2. DAS experimental data, where TN = straight fiber in northern trench, TH = helical
fiber in trench, TS = straight fiber in southern trench, OBS1 = straight fiber in observation well 1,
OBS2 = straight fiber in observation well 2, OBS2H = helical fiber in observation well 2, P =
pretzel data, and C = Croissant data (obtained from Hall et al., 2023)

FIG 4.3. Croissant experimental data (Zoomed view of Figure. 4.2), VP 13147, Foun
stacked and correlated sweeps (16 s sweep, 10-150 Hz) (obtained and modified from Hall et al.,
2023)
FIG 4.4. Map of field area showing test sweep locations on source lines 13 and 41 (left).
Details of the Pretzel (Two 10x10 m horizontal squares at 1.82 m depth; green) and Croissant
receiver stations 1, 2, and 3 $(0.15 - 1.15 \text{ m depth}; \text{ blue V's})$ locations are shown on the right
(obtained from Hall et al., 2023)
FIG 4.5. Sketch of the optic fiber cable wounded in the plastic frames
FIG 4.6. Schematic of Croissant install (cf. Figure 4.4). Vertical 1x1 m plastic frames were
installed at Croissant stations 2 (fiber wraps 1,2,3), 3 (fiber wraps 4,5,6) and 1 (fiber wraps 7,8,9).
Each Croissant component contains 28 m of fiber (4 x 7 m gauge length). Three-component
geophones were placed at the corners of the Croissant V's (orange squares) (obtained from Hall et
al., 2023)
FIG 4.7. Plan view of the Inova SM7 arrangement on the Croissant and Pretzel location.
FIG 4.8. Sketch of refracted ray path impinging on the Croissant with a vertical dominant
component (blue). Direct ray path impinging on the Croissant with a horizontal dominant
component (green)
FIG 5.1. (a) Straight and (b) helical fibers lying horizontally, in blue, close to a P-wave
source point (red circle). Red arrow points in the radial direction (between the source point and
any point on the fiber under consideration. In the second row, the shot gather of the straight (Fiber
1) and helical fiber (Fiber 2)
FIG 5.2. (a) Straight and (b) helical fibers laying vertically, in blue, close to a P-wave
source point (red circle). Red arrow points in the radial direction (between the source point and
any point on the fiber under consideration. In the second row, the shot gather of the straight (Fiber
1) and helical fiber (Fiber 2)

FIG 5.3. Sensors' frame dimensions. The 0.73 m length sides shown will result in a 1 m
square for 10.2 cm (4") diameter PVC pipe and corners (from Hall et al., 2022)
FIG 5.4. Schematic diagram in plan view for the Croissant parametrization with its
segments and dimensions
FIG 5.5. Workflow implemented to create the Croissant Loop Path in MATLAB. Input
parameters and constants are in the red box, functions in green box, internal outputs in black box
and final output of the Croissant Loop Path Function in the blue box
FIG 5.6. Visualization of the internal outputs of the Croissant Loop Path Function. a) output
of the mk_croissant_loop function, b) output of the mk_croissant_sensor1, c) output of
mk_croissant_sensors which define the complete Croissant Loop Path; in following sections this
Croissant Loop Path will be seen as a small "T: in Map View
FIG 5.7. Shot gather of the Croissant obtained from the analytical model (left). The map
view (right) shows the source-receiver layout, where the trajectory of the fiber is indicated by small
black "T" symbol. The orientations of the H1 and H2 components are shown with dotted lines.
The red dot marks the source used to generate the shot gather inline with H1 component 78
FIG 5.8. Shot gather of the Croissant obtained from the analytical model (left). The map
view (right) shows the source-receiver layout, where the trajectory of the fiber is indicated by small
black "T" symbol. The orientations of the H1 and H2 components are shown with dotted lines.
The red dot marks the source used to generate the shot gather inline with H2 component 78
FIG 5.9. P-velocity profile from inversion data (provided by CMC)
FIG 5.10. Plan view showing the location of a Croissant (blue), representing a point sensor,
and a source point (red) in a Cartesian coordinate system. The angle between the point sensor and
the source is denoted by \emptyset , measured with respect to the x-axis. L represents the distance between
the point sensor and the source point
FIG 5.11. Cross-section view of the point sensor-source plane. Relevant distances, wave
direction, critical angle, and P-wave velocities in each layer are indicated
xii

FIG 5.12. Source / straight fiber configuration and visualization of the tangent component
of any displacement on the fiber
FIG 5.13. Shot gather of the Croissant obtained from the analytical model (left). The map
view (right) shows the source-receiver layout, where the trajectory of the fiber is indicated by small
black "T" symbol. The orientations of the H1 and H2 components are shown with dotted lines.
The red dot marks the source used to generate the shot gather inline with H1 component 82
FIG 5.14. Shot gather of the Croissant obtained from the analytical model (left). The map
view (right) shows the source-receiver layout, where the trajectory of the fiber is indicated by small
black "T" symbol. The orientations of the H1 and H2 components are shown with dotted lines.
The red dot marks the source used to generate the shot gather inline with H2 component 83
FIG 5.15. Ricer wavelet. Frequency content of 40 Hz
FIG 5.16. Cross-correlated wavelet from sweep; a) Raw cross-correlated wavelet; b) Raw
wavelet spectrum, initial frequency content: 10-150 Hz; c) Modified cross-correlated wavelet with
low-pass filter of $60~\mathrm{Hz}$ applied, cropped $0.6~\mathrm{s}$, and resampled; d) Modified wavelet spectrum,
frequencies content 0-60 Hz
FIG 5.17. Shot gather of the Croissant obtained from the finite difference model (left). The
map view (right) shows the source-receiver layout, where the trajectory of the fiber is indicated by
small black "T" symbol. The orientations of the H1 and H2 components are shown with dotted
lines. The red dot marks the source used to generate the shot gather inline with H1 component. 89
FIG 5.18. In blue, average trace amplitudes for the three components, H1, V, and H2 for
Croissant 2
FIG 5.19. Shot gather of the Croissant obtained from the finite difference model (left). The
map view (right) shows the source-receiver layout, where the trajectory of the fiber is indicated by
small black "T" symbol. The orientations of the H1 and H2 components are shown with dotted
lines. The red dot marks the source used to generate the shot gather inline with H2 component. 90

FIG 5.20. Shot gather source 4, farthest source, inline with H1 component (250 ms AGC
applied)
FIG 5.21. In blue, average trace amplitudes for the three components, H1, V, and H2 for
shot 4 of Croissant 2
FIG 5.22. Shot gather source 15, nearest source, inline with H1 component (250 ms AGC
applied)
FIG 5.23. Shot gather source 10, inline with H2 component (250 ms AGC applied) 93
FIG 5.24.Particle velocity shot gather from line of geophones passing through the source
and Croissant location
FIG 6.1. Croissant shot gathers for shot 1 from L41: a) experimental data, AGC win 250ms;
b) synthetic data, AGC win 250m
FIG 6.2. Normalized spectra for experimental and model data a) Spectrum for experimental
data; in blue, wavelet extracted from cross-correlation between the source sweep with the DAS
trace; in red, the spectrum for the Croissant DAS experimental data. B) Spectrum for model data;
in blue, the spectrum of the modified wavelet (low-pass filter of 60 Hz); in red, the spectrum of
the DAS model data
FIG 6.3. Normalized spectra for model data in homogeneous half-space; a) Spectrum for
the Croissant DAS data; b) Spectrum for the Particle velocity data
FIG 6.4. Normalized spectra for model data in homogeneous layered model; a) Spectrum
for the Croissant DAS data; b) Spectrum for the particle velocity data
FIG 6.5. (a) Definition of the MER attribute of a seismic trace. The preceding and trailing
energy collection windows have equal lengths L located at a test point i. (b) The vertical black line
is the time of the peak MER value; the black and green dots indicate manually picked first-break
times (extracted from Wong, 2023)

FIG 6.6. Shot gather for shot 1 (L41) for Croissant 2, with H1, V and H2 components.
Traces in wiggle display are shown. 105
FIG 6.7 Signal to noise ratio by trace for shot 1 (L41) - Croissant 2 by components 106
FIG 6.8. Shot gather for shot 1 (L41). Traces for Croissant 2, 3 and 1 with their respective
components are visible. Blue circles are the automatic first-break picking from MER.
winMer=10ms
FIG 6.9. Shot gather for shot 1 (L41). Traces for Croissant 2, 3 and 1 with their respective
components are visible. Blue circles are the automatic first-break picking from MER.
winMer=45ms
FIG 6.10 Croissant data separated in three components Vertical, Horizontal 1 and
Horizontal 2. Window showed 0-200ms
FIG 6.11 Stacked traces by components by Croissant - This Data correspond to Croissant
1 Shot 1 (L41)
FIG 6.12. First break picking for experimental field data. In green circles after use the
vertical stacked trace. Gain applied
••
FIG 6.13. Example time window for First Arrival Analysis enclosed in the dotted blue box.
In green, the first-break time; RMS window 40 ms below the FB
FIG 6.14. Schematic representation of the Line 41 with the twenty-four shots (left).
Croissant location in blue. Horizontal 1 component color coded in orange, shots to the NE and SW
aligned with the H1 component. Horizontal 2 component color coded in yellow, shots to the SE
and NW aligned with the H2 component. (right) Shots vs Offset, shots highlighted in grey are near
offset
FIG 6.15 Average RMS Amplitudes per Azimuth for First Arrival Analysis for
homogeneous half-space (time window 25ms). In light gray are the shot numbers (1-24). Radial

axes correspond to the average RMS amplitude, and angles correspond to shot-Croissant azimuth
FIG 6.16 Average RMS Amplitudes per Azimuth for Surface Wave Analysis for
homogeneous half-space (time window 200ms). In light gray are the shot numbers (1-24). Radial
axes correspond to the average RMS amplitude, and angles correspond to azimuth shot-Croissant
location
FIG 6.17. Average Amplitude for the three Croissants for Body and Surface waves for the
Homogeneous model
FIG 6.18 Average RMS Amplitudes per Azimuth for First Arrival Analysis for
homogeneous layered model data (time window 20ms). In light gray are the shot numbers (1-24).
Radial axes correspond to the average RMS amplitude, and angles correspond to azimuth shot-
Croissant location
FIG 6.19 Average RMS Amplitudes per Azimuth for Surface Wave Analysis for
homogeneous layered model data (time window 600ms). In light gray are the shot numbers (1-24).
Radial axes correspond to the average RMS amplitude, and angles correspond to azimuth shot-
Croissant location
FIG 6.20. Amplitude Spectra for Croissant 1, from data acquisition of 2025, 4 sweeps.
FIG 6.21 Average RMS Amplitudes per Azimuth for First Arrival Analysis (time window
40ms). Vertical Components from 2023/2024/2025. In light gray are the shot numbers (1-24).
Radial axes correspond to the average RMS amplitude
FIG 6.22 Average RMS Amplitudes per Azimuth for First Arrival Analysis (time window
40ms). Horizontal 1 Components from 2023/2024/2025. In light gray are the shot numbers (1-24)
Radial axes correspond to the average RMS amplitude

FIG 6.23 Average RMS Amplitudes per Azimuth for First Arrival Analysis (time window
40ms). Horizontal 2 Components from 2023/2024/2025. In light gray are the shot numbers (1-24).
Radial axes correspond to the average RMS amplitude
FIG 6.24. Average RMS amplitude vs Offset for the three Croissants for body waves (first
arrival characterized by P-wave) from the Croissant experimental data
FIG 6.25. LiDAR image, elevation map, provided by CMC. VP Locations are the black
circles enumerated from 1 to 24. Croissant locations in red
FIG 6.26. Average RMS Amplitudes per Azimuth for First Arrival Analysis (time window
40ms). Vertical, Horizontal 1 and Horizontal 2 components from 2025 dataset. In light gray are
the shot numbers (1-24). Radial axes correspond to the average RMS amplitude corrected by the
geometric factor by Croissant
FIG 6.27 Average RMS Amplitudes per Azimuth for Surface Wave Analysis (time window
$FB/1000). \ Vertical \ Components \ from \ 2023/2024/2025. \ In \ light \ gray \ are \ the \ shot \ numbers \ (1-24).$
Radial axes correspond to the average RMS amplitude
FIG 6.28 Average RMS Amplitudes per Azimuth for Surface Wave Analysis (time window
FB/1000). Horizontal 1 Components from 2023/2024/2025. In light gray are the shot numbers (1-
24). Radial axes correspond to the average RMS amplitude
FIG 6.29 Average RMS Amplitudes per Azimuth for Surface Wave Analysis (time window
FB/1000). Horizontal 2 Components from 2023/2024/2025. In light gray are the shot numbers (1-
24). Radial axes correspond to the average RMS amplitude
FIG 6.30. Average RMS amplitude vs Offset for the three Croissants for surface waves
from the Croissant experimental data
FIG 6.31. Average RMS Amplitudes per Azimuth for Surface Wave Analysis (time
window 800ms). Vertical, Horizontal 1 and Horizontal 2 components from 2025 dataset. In light
gray are the shot numbers (1-24). Radial axes correspond to the average RMS amplitude corrected
by the geometric factor by Croissant.

FIG 6.32 Representative signal to noise ratio for Croissant 3, comparing 2024 (2 Sweeps)
and 2024 (4 Sweeps) data
FIG 6.33 Representative signal to noise ratio for Croissant 3, comparing 2023 (2 Sweeps)
and 2024 (2 Sweeps) data
FIG 6.34 Representative signal to noise ratio for Croissant 3. Comparison between
2023(2S) and 2025(4S) data
FIG 6.35 Signal-to-noise ratio for Croissant 1, 2 and 3 (columns), for Shot 1, 9, 15 and 18
(rows) from 2025 (4S) dataset
(10.10) 110111 2020 (10) 111111111111111111111111111111111
FIG 7.1. Trace comparison from Croissant and Geophone for shot 4, the farthest shot
(vertical component of Croissant 1 and geophone in Croissant 1 location)
FIG 7.2. Amplitude Spectrum from traces of co-located geophone data
FIG 7.3 Average RMS Amplitudes per Azimuth for First Arrival Analysis (time window
30ms). Vertical, Horizontal 1 and Horizontal 2 traces from co-located geophones. In light gray are
the shot numbers (1-24). Radial axes correspond to the average RMS amplitude 145
FIG 7.4. Average RMS amplitude vs Offset for the traces of the co-located geophones.
Geometric correction obtained from a power trend for the first arrival time window
The second contains a norm a power work and the wind winds with a second norm and the second normal norm and the second normal norm and the second norm and the second normal no
FIG 7.5 Average RMS Amplitudes per Azimuth for First Arrival Analysis (time window
30ms) corrected by geometrical factor. Vertical, Horizontal 1 and Horizontal 2 traces from co-
located geophones. In light gray are the shot numbers (1-24). Radial axes correspond to the average
RMS amplitude. Shots 9, 10, 17, and 18 deleted due to high amplitudes
FIG 7.6 Average RMS Amplitudes per Azimuth for Surface Wave Analysis (time window
250ms). Vertical, Horizontal 1 and Horizontal 2 traces from co-located geophones. In light gray
are the shot numbers (1-24). Radial axes correspond to the average RMS amplitude
FIG 7.7 Average RMS Amplitudes per Azimuth for Surface Wave Analysis (time window
250ms) corrected by the geometric factor in the surface wave window. Vertical, Horizontal 1 and
xviii

Horizontal	2 traces	from co	-located	geopl	nones.	In light	gray	are th	e shot	numl	bers ((1-24)	. Radia
axes corres	spond to	the avera	age RMS	S amp	litude.								149

List of Tables

Table 4.1. Summary table of Line 41 acquisition for 2023, 2024 and 2025
Table 5.1. Coordinates for the junction of 4 segments defining the fiber path
Table 5.2. Differences in offset for Croissants 1, 2 and 3 respect to shot 15
Table 5.3. Estimated values for the synthetic shot gather from geophones for shot 15 9

1. CHAPTER 1 – INTRODUCTION

Seismic acquisition is a fundamental component of both scientific seismology and exploration and development in the oil and gas industry. Instruments such as geophones and seismometers are traditionally employed to investigate the Earth's interior, characterize subsurface structures, and explore for natural resources. By recording the seismic wave field generated from natural (e.g., earthquakes) or artificial (e.g., controlled explosions or vibrators) sources, these instruments enable the estimation of key subsurface properties.

In recent years, fiber-optic technologies, originally developed for telecommunications, have been increasingly adapted for geophysical monitoring and acquisition. One of the most significant advances in this area is Distributed Acoustic Sensing (DAS). Over the past two decades, DAS has emerged as a valuable alternative to conventional geophones in seismic acquisition. DAS systems offer high spatial resolution—typically between 1 and 10 meters—and operate over a broad frequency range, from millihertz to tens of kilohertz. These features, combined with simpler deployment logistics, lower costs, and resilience to extreme environmental conditions (from -50°C to 400°C), have enabled DAS to be employed in a wide range of applications (Tang et al., 2021). These include vertical seismic profiling (VSP), downhole surveillance, microseismic monitoring, flow monitoring, carbon capture and storage (CCS), geothermal energy exploration, mineral prospecting, and earthquake seismology, among others (Mateeva et al., 2014; Daley et al., 2013; Lindsey et al., 2017; Ajo-Franklin et al., 2019).

1.1 Conventional sensors – geophones and seismometers

Geophones are similar to seismometers in their design and are also used to register seismic waves. In the past, there were clear differences between geophones and seismometers. Compared to conventional geophones, seismometers are more suitable for detecting extremely small ground movements as they cover a wider frequency band, including the frequency range below their natural frequency, usually from 0.01 to 50 Hz (Hou et al., 2021). In conventional geophones, the frequency band is in the range of 1-15 Hz. They are cheaper than seismometers and are therefore more commonly used in arrays for large area detection with better specialised resolution. However, with the development of new technologies, the frequency coverage in compact devices has also

increased significantly, so that geophones can now cover frequency bands from 0 to 500 Hz and the boundaries between geophones and seismometers are becoming blurred (Hou et al., 2021).

In these conventional sensors, a coil is suspended by springs in a magnetic field (the magnet may be integral with the case of the instrument). A seismic wave moves the case and the magnet, but the coil remains relatively stationary because of its inertia. The relative movement of a magnetic field with respect to the coil generates a voltage across the coil, the voltage being proportional to the relative velocity of the coil with respect to the magnet. Below the natural frequency, the output (for input of constant velocity of magnet motion) is proportional to frequency and hence to the acceleration involved in the seismic wave (Evenden et al., 1971).

Geophones ordinarily respond to only one component of the ground's displacement, velocity, or acceleration that is involved in the passage of a seismic wave. Three mutually orthogonal phones are used to record all three components (Evenden et al., 1971).

The majority of geophones are used in reflection seismology to record the energy waves reflected by the subsurface geology. In this case the primary interest is in the vertical motion of the Earth's surface. However, not all the waves are upwards traveling. A strong, horizontally transmitted wave known as ground-roll also generates vertical motion that can obliterate the weaker vertical signals (Sheriff and Geldart, 1995; Yilmaz, 2001).

1.2 Fiberoptic sensor – Distributed Acoustic Sensing (DAS)

DAS operates based on the principles of optical time-domain reflectometry (OTDR). A coherent laser pulse is transmitted along a fiberoptic cable. As the light travels through the fiber, a small portion is scattered due to Rayleigh, Raman, and Brillouin interactions (Shatalin et al., 2021). This backscattered light is captured by an interrogator unit. The time delay between the emitted pulse and the returned signal allows the system to determine the position along the fiber at which scattering occurred.

When the fiber is subjected to strain—such as from seismic waves—the local stretching or compression alters the phase of the backscattered light. These changes in phase cause interference

patterns in the returned signal, which are measured over time to infer strain or strain rate. In effect, the entire optical fiber acts as a distributed array of seismic sensors.

DAS measurements are typically averaged over a segment of the fiber referred to as the gauge length, meaning the recorded signals represent strain integrated over this distance. While data are often presented as a time series from discrete points, it is essential to recognize this averaging effect. The ability to obtain densely sampled seismic wave fields using existing fiber infrastructure has significantly expanded the scope of geophysical applications for DAS (Daley et al., 2016;Mestayer et al., 2011).

Initial implementations of DAS were concentrated in borehole environments, where coupling between the fiber and surrounding rock can be made strong. These setups have been particularly effective in vertical seismic profiling and monitoring of hydraulic fracturing operations (Karrenbach et al., 2018). However, DAS is also being investigated for surface seismic reflection surveys. Although surface installations are often limited by poor sensitivity to steeply incident P-waves, modified cable geometries can partially mitigate this issue (Bakulin et al., 2020).

DAS-recorded strain-rate signals closely resemble conventional seismometer outputs but differ due to their directional response. However, practical cable layouts frequently include bends and directional changes, complicating this conversion.

While DAS offers considerable promise, its measurement of only axial strain limits its ability to capture the full vector nature of seismic waves; the same can be said of single-component geophones. This constraint poses challenges for tasks such as seismic inversion and reservoir characterization (Lim Chen Ning and Sava, 2018).

1.3 Challenges with DAS

Despite its advantages, DAS technology presents several challenges that must be addressed to enable broader adoption in land-based seismic acquisition.

One major limitation is the lack of multicomponent capability. Traditional DAS systems are sensitive only to strain along the axis of the fiber. As a result, signals arriving perpendicular to the fiber—so-called broadside signals—are often underrepresented or entirely missed (Bakku, 2015; Lumens, 2014). Field trials have confirmed that DAS sensitivity to plane P-waves drops as $\cos^2\theta$ with increasing angle θ (Kuvshinov, 2016). Since the recorded strain reflects only the component aligned with the fiber's axial orientation, the full seismic wave field cannot be captured without geometric modifications to the cable layout. Some studies have proposed coiled or helically wound fiber arrangements to recover multiple directional components and reconstruct the local strain tensor (Innanen, 2017; Kuvshinov, 2016; Lim Chen Ning and Sava, 2018; Mateeva et al., 2014; Takekawa et al., 2022).

Another important consideration is the fiber-to-soil coupling. Effective data acquisition relies on strong mechanical contact between the fiber and the surrounding medium. In many deployments, especially surface-laid cables, coupling is weak due to reliance on gravity and friction alone (Martin et al. 2017). Poor coupling particularly affects high-frequency signals, diminishing data quality. Buried or trenched installations improve coupling but present logistical and financial challenges, especially in complex terrain or protected environments.

Nonetheless, even with imperfect coupling, DAS has proven capable of recording surface waves, refracted arrivals, and microseismic events. Furthermore, the use of ambient noise interferometry with DAS holds promises for long-term monitoring applications, including virtual source imaging and earthquake detection (Ajo-Franklin et al., 2019; Lindsey et al., 2020)

1.4 DAS in seismic

Modern land seismic acquisition has been trending toward "light and dense" survey geometries, aimed at minimizing equipment while increasing spatial resolution. Within this paradigm, wireless nodal systems have gained traction due to their operational flexibility (Bakulin et al. 2020). However, these systems often forego array-based signal averaging, which can reduce data quality. Densely spaced geophones (e.g., 1-meter intervals) could compensate for this

limitation, but the associated costs remain prohibitive due to limited economies of scale in point sensor manufacturing.

In this context, DAS offers a compelling alternative. Its capacity for high channel density and fine spatial sampling makes it particularly suited for land-based seismic surveys. A single deployment of fiber-optic cable can serve as a dense linear array, facilitating continuous seismic recording without the need to reposition sensors. This approach supports multiple exploration objectives, including shallow imaging, deep-target characterization, and velocity model development.

While DAS systems are inherently limited by directional sensitivity and cannot record three-component data, the potential benefits—such as reduced field labor, low marginal cost per channel, and rapid scalability—often outweigh these drawbacks. Additionally, with sub-meter spatial resolution, DAS provides a level of data coverage that is economically unattainable with conventional geophone arrays.

Although DAS has been more commonly used in borehole applications, its utility in surface seismic acquisition is gaining recognition. Surface deployments are poised to benefit significantly from DAS technology, particularly as demand grows for high-density spatial sampling in both academic and industry settings.

1.5 Thesis overview and objectives

This thesis explores the feasibility, performance, and interpretability of DAS in land-based seismic acquisition through an experimental deployment. To me and my collaborators' knowledge, it represents the only field-deployment of a system of the type discussed above: one built to measure, through shaping, full vertical and horizontal components of strain rate. In this thesis I investigate its response with the aim to develop it as a novel, low-cost, multi-component DAS sensor. It is referred to as the *Croissant*.

One of the motivations for this work is to introduce the possibility that, in an otherwise single-component experiment such as DAS, it may be useful to have selected points where the full elastic wave field can be measured. The idea is to determine whether single-component DAS data, which are inherently limited in directional sensitivity, can be appropriately used for monitoring when it is supported by the sensing of the full multicomponent seismic wave field. If that proves to be the case, then DAS—already valued for its low cost, long-term monitoring capabilities, and use of the same system, same fiber, and same interrogator—could be enhanced through the addition of compact, point-based multicomponent sensors like the Croissant, without compromising its cost-effectiveness.

This study is based on multi-year data acquisition carried out at the Carbon Management Canada (CMC) Newell County facility. Data were collected between 2023 and 2025 along a circular source line, Line 41, using a P-wave vibrator (P-Vibe). This experimental dataset enables the analysis of the Croissant's response to a wide range of azimuths, and offsets, allowing for an evaluation of its directional sensitivity and potential, in the future, for the full strain tensor recovery.

The Croissant sensor builds upon previous work involving buried directional DAS sensors (DDS), particularly the *Pretzel* configuration tested by Innanen et al., (2018) and Hall et al., (2020; 2022) as well as the small-scale multi-component prototype developed by Takekawa et al. (2022). The Pretzel, a 10×10 m flat fiber layout, demonstrated the ability to measure horizontal strain components but lacked vertical sensitivity due to its two-dimensional design. In contrast, the Croissant measures approximately $1 \times 1 \times 1$ m and consists of fiber wrapped on two vertical plastic frames set at right angles, enabling it to capture vertical motion while maintaining a compact and permanent design.

One important question regarding the feasibility of directional DAS sensors like the Croissant is whether such a sensor can be deployed at large scale. The design involves wrapping fiber multiple times around frames, which may not be practical for broad deployment due to labor, material, or spatial constraints. Rather than proposing the Croissant as a scalable replacement for conventional linear DAS arrays, this study explores its potential as a point-based, multi-component sensing unit. The aim is to assess whether this compact, permanent design can provide enhanced

strain information—ideally enabling 3- to 9-component measurements at discrete locations—offering richer data at strategic points in a survey area for seismic analysis purposes.

The core goal of this work is to characterize the Croissant's response to a multi-offset, multi-azimuth source-receiver geometry. A key objective is to compare the recorded experimental data with synthetic responses generated from numerical models and from co-located geophone measurements. This comparative analysis aims to evaluate the sensor's directional sensitivity, amplitude response, and the inherent frequency content of the seismic wave field recorded by each multicomponent sensor, as well as to use the analysis to suggest ways the Croissant might be improved for future applications.

To provide a roadmap of the thesis, the chapters are organized as follows:

- Chapter 2 provides the theoretical foundation and principles of DAS technology, describing the main system components as well as the mathematical framework and associated limitations.
- Chapter 3 outlines key concepts from seismology about wave propagation, properties of P-waves and S-waves, and geometric spreading, which form the basis for interpretation in the chapters that follow.
- Chapter 4 describes the project location, geological setting, data acquisition methods, and experimental configurations used during the 2023–2025 campaigns. Each dataset is introduced, along with details of the source and receiver geometries.
- Chapter 5 presents a set of analytical and numerical models used to simulate the Croissant's response. These include homogeneous media, a two-layer system, and a 3D elastic finite-difference simulation incorporating surface wave phenomena. A thorough analysis of the amplitude response is conducted to understand what the Croissant's response should be in both simple and layered elastic models.
- Chapter 6 focuses on the interpretation of experimental data recorded by the Croissant, emphasizing signal types, arrival times, and amplitude characteristics observed in the dataset.

• Chapter 7 presents a comparative analysis between Croissant DAS data and co-located geophone recordings, assessing the level of agreement between the two sensor types.

Together, these chapters aim to demonstrate the capabilities of the Croissant sensor in addressing the limitations of conventional DAS for surface seismic acquisition and to evaluate its potential as a permanent, multicomponent alternative to traditional seismic sensors.

2. CHAPTER 2: DAS Foundations and Principles

Fiberoptic cables are typically deployed in support of the telecommunication industry and information transmission. Over time, the same physical infrastructure has found a second life in the world of sensing, particularly in geoscience applications. This crossover is made possible by exploiting the physical phenomena that were once considered limitations in telecom—namely, the backscattering of light within the fiber. This innovative repurposing has led to the development of DAS, a technique that transforms standard optical fibers into powerful strain measuring devices. To briefly develop how DAS works, this chapter begins by exploring the original role of fiber optics in telecommunications, followed by an explanation of the DAS operating principles, its components, and a mathematical definition of strain as it relates to the measurements made using optical fibers.

2.1 Fiber optics in the telecommunications industry

Over the past several decades, optical fibers have carried the bulk of international and domestic telecommunications traffic, including telephone, internet, and multi-channel high-definition television services. One inherent challenge in this application is the backscattering of light, which arises from microscopic variations in the fiber's refractive index. Typically treated as a source of noise, telecommunication service companies employ devices known as Optical Time Domain Reflectometers (OTDR), exploiting the backscattered light to test the fiber quality and detect flaws with splices and coupling (Eaid and Innanen 2019).

Recent work has focused on using the interference pattern of samples of the backscattered light, compared to previously backscattered light, to turn the fibers into sensors of physical quantities including strain, stress, and temperature. To achieve this, the laser pulse injected into the fiber must be fairly coherent, a condition not met by typical OTDR. Special reflectometers, known as Coherent Optical Time Domain Reflectometers (COTDR) have been developed to turn standard optical fibers into highly sensitive, distributed strain sensors (Eaid and Innanen 2019).

2.2 DAS Principles

The basic principle of DAS involves injecting a coherent laser pulse into an optical fiber and detecting the Rayleigh backscattered interference along the fiber (Figure 2.1). When an acoustic wave or other mechanical disturbance interacts with the fiber, it induces localized strain, altering the optical phase of the backscattered pulses separated by a distance called the gauge length. This phase alteration affects the interference pattern between the two pulses, causing variations in the intensity of the returning signal.

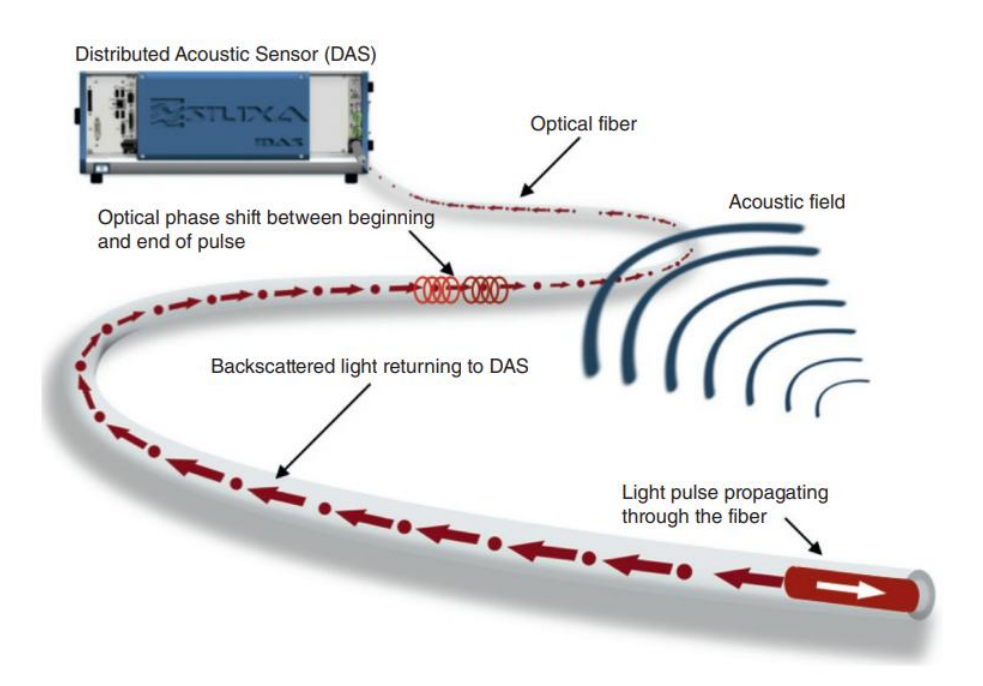


FIG 2.1 Operation principle of distributed acoustic sensing (Shatalin et al., 2021).

The backscattered light can be modeled as a combination of reflections with random amplitude and phase. When the fiber is strained, these amplitude and phase values vary unpredictably along its length, but the intensity of the backscatter correlates with the strain rate at each point (Shatalin et al., 1998). This response allows DAS systems to detect and localize dynamic events in real time.

2.3 DAS System Components

According to Willis (2022), DAS systems consist of four fundamental components:

- 1. The fiber
- 2. The fiber deployment method
- 3. The interrogator and gauge length
- 4. Measurement of the fiber: Strain or strain rate

2.3.1 The fiber

Optical fiber is comprised of a cylindrical core, normally of fused silica glass, surrounded by a concentric cladding layer with a lower index of refraction (Figure 2.2). The combined cylinder is only a few tens of microns in diameter but potentially many tens of kilometres in length; hence "fiber". The fragile fiber is normally enclosed within strength members and a protective outer layer to yield a practical, deployable fiber optic cable (SEAFOM, 2024).

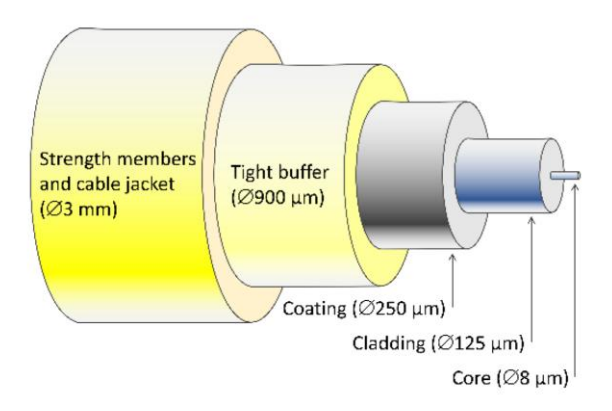


FIG 2.2. Structure of a classical, cylindrically symmetric, glass-based optical fiber (extracted from SEAFOM, 2024)

Modern fiber achieves extremely high reflection efficiency at the core-cladding boundary and extremely low attenuation in the core so that optical losses with propagation distance are very low.

Light travels in the glass core and the surrounding cladding enables the optical mechanism to keep the light trapped inside the core (Willis 2022). As shown in Figure 2.3, using ray theory from geometrical optics, the cladding will keep light inside the fiber for all ray angles smaller than the

critical angle of refraction, θ_c , given by (Thevenaz, 2011). To restrict the ray angles, the diameter of the fiber must be small compared to the wavelength of the light.

$$\theta_c = \cos^{-1}(\frac{n_{clad}}{n_{core}})$$
 (2.1Error! No sequence specified.)

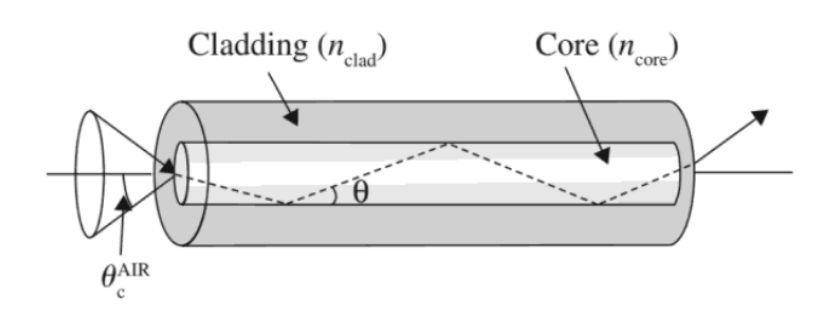


FIG 2.3 Reflection at the core-cladding interface is total (extracted from Thevenaz, 2011)

The jacket that covers the fiber has two main functions: (i) to absorb all cladding light which is not properly guided; and (ii) to protect the otherwise naked glass from atmospheric interactions, which can compromise the mechanical strength of the fiber. Jacket materials may include simple acrylate, easy-to-strip coating (normally 250 microns in diameter), a bit thinned (~140 micron) polyimide coating for high temperature (180 °C) applications, including embedding in composite structures, as well as more exotic compounds such as carbon or aluminum for special applications (Thevenaz 2011).

Each fiber in the fiber optic cable can be used to measure the motion of the ground. The DAS measurement is almost exclusively sensitive to the longitudinal stretching or compressing of the fiber (Willis 2022). This means DAS primarily detects strain along the axis of the fiber, making it a single-component (axial) sensor that is most responsive to seismic or acoustic waves aligned with the fiber's length (Mateeva et al. 2014).

2.3.2 Fiber Deployment Methods – Surface

In terms of fiber deployments, two different kinds of fiber optic cable deployment are used. Depending on the application, the cable can be positioned parallel to the surface or into a borehole (Willis 2022). Using whichever method chosen to deploy it, the fiber itself is the basis for sensing the motion of the earth.

Fiber-optic cables can be buried in the ground to measure vibrations in their surrounding materials, making them effective tools for near-surface seismic and acoustic monitoring. One simple deployment method involves laying the fiber optic cable directly on the surface, where it may rest above the ground, sometimes supported by vegetation such as grass and twigs. While this method is low-cost, it often results in poor coupling with the ground. A more effective, though more expensive, approach is to place a material on top of the cable to press it against the ground and improve coupling. However, fiber-optic cables are most commonly buried in shallow trenches to ensure stronger and more consistent mechanical contact with the soil.

Research has demonstrated that good coupling can also be achieved through various alternative methods: pushing the cable directly into the soil (Lindsey and Martin, 2021), laying it on the surface (Spikes et al. 2019), or in cold environments, pouring water over the cable to freeze it in place (Yang et al. 2021). Despite these options, surface deployments can be logistically challenging in areas with infrastructure obstacles such as roads, buildings, or rocky near-surface conditions. In some such cases, an effective workaround can be to utilize pre-existing fiber optic cables already installed in telecommunications conduits or tunnels within the area of interest (Martin et al. 2017).

2.3.3 Interrogator unit and gauge length

The interrogator unit (IU) is a critical component in DAS systems, responsible for detecting perturbations along a fiber-optic cable. It operates by transmitting coherent laser pulses into the fiber and analyzing the Rayleigh backscattered light that returns due to microscopic variations in the refractive index of the glass (see Figure 2.4). These natural imperfections are distributed throughout the fiber and reflect a portion of the incident light back toward the IU (Kennett, 2024; Willis, 2022).

As the fiber experiences mechanical disturbances, such as strain or vibration, the optical path length changes, resulting in phase shifts in the backscattered light. The IU measures these phase shifts to determine the amount and location of fiber deformation.

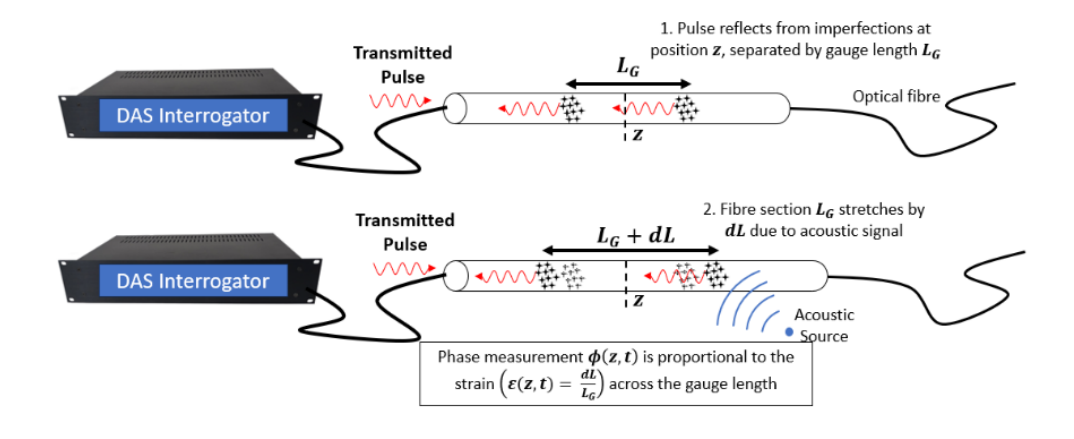


FIG 2.4. Typical DAS strain measurement, over gauge length (Terra15, 2024)

The gauge length is a hardware or software constraint on any DAS system (depending on vendor), given as a fixed distance along the DAS cable. The presence of a characteristic gauge length in a DAS data set reflects the fact that the measurement should be understood as an average of strain-rate over a finite segment of the fiber, as opposed to a point measurement. The gauge length characterizes the spatial resolution of the sensing system. For localized seismic or acoustic events, the strain rate observed in a DAS experiment can be interpreted as the difference in ground velocity resolved along the fiber at the ends of the gauge interval (Kennett, 2024).

The longer the gauge length the greater the sensitivity to comparatively large-scale strain features since a smaller change in mean strain is required in a longer gauge length to produce the IU's minimum measurable change in optical phase, but the less precisely the IU is able to spatially resolve comparatively small-scale sources of strain. There is a compromise, therefore, in the choice of gauge length between strain sensitivity and range resolution (SEAFOM, 2024).

2.3.4 Measurement of the fiber

To obtain a reliable measurement of strain the concept of a dual-pulse optical system is essential. This methodology creates two pulses of backscattered light combined in an interferometric process to construct the phase difference between these pulses. These two pulses of light are delayed in time from each other, either at the launch path of the IU or by a time-delay loop of fiber in the receiver path of the IU and corresponds to what is called the "gauge length. Independent of the design, the effect of this time delay is to allow the system to compare the phase of the backscattered light at all points of the sensing fiber, each separated by gauge length.

Most DAS interrogators measure strain in the fiber, as shown in Figure 2.4. The optically measured interference phase $\phi(z,t)$ is proportional to the strain, $\varepsilon(z,t) = dL/L_G$, as below:

The relationship between the measured phase angle for the two light paths in the interferometer is given by (SEAFOM 2024),

$$\varepsilon(z,t) = \lambda \frac{\phi(z,t)}{4\pi n L_G \xi} \tag{2.2}$$

where n is the refractive index of the fiber, L_G is the gauge length, ξ is the photo-elastic constant, and λ is the laser wavelength in a vacuum.

The strain rate is simply the time derivative of strain given by:

$$\dot{\varepsilon} = \frac{d\varepsilon}{dt} \tag{2.3}$$

All of the terms on the right side of Equation 2.2 are constants except for ϕ , the phase difference. This means that the strain rate is controlled by the change over time of the phase difference of the light from the two paths.

The phase measurement is made by interfering light reflected from scattering sites separated by a short distance L_G , called the gauge length of the system. As the fiber length expands or contracts due to acoustic signals, the phase measurement between the two scattering sites changes

proportionally to the length change of the fiber section, dL or δ , as is shown in Figure 2.5. Strain in the fiber section is the ratio of the length change to the gauge length, dL/ L_G . By making this measurement every time a pulse is sent into the fiber, and at all points z along the fiber, the interrogator makes a continuous, distributed measurement of strain along the whole fiber, $\varepsilon(z,t)$.

2.4 Mathematical definition of strain

When you apply stress to an object, it deforms. If we think about an elastic object and pull on it, it gets longer – it stretches as is shown in Figure 2.5. Deformation is a measure of how much an object is stretched, and strain is the ratio between the deformation and the original length. Strain can be seen as a percent of elongation – how much bigger (or smaller) is the object upon loading it.

In a three-dimensional system, strain refers to the deformation experienced by a material due to an applied stress. It quantifies the relative change in shape or size of the material compared to its original, undeformed state.

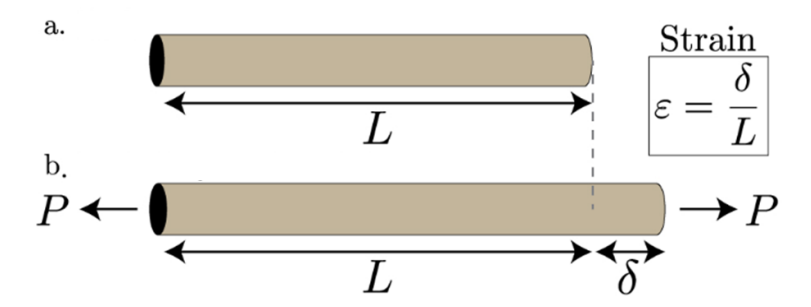


FIG 2.5. Diagram to define strain. (a) It is a bar with length L at the beginning. (b) It is the bar which has been altered by an applied stress P and is now length $L + \delta$ (Mechanics of Slender Structures, 2020)

Normal Strain (ε): Normal strain represents the change in length per unit original length along a particular direction and is denoted by the Greek letter epsilon. It accounts for elongation or contraction of the material along that direction.

Shear Strain (γ): Shear strain describes the change in shape resulting from forces causing parallel planes within the material to slide past one another and is denoted by the Greek letter gamma. It represents the angular deformation of the material (see Figure 2.6).

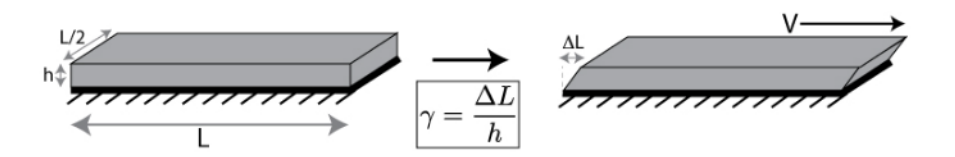


FIG 2.6. Diagram to define shear strain. Deformation of an object is response to a shear stress (i.e. parallel to a surface) (Mechanics of Slender Structures, 2020)

Volumetric Strain: Volumetric strain accounts for the change in volume of the material due to deformation. It considers the combined effects of normal strains in all three dimensions.

Strain is typically represented using a strain tensor, which is a mathematical object that encapsulates the components of strain in different directions. This tensor provides a comprehensive description of how the material deforms under stress and allows for the calculation of various mechanical properties, such as Young's modulus, Poisson's ratio, and shear modulus.

As outlined by Krebes (2019), consider two infinitesimally close points, P and Q, in a medium (see Figure 2.7). Point P is located at $x = (x_1, x_2, x_3)$ and point Q at x + dx. Under stress, P undergoes a displacement u to P', and Q undergoes a displacement u + du to Q'. Mathematically, the displacement of point P is $u = u(x_1, x_2, x_3) \equiv u(x)$, and the displacement of point Q is u(x + dx) = u(x) + du(x), where:

$$du_i(x) = \nabla u_i. dx = \sum_{i=1}^{3} \frac{\partial u_i}{\partial x_j} dx_j, \quad i = 1, 2, 3.$$
(2.4)

 \boldsymbol{u} is a function of the time t also (e.g., when strain is produced by wave motion), but for a static strain, du_i can be rewritten as:

$$du_i = \sum (e_{ij} - \eta_{ij}), \tag{2.5}$$

where
$$e_{ij} = \frac{1}{2} \left(\frac{\partial u_i}{\partial x_i} + \frac{\partial u_j}{\partial x_i} \right)$$
 and $\eta_{ij} = \frac{1}{2} \left(\frac{\partial u_j}{\partial x_i} - \frac{\partial u_i}{\partial x_j} \right)$ (2.6)

Where e_{ij} is a Cartesian tensor of rank 2 and is called the strain tensor and η_{ij} is a rotation tensor. This means the displacement vector accounts for a deformation component and rotation component.

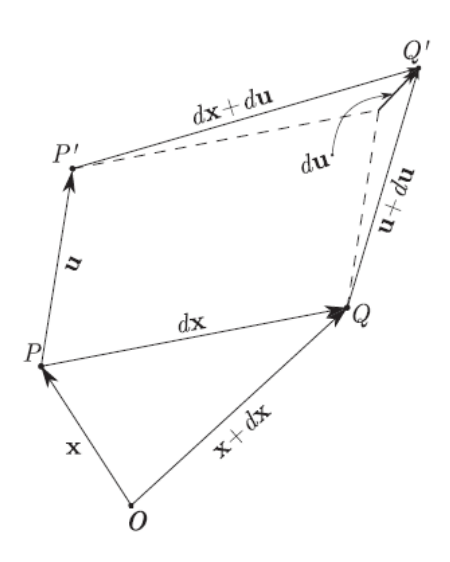


FIG 2.7. Displacement and strain in 3D (extracted from Krebes, 2019)

 e_{11} , e_{22} , and e_{33} are called the normal strains, and e_{12} , e_{13} , e_{21} , e_{23} , e_{31} , and e_{32} are called the shear strains. Like the stress tensor, the strain tensor has only six independent components, since $e_{12} = e_{21}$, $e_{13} = e_{31}$, and $e_{23} = e_{32}$ due to symmetry in the strain tensor.

The normal strains, sometimes called longitudinal strains e_{ii} , have simpler formulas than the shear strains e_{ij} .

$$e_{11} = \frac{\partial u_1}{\partial x_1}$$
 and $e_{12} = \frac{1}{2} \left(\frac{\partial u_1}{\partial x_2} + \frac{\partial u_2}{\partial x_1} \right)$ (2.7)

The normal strain e_{11} is the relative change, due to strain, in the x_1 component of the vector distance between two infinitesimally close points that both lie on the x_1 axis prior to being strained. Similarly, the normal strain e_{22} is the relative change in the x_2 component of the vector distance between two infinitesimally close points that both lie on the x_2 axis prior to being strained. A similar statement can be made for e_{33} .

2.5 Strain and strain rate measured by the fiber

A fiber core can be surrounded by layers of different materials (coating, cladding, and jacket). We treat these materials as a single uniform material with some effective elastic properties, which is called the "cable." The cable can be viewed as anelastic material that fills a straight, small-diameter hole in a subsurface formation. We are considering a cable with a straight fiber, which is shown in Figure 2.8. The direction along the fiber is called the longitudinal direction and is labelled by the subscript "z". The direction along the cable is called the axial direction and is labelled by the subscript "\mathbb{"}". In the case considered, the axial and longitudinal directions coincide (Kuvshinov, 2016).

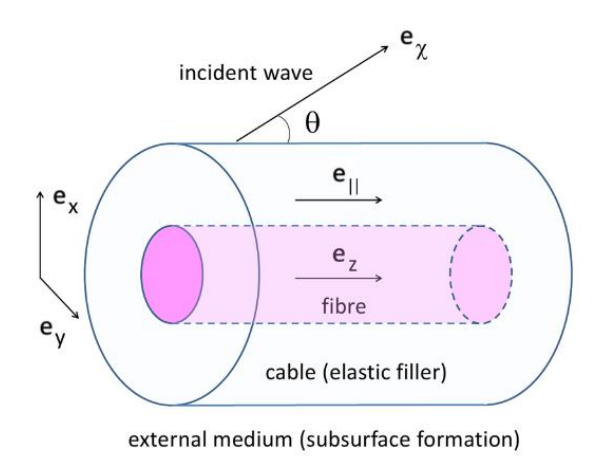


FIG 2.8. Straight optical fiber embedded in a cable (obtained from Kuvshinov, 2016)

In Figure 2.8, the coordinate vectors $e_{\rm x}$ and $e_{\rm y}$ are directed normally to the cable axis. The coordinate vectors e_{\parallel} and $e_{\rm z}$ are directed along the cable and along the fiber, respectively. Impinging wave propagates along the coordinate vector e_{χ} , which forms angle θ with respect to the cable axis. In the case considered, $e_{\parallel}=e_{\rm z}$, and the longitudinal strain in the fiber $e_{zz}^{(f)}$ is equal to the axial strain in the cable $e_{\parallel}^{(c)}$ (Kuvshinov 2016).

As described by Kuvshinov (2016), since optical fibers are very thin, the transversal (with respect to the fiber axis) stress $\sigma_{\perp}^{(f)}$ and the longitudinal strain $e_{zz}^{(f)}$ inside a fiber are almost constant over its cross-section. The transversal stress in the fiber $\sigma_{\perp}^{(f)}$ is equal to the transversal

stress in the cable $\sigma_{\perp}^{(c)}$. In what follows, we assume that the fiber is perfectly coupled to the cable, so that the longitudinal strain e_{zz} is transported from the cable to the fiber without losses: $e_{zz}^{(f)} = e_{zz}^{(c)}$

The fiber strains and the DAS signal are mostly governed by the component of the cable strain along the fiber axis (Kuvshinov 2016).

In terms of the interaction of the cable with the seismic waves, the strain is induced by impinging seismic waves. In seismic exploration and reservoir monitoring, one usually deals with P-waves. P-waves generate strain that is parallel to the direction of the wave propagation. If a plane P-wave propagates along the χ -axis, the only non-zero strain component carried by the wave is $e_{\chi\chi}^{(w)}$. Suppose the cable forms the angle θ with the χ -axis, as Figure 2.9 shows. The strain is a second rank tensor, and in contrast to vectors, its projections have a cosine squared dependence. The projection of $e_{\chi\chi}^{(w)}$ along the cable is equal to $e_{\parallel}^{(w)} = e_{\chi\chi}^{(w)} \cos^2 \theta$. In most situations where DAS is used, the cable is coupled to the rock (outer formation), so that its axial strain e(c) is approximately equal to the axial strain in the impinging wave $e_{\parallel}^{(w)}$. The cable and fiber axes coincide if the fiber is straight. Therefore, $e_{zz}^{(f)} = e_{\parallel}^{(w)}$. The DAS signal is proportional to $\cos^2 \theta$, and it barely depends on the cable material (Kuvshinov 2016).

Building on this understanding of strain between the cable to the fiber, we now turn to what the Distributed Acoustic Sensing (DAS) interrogator unit actually measures. The DAS IU detects only the component of strain aligned with the axial (lengthwise) direction of the fiber. For surface-deployed fibers, this direction corresponds to the z-axis, or the direction along the ground. Consequently, the strain component recorded by the DAS system is $e_{zz}^{(f)}$ that is, the deformation due to a force applied in the z-direction and measured in the same direction. If the subscript z is omitted in subsequent equations, it is assumed that the strain is aligned with the fiber axis (Willis 2022).

2.6 DAS spatial parameters

This section provides a definition of terms, units and supporting parameters associated with DAS data that will be used (SEAFOM 2024).

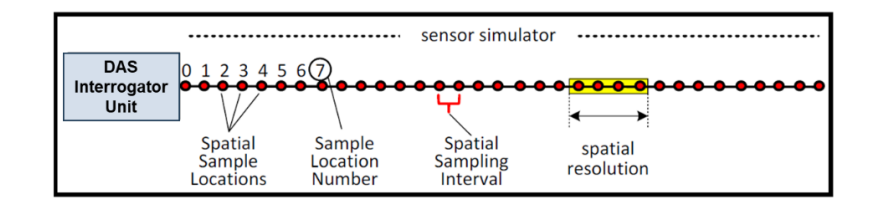


FIG 2.9. DAS interrogator unit test arrangement (extracted from SEAFOM, 2024)

2.6.1 Spatial Sample Location / Sample Location Number

The DAS IU samples the backscattered light from the sensor at different locations along the fiber sensor. These locations are defined through the interrogator configuration or setup and are represented spatially along the fiber as uniformly spaced red dots in Figure 2.9. A numbering system is defined such that the first Spatial Sampling Location starts at zero. Successive locations are numbered as positive integers which increase along the length of the cable (SEAFOM 2024).

2.6.2 Fiber Distance and Spatial Sampling Interval

Fiber distance is the mechanical distance in meters of fiber length from the connector of the IU to the desired Spatial Sample Location (SEAFOM 2024).

The separation in meters between consecutive Spatial Sample Locations defines the Spatial Sampling Interval. It should not be confused with 'Spatial Resolution' (SEAFOM 2024).

2.6.3 Gauge Length and spatial resolution

Gauge length is the distance (mechanical length along the fiber in meters, not optical length) over which the IU measures the change in optical path length and, hence, the change in spatial integral of strain. Gauge length might be defined in hardware or software configuration. It is not necessarily equal to the spatial resolution of the IU, which is a measured performance

parameter. It should, for a properly operating IU, however, be a close approximation (SEAFOM 2024).

2.6.4 Supporting DAS signal parameters

DAS interrogation generally involves periodically pulsed sampling of acoustically or vibrationally induced strain perturbations of the fiber sensor at each of the Spatial Sample Locations. Thus, each Spatial Sample Location yields a sequence or *time series* of strain-change measurements (plus noise) which can be processed according to the intended application information desired.

2.6.5 Sample Rate & Sample number

Sample Rate is the rate at which raw acoustic data are output from the IU for every Spatial Sample Location (SEAFOM 2024). Sample number is the identifying sequence number of a Sample in a Time Series (see Figure 2.10).

2.6.6 Time Series

In DAS systems, the interrogator unit plays a crucial role in converting the optical signal backscattered from a fiber optic cable into a time series (see Figure 2.10) of strain or strain-rate measurements. This process begins when the interrogator sends a sequence of short, coherent optical pulses (typically a few nanoseconds long) into the fiber at a high repetition rate—often in the kilohertz range. As each pulse travels along the fiber, a portion of the light is backscattered from every point due to microscopic variations in the fiber (Rayleigh scattering). This backscattered light is sampled in time, where each time delay corresponds to a specific distance along the fiber, effectively dividing the fiber into discrete "channels," commonly spaced at 1-meter intervals (though this spacing depends on the interrogator settings).

The system detects changes in the phase of the backscattered light between successive pulses. These phase shifts result from dynamic strain in the fiber caused by disturbance by seismic waves or other vibrations passing through the surroundings (Zhan, 2020). It takes only a slight extension or compression to a fiber to change the distances—as measured along the fiber—

between many scattering points (Zhan, 2020). By tracking the phase changes over time at each channel, the interrogator reconstructs a time series of strain or strain rate. The sampling rate of these time series typically ranges from 500 Hz to several kilohertz, with each time sample associated with a new interrogation pulse. The final output is a 2D matrix—channels versus time—that resembles a seismic shot gather.

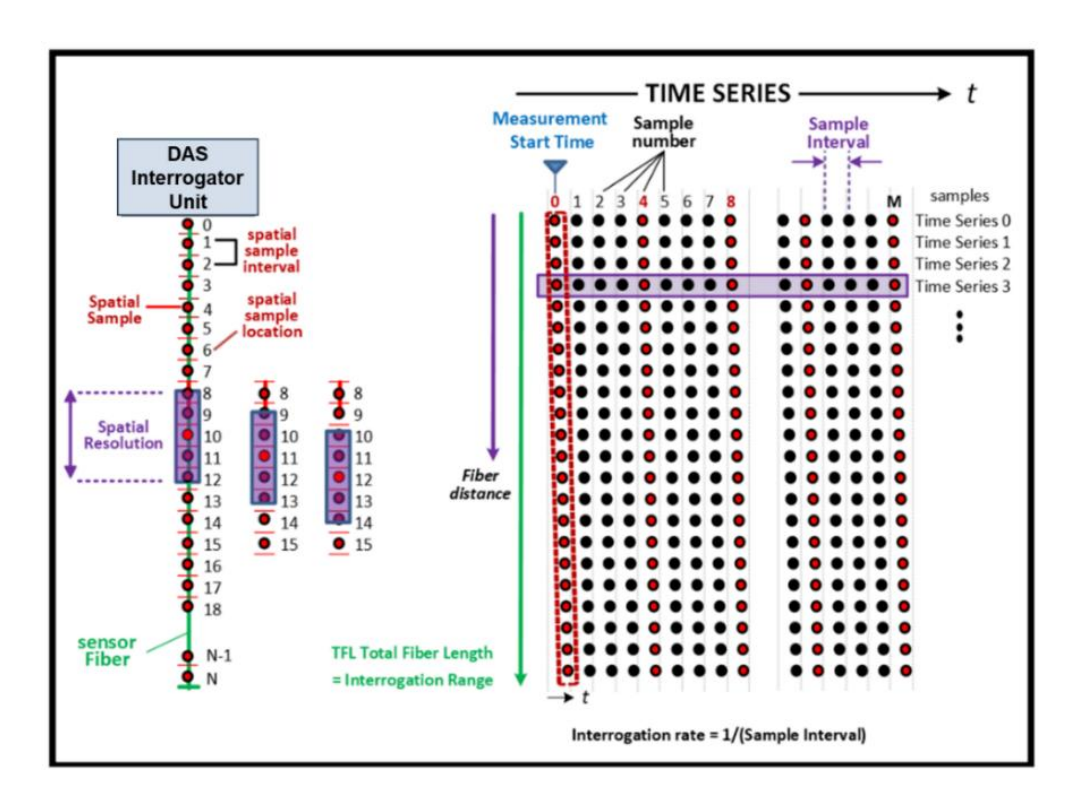


FIG 2.10. Signal parameters relating to Time Series and their Spatial Location Identification (extracted from SEAFOM, 2024)

2.7 DAS directionality and multicomponent sensing: previous work

Directionality of the DAS response depends on the fiber optic cable configuration and the cable design, as the device itself is sensitive only to fiber elongation. We will start our consideration where the fiber is placed linearly inside a cable, with no slippage between fiber and cable, nor between the cable and the ground. In this case, fiber displacement will follow ground displacement, and sensitivity will depend on the relative position of fiber and seismic source. This setup follows the same mechanical principle as early linear strain seismographs, which measured changes in distance between two ground points (Benioff 1935).

The angular response of DAS to seismic waves can be described using geometrical considerations and tensor transformations. For longitudinal (P) waves, the response follows a $\cos^2(\theta)$ pattern, while for transverse (S) waves, it follows $\sin(\theta)\cos(\theta)$, where θ is the angle between the wave vector and the fiber direction (see Figure 2.11)—again, similar to the response described by Benioff (1935). Additionally, fiber orientation affects not only amplitude but also spatial resolution. The fiber acts like an acoustic antenna: if the wavefront travels along the fiber direction, signal variation occurs over short distances. In contrast, if the wavefront is parallel to the fiber axis, the signal remains relatively uniform along the fiber (Shatalin et al., 2021).

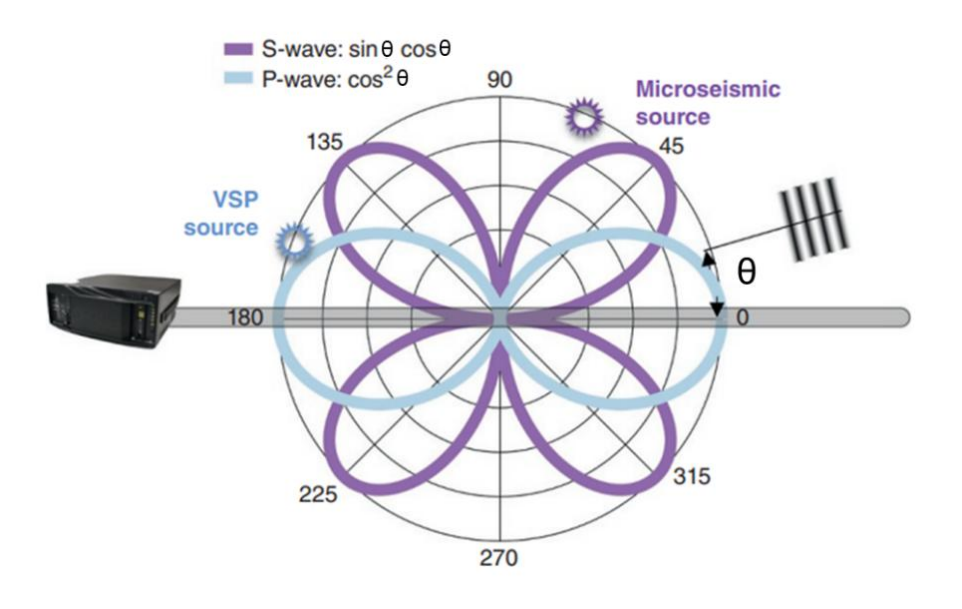


FIG 2.11. DAS with linear optical cable is more sensitive to P-wave in VSP configuration and to S-wave in microseismic events (modified from Shatalin et al., 2021)

From 2010 to 2014, advancements in DAS hardware made it possible to record seismic data with quality comparable to conventional geophones (Bakku, 2015; Daley et al., 2013; Mateeva et al., 2014; Mestayer et al., 2011). As a result, the interpretation of DAS signals drew increased focus. One simple model represents DAS strain rate as the difference between two inertial velocity sensors spaced by the gauge length (Daley et al. 2016). Field validation by Wang et al. (2018) confirmed this concept using earthquake data.

An alternative explanation, based on optical interferometry, links the measured phase shift to the longitudinal strain experienced by the fiber (Lindsey et al. 2020). Optical fading, which refers to reduced amplitudes at quasi-random locations resulting from destructive optical interferometry, and poor coupling of a channel, are indistinguishable except at the scale of the array, where coupling issues are often identifiable by systematic patterns or field installation information (Lindsey and Martin 2021).

Straight fibers exhibit a directional sensitivity, with their response diminishing as $cos^2(\theta)$, where θ is the angle between the seismic P-wave direction and the fiber axis (Benioff 1935). This strong azimuthal dependence, along with complex polarity behavior, differentiates DAS from standard geophones (Lindsey et al. 2017).

Sensor coupling is another critical factor. Laboratory experiments have shown that fiber embedded in loosely bonded or gel-filled metal tubes produces weaker signals than cemented bare fiber (Becker and Ciervo, 2018; Papp et al., 2017). Nonetheless, surface waves, characterized by a retrograde elliptical motion, which results in vertical and horizontal displacements, are regularly detected in practical deployments using fibers placed in shallow trenches (Dou et al. 2017) or even temporarily laid on the surface and weighed down (Spikes et al. 2019).

Just like geophones, which use three orthogonal components to reconstruct the full seismic wave field, DAS can be expanded beyond its single-component nature. While a straight fiber only detects strain along its axis, creative adjustments to fiber layout and geometry have led to configurations capable of capturing directional strain signal. However, traditional DAS setups still face broadside sensitivity—reduced sensitivity to seismic waves arriving perpendicular to the fiber—which remains a fundamental limitation of straight-fiber deployments (Kuvshinov, 2016; Mateeva et al., 2014).

To mitigate this limitation, researchers have explored modifying the geometry of the fiber itself. Altering the layout—from straight to helically wound or other shaped configurations—allows the fiber to sample a broader range of strain directions. This conceptual advance has been supported by a robust theoretical framework.

Innanen (2016) introduced a geometrical model that describes the DAS response for arbitrarily shaped fibers, including complex geometries such as helices wound around curved paths. This model enables the projection of seismic wave fields onto the local tangent vectors of the fiber and supports the generalization of directionality rules—which involves the $\cos \theta$ and $\cos^2 \theta$ responses—to nontrivial geometries. These advancements have established the theoretical foundation necessary for designing DAS arrays capable of capturing multicomponent seismic data.

The first field implementation of these ideas was the "Pretzel" array, designed and deployed by CREWES in 2018 at the CMC - Newell County facility. The Pretzel consisted of two 10×10 m buried square loops of fiber—both straight and helically wound—arranged in orthogonal and diagonal orientations (Innanen et al. 2018). This setup aimed to sample multiple strain directions within the same horizontal plane. Vibroseis sources from multiple azimuths were used to illuminate the array. Analysis confirmed that shaped fibers, when properly oriented and spaced relative to the interrogator's gauge length (typically 5–10 m), could approximate a multicomponent DAS sensor. The directional sensitivity inherent in the fiber geometry allowed the capture of distinct horizontal strain components. However, limitations remained—chief among them the lack of vertical coverage and the inherent spatial extent required for gauge-length constraints, which prevents such arrays from acting as true point sensors.

In addition to directionality, the coupling between the optical fiber and the surrounding soil emerged as a practical challenge, particularly in near-surface applications. Oscillatory motion can be damped by burial and backfilling, but this introduces longer vibration durations compared to standard geophones. Innanen et al. (2019 Aug) showed that shaped fiber arrays could estimate strain tensor components under realistic field conditions, but issues related to the lack of vertical sensitivity, and the footprint of the array persisted.

Inspired by these challenges and recent developments, researchers have sought to miniaturize DAS multicomponent sensors. Takekawa et al. (2022) introduced a prototype consisting of three optical fiber loops wound around a rigid PVC frame to capture horizontal and vertical strain. The frame size is about 20–25 cm, a size chosen to be equivalent to the gauge length of the DAS measurement of about 20 cm (see Figure 2.12). The design successfully functioned as a point sensor and was shown to produce waveforms comparable to those recorded by conventional

geophones. Their results demonstrated that if damping effects are well controlled, DAS sensors can match geophone fidelity and potentially exceed them in multicomponent versatility.



FIG 2.12. Overview of the developed DAS sensor: (a) photo of the DAS sensor. The frame size is about 20–25 cm; the pipe diameter was 32 mm (extracted from Takekawa et al., 2022)

Following this direction, a new prototype known as the "Croissant" was designed and developed in 2022 at Carbon Management Canada's Newell County Facility (Hall et al., 2022). In this case, the experimental directional DAS sensor is a compact 1×1×1 m structure that addressed many of the Pretzel's limitations, including ease of burial for permanent installation and improved coupling. Fiber was wound around small vertical plastic frames and buried, enabling true 3D orientation including vertical components, such as the Takekawa et al. (2022) prototype. Despite using a much longer gauge length (7 m), the Croissant demonstrated meaningful strain-rate measurements along all three axes. Early field and lab tests confirmed that geometrically isolated directional responses could be achieved even at this small scale. Strain-rate data from the Croissant was found to agree well with converted geophone data, suggesting that miniaturized DAS sensors can offer high-fidelity multicomponent recordings.

In parallel with sensor development, efforts continued to compare DAS strain-rate data with traditional seismic instrumentation. At CaMI-FRS, geophones collocated with the Pretzel array

enabled a direct comparison of DAS and velocity-derived strain-rate signals. While DAS amplitudes were generally lower—likely due to installation depth and coupling differences—the temporal and spectral characteristics of the signals were highly comparable. Furthermore, inversion frameworks were developed to estimate horizontal strain-rate tensors (ε_{EE} , ε_{EN} , ε_{NN}) from directional DAS traces, relying on reconstruction techniques such as least-squares optimization and horizon flattening to address spatial and moveout variations.

In summary, the field has progressed from conceptual models of fiber directionality to real-world demonstrations of shaped fiber arrays acting as distributed multicomponent sensors. The evolution from large horizontal layouts like the Pretzel to compact, vertically integrated devices like the Croissant reflects a broader trend toward scalable, deployable DAS technologies with multicomponent capability.

3. CHAPTER 3. The seismic waves and events in surface datasets

For very small strains, soils exhibit an almost linear strain-stress relationship, so that the assumption of a linear elastic constitutive model is reasonable (Foti et al., 2014).

Two different types of body (or bulk) waves propagate in an unbounded, homogeneous, and linear elastic medium: P-waves (primary or compressional or longitudinal waves) and S-waves (secondary or shear waves). P-waves propagate with particle motion in the same direction of the wave propagation and cause volume change without distortion. They propagate at a velocity greater than S-waves, for which the particle motion is perpendicular to the direction of wave propagation.

The velocities of propagation of seismic waves in a linear elastic solid are associated with the medium's mechanical parameters through simple relationships. Indeed, the mechanical response of an elastic medium is fully characterized by two elastic constants, for example, Lame's constants λ and μ (see equations 3.1). Seismic waves velocities can be expressed with simple relationships between such constants and the material density ρ (Foti et al., 2014).

$$\begin{cases} V_P = \sqrt{\frac{\lambda + 2\mu}{\rho}} \\ V_S = \sqrt{\frac{\mu}{\rho}} \end{cases}$$
 (3.1)

The velocity of propagation of body waves is directly linked to the stiffness of the medium and is not frequency dependent in linear elastic materials. In particular, the velocity of propagation of P-waves is associated with the longitudinal modulus, whereas the velocity of propagation of S-waves is associated with the shear modulus. Equations 3.1 form the basis for the use of seismic waves in material characterization, showing that the elastic constants can be easily determined if the seismic wave velocities are measured experimentally (Foti et al., 2014).

The seismic wavefield is a combination of polarized waves in the three-dimensional (3D) space. The polarization is a characteristic of the wave related to the particle motion. The displacement of particles effected by elastic waves shows a particular polarization shape and a preferred direction of polarization depending on the source properties (location and characteristics) and the Earth structure. P-waves, for example, generate linear particle motion in the direction of propagation; the polarization is thus called linear. Rayleigh waves, on the other hand, generate, at the surface of the Earth, retrograde elliptical particle motion (Labonne et al., 2016).

3.1 Body waves

For P-waves, the only displacement occurs in the direction of propagation along the x axis, as shown in Figure 3.1 for a harmonic P-wave. To this be the case, the wave must be a longitudinal wave, meaning it consists of compressions, causing the medium's particles to move back and forth in the same direction the wave travels. This type of motion is characteristic of P-waves (pressure waves), which push and pull the medium, unlike S-waves (shear waves) that cause perpendicular displacement. Since P-waves introduce volume changes in the material, they can also be termed "compressional" or "dilatational" (Shearer, 2019).

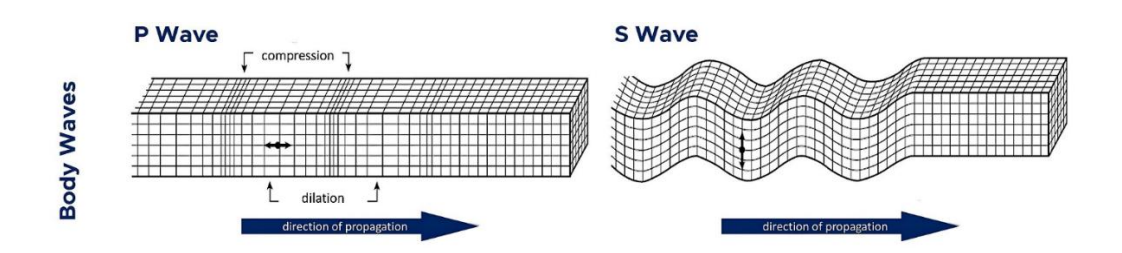


FIG 3.1. Elastic deformations and ground particle motions associated with the passage of body waves: (left) a P-wave; (right) an S-wave (extracted and modified from Kearey and Brooks 1987).

Now consider a plane S-wave propagating in the positive x direction as shown in Figure 3.1, the particle motion is in the y and z directions, perpendicular to the propagation direction. The motion is pure shear without any volume change (hence the name is shear waves). The S polarization may assume any angle within the plane (the wavefront) perpendicular to the wave path. As shown in Figure 3.2, the S-wave particle motion is often divided into two orthogonal

components: the motion within a vertical plane through the propagation vector (SV-waves) and the horizontal motion in the direction perpendicular to this plane (SH-waves). The three particle motion directions are defined with respect to the orientation of the propagation or ray direction and the local vertical axis. The radial and transverse components are orthogonal and both measure horizontal motion, with the radial direction aligning with the horizontal component of the ray direction. Note that SH-waves are purely transverse, whereas both P-waves and S-waves involve both vertical and radial motion, with the relative proportions of each determined by the ray angle from vertical. The SV polarization becomes nearly horizontal as the ray angle approaches vertical, and the SV and SH orientations are undefined for a purely vertically travelling S-wave. Particle motion for a horizontally propagating harmonic S-wave polarized in the vertical direction (SV-wave) is illustrated in Figure 3.2.

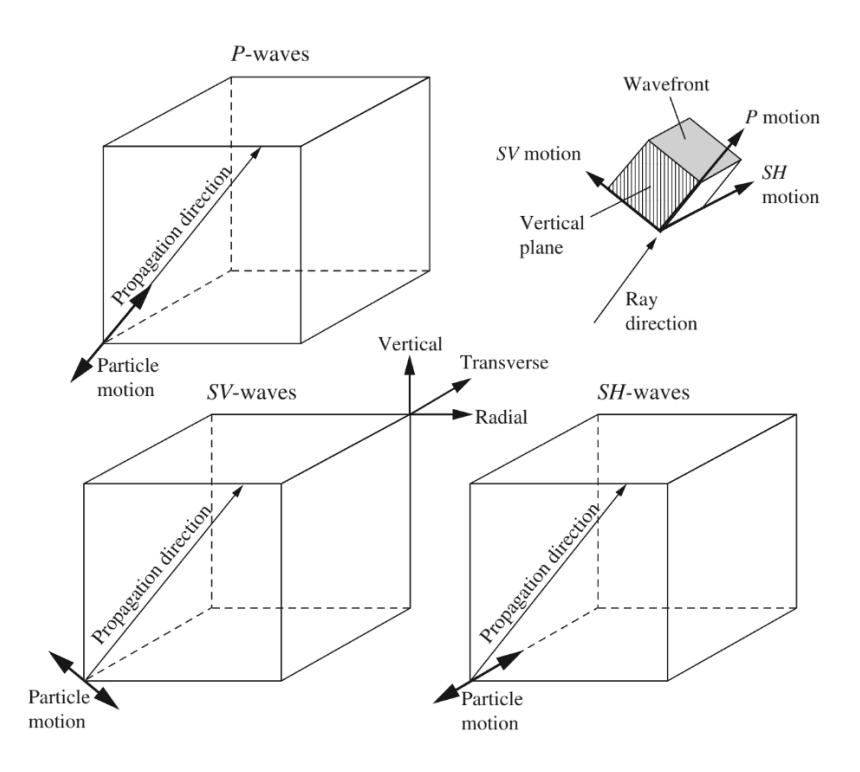


FIG 3.2. Displacement (particle motion) for P-, SV-, and SH-waves with respect to the propagation (ray) direction of the wave. P-wave particle motion is aligned with the ray direction; SV and SH motion is orthogonal to the ray direction. SV motion occurs within a vertical plane through the propagation vector (extracted from Shearer, 2019).

3.2 Surface waves

There are two types of surface waves that propagate along Earth's surface, Rayleigh waves and Love waves. For laterally homogeneous models, Rayleigh are radially polarized (P-SV) and exist at any free surface, whereas Love waves are transversely polarized and require some velocity increase with depth (Shearer 2019).

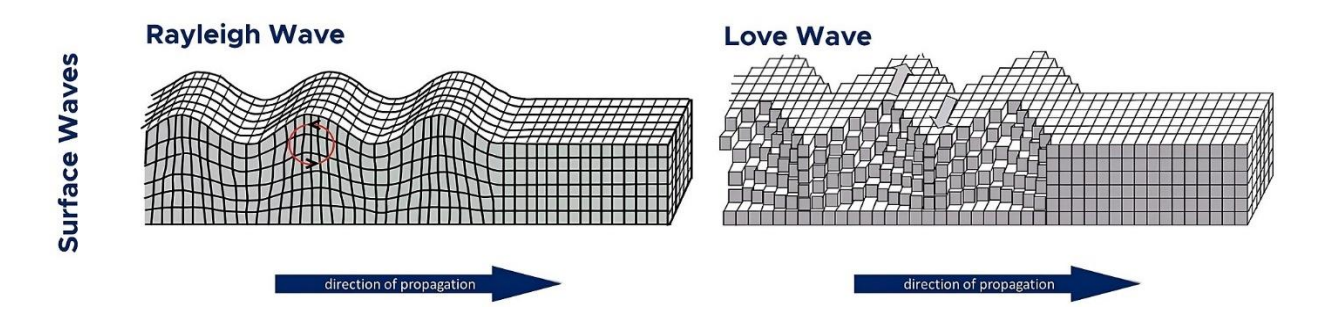


FIG 3.3. Elastic deformations and ground particle motions associated with the passage of surface waves: (left) a Rayleigh wave; (right) a Love wave (extracted and modified from Kearey and Brooks, 1987).

Surface waves are typically the strongest arrivals observed at teleseismic distances and provide valuable constraints on the shallow Earth structure and low-frequency source characteristics. Unlike body waves, surface waves travel more slowly, experience less amplitude decay with distance, where the energy density decays proportionately to 1/r, and the amplitude decays as $1/\sqrt{r}$; and exhibit strongly frequency-dependent velocities (Shearer 2019).

Rayleigh waves, a type of surface wave, involve both vertical and radial particle motion, with amplitudes that decay rapidly with depth. Notably, Rayleigh waves can propagate along the surface of a uniform elastic half-space and do not require an increase in seismic velocity with depth to exist (Shearer 2019).

3.3 Refracted waves

In seismic refraction methods, soil characterization is based on arrival time on the ground surface of seismic waves that have been critically refracted at interfaces among layers having a different velocity (Foti et al. 2014).

In many geological situations, subsurface refractors may approximate planar surfaces over the linear extent of a refraction line. In such cases the observed travel-time curves are commonly assumed to derive from a set of planar layers and are analysed to determine depths to individual planar refractors (Kearey and Brooks 1987). The geometry of refracted ray paths through planar layer models of the subsurface is considered below.

As described by Kearey and Brooks (1987), the general assumption relating to the ray path geometries considered in this section are that the subsurface is composed of a series of layers separated by a plane interface, that seismic velocities are uniform within each layer, that layer velocities increase with depth and that ray paths are restricted to a vertical plane containing the profile line.

Figure 3.4 illustrates progressive positions of the wavefront associated with energy travelling directly through an upper layer and energy critically refracted in a lower layer, from a seismic source at A. Direct and refracted ray paths to a detector at D, a distance x from the source, are also known. The layer velocities are v_1 and v_2 (> v_1) and the refracting interface is at a depth z.

The direct ray travels horizontally through the top of the upper layer from A to D at velocity v_1 . The refracted ray travels down to the interface and back up to the surface at velocity v_1 along slant paths AB and CD that are inclined at the critical angle θ , and travels along the interface between B and C at the higher velocity v_2 .

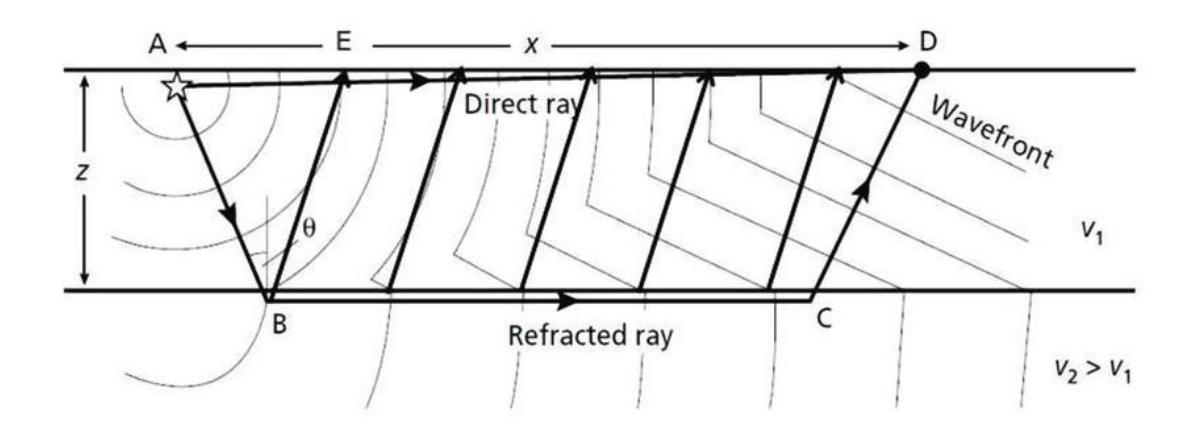


FIG 3.4. Successive positions of the expanding wavefronts for direct and refracted waves through a two-layer model. Individual ray paths from source A to detector D are shown (Kearey and Brooks 1987).

The total travel-time along the refracted ray path ABCD is:

$$t = t_{AB} + t_{BC} + t_{CD} = \frac{z}{v_1 \cos \theta} + \frac{(x - 2z \tan \theta)}{v_2} + \frac{z}{v_1 \cos \theta}$$

Noting that $\sin \theta = v_1/v_2$ (Snell's Law) and $\cos \theta = (1 - v_1^2/v_2^2)^{1/2}$, the travel-time equation may be expressed in the following form:

$$t = \frac{x}{v_2} + \frac{2z(v_2^2 - v_1^2)^{1/2}}{v_1 v_2}$$
 (3.2)

Or

$$t = \frac{x}{v_2} + t_i \tag{3.3}$$

where plotting t against x (Figure 3.5), t_i is the intercept on the time axis of a travel-time curve having a gradient of $1/v_2$. t_i , known as the intercept time, is given by

$$t_i = \frac{2z(v_2^2 - v_1^2)^{1/2}}{v_1 v_2} \tag{3.4}$$

Solving for refractor depth

$$z = \frac{t_i v_1 v_2}{2(v_2^2 - v_1^2)^{1/2}}$$
(3.5)

Thus, the analysis of the travel-time curves of direct and refracted arrivals, v_1 and v_2 can be derived (reciprocal of the gradient of the relevant travel-time curve, see Figure 3.5) and from the intercept time t_i the refractor depth z can be determined.

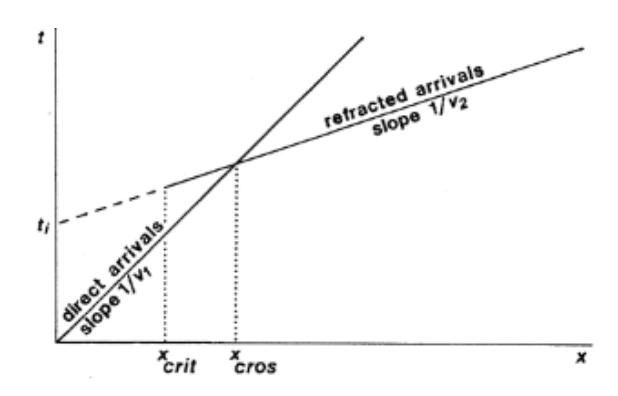


FIG 3.5. Travel-time curves for direct wave and the head wave from a single horizontal refractor (Kearey and Brooks 1987).

Refracted waves start arriving after a critical distance x_{crit} , but they overtake the direct waves at a crossover distance x_{cros} . The critical distance is:

$$x_{crit} = 2z \tan \theta_{crit} \tag{3.6}$$

At the crossover distance x_{cros} the travel times of direct and refracted rays are equal:

$$\frac{x_{cros}}{v_1} = \frac{x_{cros}}{v_2} + \frac{2z(v_2^2 - v_1^2)^{1/2}}{v_1 v_2}$$

Thus, solving for x_{cros}

$$x_{cros} = 2z \left[\frac{v_2 + v_1}{v_2 - v_1} \right]^{1/2}$$
 (3.71)

From this equation it may be seen that the crossover distance is always greater than twice the depth to the refractor.

3.4 Geometric spreading and attenuation

Changes in seismic wave amplitude that result from geometric spreading of wavefronts and the reflection and transmission coefficients that occur at discontinuities. A third factor that affects amplitudes is energy loss due to anelastic processes or internal friction during wave propagation (Shearer 2019). The word attenuation is also sometimes used to simply to describe the general decrease in amplitude of seismic waves with distance, which is primarily a result of geometric spreading (Shearer 2019).

The familiar law of conservation of energy, when applied to a spherical wavefront emanating from a point source in a uniform lossless material, tells us that the intensity diminishes as the inverse square of the radius of the wave front (Figure 3.6a). Translated into the type of measurements made in seismic work, this says that the pressure amplitude of the seismic wave is inversely proportional to the distance travelled. However, the earth is not uniform, and in the presence of an increase of seismic velocity with depth the wavefronts are generally not spherical. Therefore, the amplitude decay is subject to an additional effect associated with refraction (Figure 3.6b) (O'DOHERTY and ANSTEY 1971).

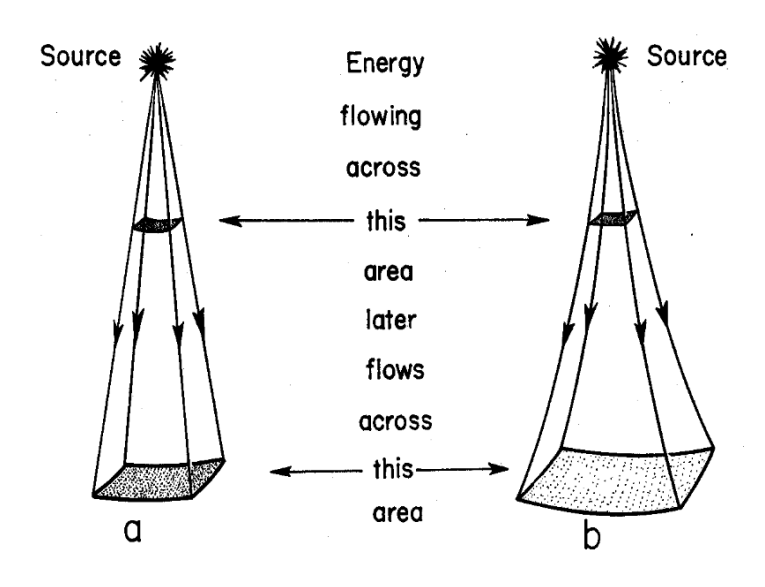


FIG 3.6 Amplitude decay associated with geometric spreading (a) in a uniform material (b) in a material whose velocity increases with depth (Obtained from O'DOHERTY and ANSTEY, 1971).

In a homogeneous medium, energy density decays proportionately to $1/r^2$, where r is the radius of the wavefront for body waves, wave amplitude is proportional the square root of energy density, it decays as 1/r (Shearer, 2019; Yilmaz, 2001). In contrast, for surface waves, the energy density decays proportionately to 1/r, which means that the amplitude decays as $1/\sqrt{r}$.

4. CHAPTER 4: Experimental data Location and Acquisition

To provide essential context for this study, it is important to understand both the geographical location and the geological characteristics of the study area.

4.1 Project Location

The research was conducted at the Carbon Management Canada (CMC) Newell County Facility, a pilot-scale site located approximately 200 km southeast of Calgary, near the town of Brooks in Newell County, southern Alberta, Canada.

Carbon Management Canada (CMC) is an Alberta-based, not-for-profit organization specializing in research and development related to carbon capture and storage (CCS). Through its Containment and Monitoring Institute (CaMI), and in collaboration with the University of Calgary, CMC operates the Field Research Station (FRS) at this site.

The FRS serves as a comprehensive research hub, equipped with a wide array of advanced geophysical and geochemical monitoring technologies. These include, among others, fiber-optic sensors that enable DAS, which plays a key role in subsurface monitoring and characterization.

4.2 Geological Setting of the Study Area

The Field Research Station (FRS) is situated within the Countess Oil Field, located between the Bow and Red Deer Rivers in a mixed grassland ecosystem in Alberta. This region is part of a glaciated landscape characterized by low-relief plains formed from Laurentide (continental) glacial till. These plains exhibit internal drainage systems and are bordered by incised valleys where Upper Cretaceous bedrock strata are exposed (Fenton et al. 2013).

Geologically, the site is positioned within the Interior Platform Structural Province, a stable region of the Western Canada Sedimentary Basin. The stratigraphy here is predominantly composed of undeformed, Phanerozoic sedimentary successions that are bounded by regional unconformities. Although the overall structural deformation is minimal, localized features may

include warping due to dissolution of Paleozoic evaporite deposits, differential sediment compaction, and occasional faulting in the underlying Precambrian basement rocks.

The weather conditions between winter and summer on the Alberta Plains (e.g., up to 80°C temperature variation between summer and winter, snowfalls, high-speed wind) make the near-surface conditions challenging for active surface seismic but enable us to test the working range of the instrumentation (Macquet et al. 2022).

At the land-based Newell County Facility, one of the challenges Full Waveform Inversion (FWI) faces is the near-surface heterogeneity. The unconsolidated nature of the sediment in proximity to Earth's surface leads to complex seismic wave propagation that is heavily influenced by surface waves, attenuation and dispersion, and spatially varying source signatures. Additionally, there is limited prior information about the near surface that can be used to constrain the inversion (Hu et al. 2024).

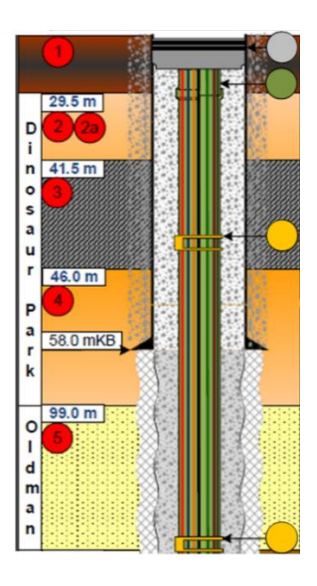


FIG 4.1. Geological Legend: 1) Pleistocene and Holocene (4.9 m KB) 2) Dinosaur Park Formation/Bedrock Surface (29.5 m) 2a) Dinosaur Park Formation, Lethbridge coal zone top (29.5 m) 3) Dinosaur Park Formation, Lethbridge coal zone base (41.5 m) 4) Dinosaur Park, sandy zone (46 m) 5) Oldman Formation (99 m).

Insights into the local stratigraphy are available from well completion data provided by the CMC for Observation Well #2, located approximately 35 meters from the Croissant installation. A lithological profile based on this data is presented in Figure 4.1.

Pleistocene and Holocene layer at least in the top couple of meters - is anisotropic glacial deposits. Primarily fine-grained clay, but with random well-spaced fist to boulder sized rocks in it.

4.3 Introduction to data, acquisition, setting

The DAS data used in this project were acquired from the main fiber loop at the CMC-CaMI Field Research Station (FRS), using an OptaSense ODH4 interrogator capable of continuous data acquisition. The fiber installed, just for the Croissant, is a telecom-fiber, single-mode, specifically the Toneable FTTP Tight Buffered Indoor/Outdoor Drop, Series W7T, with an operational and storage temperature range of –40°C to +70°C.

The fiber loop, approximately 5 kilometers in total length, includes both borehole and trenched segments, arranged in the following sequence:

- 1. Horizontal straight fiber in the northern trench (TN in Figure 4.2)
- 2. Horizontal helical fiber in trench (TH in Figure 4.2)
- 3. Horizontal straight fiber in the southern trench (TS in Figure 4.2)
- 4. Straight fiber in Observation Well 1 (OBS1 in Figure 4.2)
- 5. Straight fiber in Observation Well 2 (OBS in Figure 4.2)
- 6. Helical fiber in Observation Well 2 (OBS2H in Figure 4.2)

Following this configuration, the "Pretzel" and "Croissant" fiber layouts were later integrated into the main fiber loop, as illustrated in Figure 4.2.

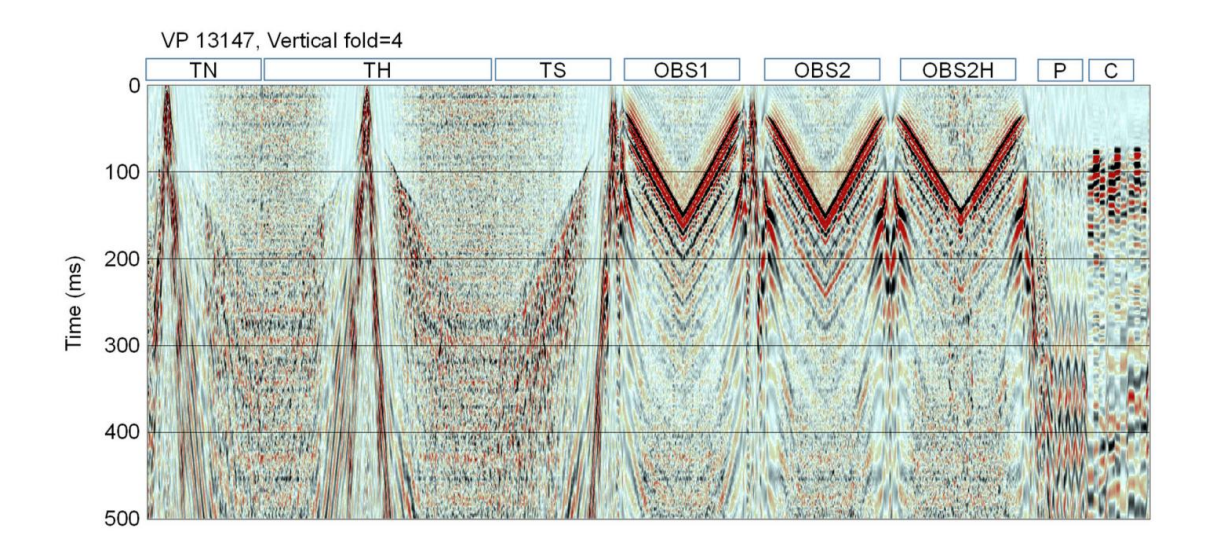


FIG 4.2. DAS experimental data, where TN = straight fiber in northern trench, TH = helical fiber in trench, TS = straight fiber in southern trench, OBS1 = straight fiber in observation well 1, OBS2 = straight fiber in observation well 2, OBS2H = helical fiber in observation well 2, P = pretzel data, and P = traight fiber in observation well 2, P = traight

The data for this study will be limited to the "Croissant" segment, as shown in Figure 4.3. Although the Croissant consists of three stations or sensors, each will be referred to simply as "Croissant" followed by its station number in the following chapters. For example, Station 2 will be referred to as Croissant 2, Station 3 as Croissant 3, and Station 1 as Croissant 1.

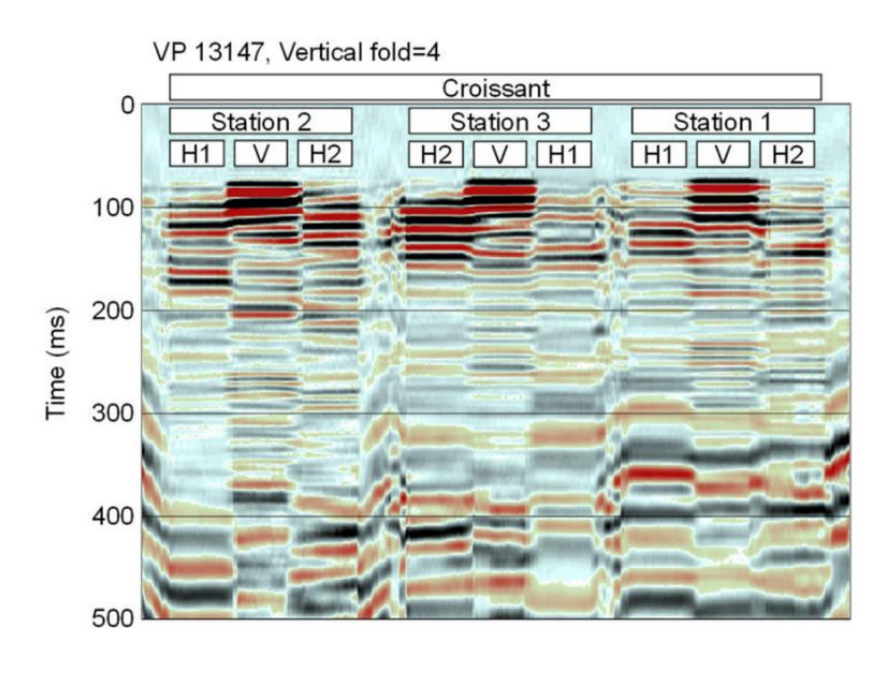


FIG 4.3. Croissant experimental data (Zoomed view of Figure. 4.2), VP 13147, Four stacked and correlated sweeps (16 s sweep, 10-150 Hz) (obtained and modified from Hall et al., 2023)

4.3.1 Croissant Data: Line 41 – P-Vibe

A map of the study area is shown in Figure 4.4. Source Line 41 (red dots) is a circular array of 120 m radius centered on observation well 2 (OBS2) and consists of 24 shots from a P-vibe source. This source line configuration provides a good variety of source-receiver offsets and azimuths for the acquisition. From south-west to north-east, part of Line 13 is also displayed in Figure 4.4, which is a P-vibe source, trenched fiber and geophone receiver line. Zoomed out to the right, is the Pretzel (green), and the three Croissants locations (V's in blue). Croissant horizontal component directions are labelled as CH1 and CH2.

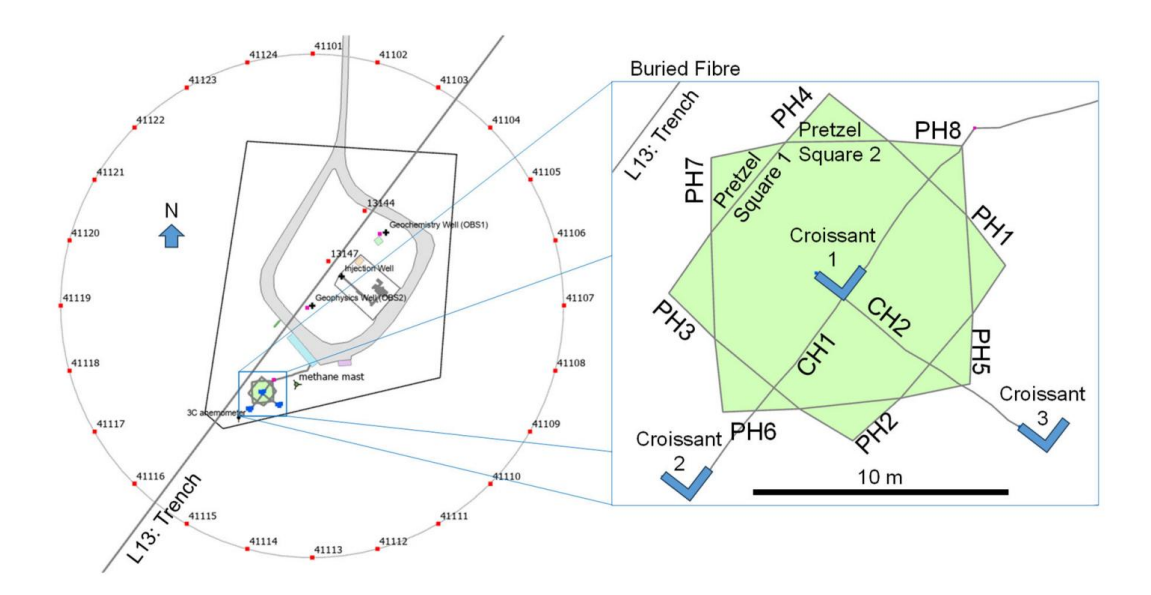


FIG 4.4. Map of field area showing test sweep locations on source lines 13 and 41 (left). Details of the Pretzel (Two 10x10 m horizontal squares at 1.82 m depth; green) and Croissant receiver stations 1, 2, and 3 (0.15 – 1.15 m depth; blue V's) locations are shown on the right (obtained from Hall et al., 2023)

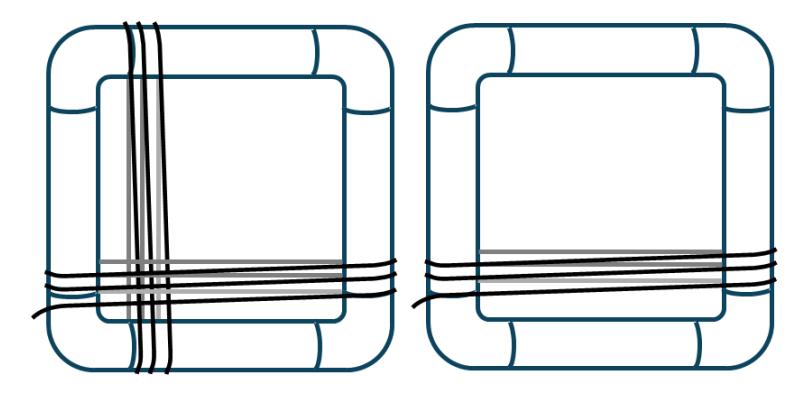


FIG 4.5. Sketch of the optic fiber cable wounded in the plastic frames

Six frames were constructed from 4" diameter PVC pipe. Twenty-eight meters of fiber was used for each component. Twenty-eight meters was chosen for the wrap because it is the same length as four 7 m gauge-lengths. As shown in Figure 4.5 (left), one frame at each Croissant station has two fiber wraps, one horizontal and one vertical. The other frame has just one horizontal wrap (Figure 4.5, right). The wraps are offset from the center of the frames, so the vertical component is close to the junction of the two frames, and the horizontal wraps are as far below the surface as possible. There is no physical connection between the two frames at each station. They are held vertically by the trench, and close to each other by the fill. The fiber is not tensioned and relies on burial compaction for coupling.

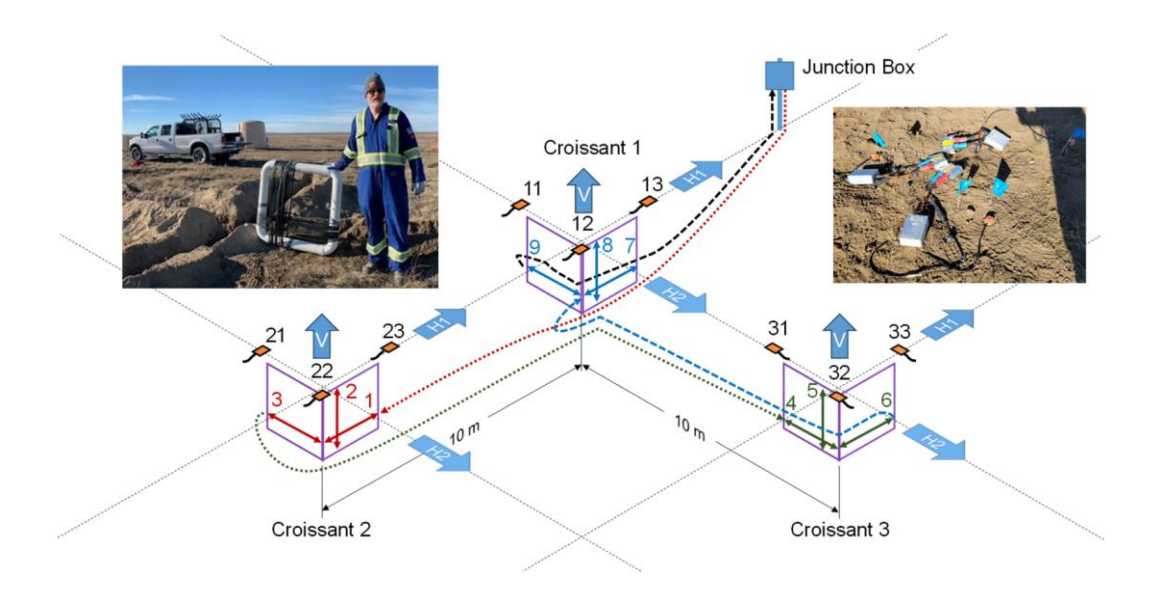


FIG 4.6. Schematic of Croissant install (cf. Figure 4.4). Vertical 1x1 m plastic frames were installed at Croissant stations 2 (fiber wraps 1,2,3), 3 (fiber wraps 4,5,6) and 1 (fiber wraps 7,8,9). Each Croissant component contains 28 m of fiber (4 x 7 m gauge length). Three-component geophones were placed at the corners of the Croissant V's (orange squares) (obtained from Hall et al., 2023).

Figure 4.6 shows a schematic of the Croissant fiber path starting from the junction box (dotted red line), through the trenches, around Croissant plastic frames and its components, and back to the junction box (as dotted black line).

Croissant installation took place over the course of four days in November 2023, which included GPS surveying, digging the trenches, wrapping fiber around six pre-built 1x1 m plastic frames, placing the frames and fiber wraps in the ground and back-filling by hand.

Although nine Inova SM-7 three-component geophones and Hawk nodes were installed near the corners of the frames (three per croissant station), with geophone elements oriented parallel to the frames (orange squares in Figure 4.6) these geophones were picked up before line 41 was shot. During the March 2025 acquisition, these geophones were placed again, and data were recorded.

Seismic acquisition along Line 41 was conducted in 2023, 2024, and 2025 using the University of Calgary's IVI P-EnviroVib source. The first survey took place in November 2023, about one week after the Croissant array was buried and installed. During this acquisition, two sweeps per vibe point (VP) were recorded, with both records stacked to enhance the signal-to-noise ratio. The second survey, conducted in September 2024, aimed to evaluate whether a year of soil and clay compaction around the buried sensors had enhanced data quality. This acquisition used four sweeps per VP allowing the first two sweeps to be stacked to enable direct comparison with the 2023 dataset. Comparing the 2-sweep stacks to the 4-sweep stacks offered additional data to evaluate improvements in signal with increased source effort. The third and most recent survey was conducted in March 2025, using four sweeps per VP, with a continued focus on assessing data quality improvements. Additionally, nine collocated geophones were integrated into the acquisition to allow for cross-comparison between conventional geophone and DAS data.

 Line 41 (L41) – P – Vibe

 2023
 2024
 2025

 2 sweeps
 2 sweeps
 4 sweeps
 4 sweeps

Table 4.1. Summary table of Line 41 acquisition for 2023, 2024 and 2025.

4.3.2 Geophone Data: Line 41 – P-Vibe

In the March 2025 acquisition, nine Inova SM-7 three-component geophones and Hawk nodes were installed near the corners of the frames (three per Croissant station) as is shown with the orange rectangles in Figure 4.7. This figure shows the arrangement of geophones relative to the Pretzel and Croissant fiber locations.

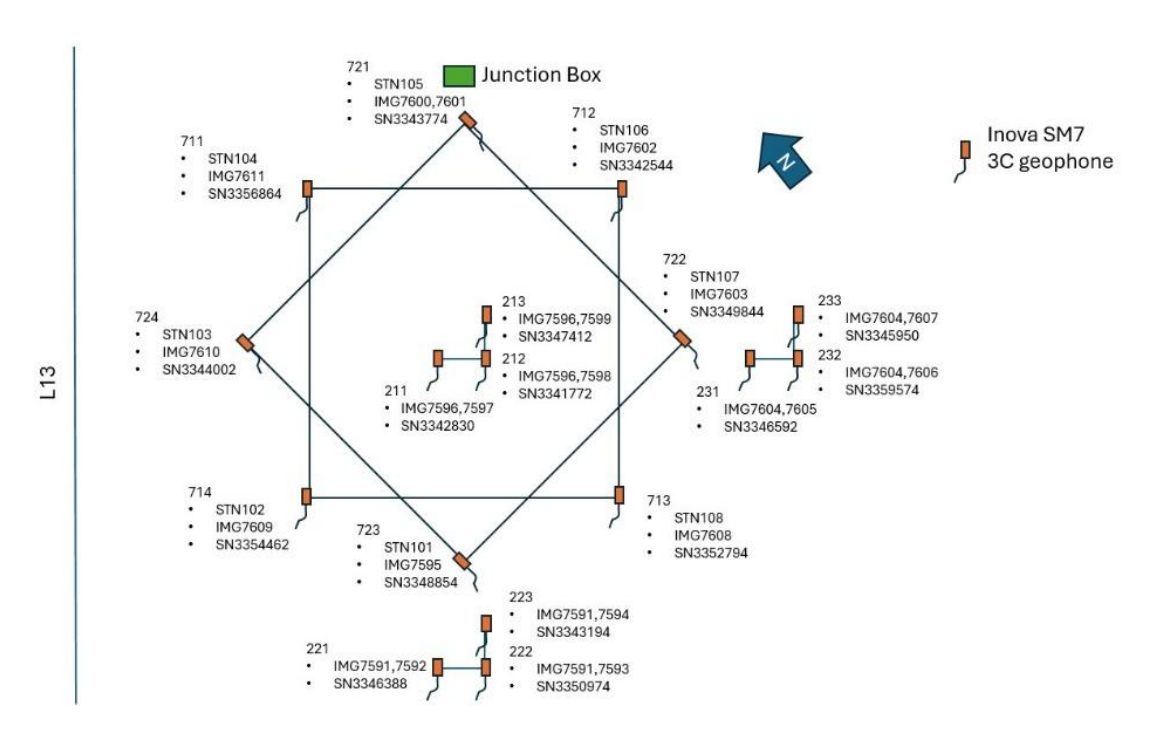


FIG 4.7. Plan view of the Inova SM7 arrangement on the Croissant and Pretzel location.

4.4 Data Processing

For each acquisition—both DAS and geophone—the processing workflow involved stacking the individual sweeps for each Vibroseis Point (VP) and correlating them with a 16-second linear sweep ranging from 10 to 150 Hz. This sweep included a 0.5-second start taper and a 0.25-second end taper to minimize edge effects and spectral leakage.

The stacking step was used to enhance signal quality by suppressing random noise, while the correlation with the reference sweep helped to retrieve the seismic impulse response of the subsurface.

4.5 Qualitative observations for Croissant data L41 - Hypothesis

Figure 4.3 displays the order of the Croissant experimental data beginning with Croissant 2, followed by Croissant 3, and concluding with Croissant 1. In addition to the data recorded along each sensor segment, several connector segments of fiber are also visible. The first connector

segment, shown in Figure 4.6, links the junction box to Croissant 2. Subsequent connector segments connect Croissant 2 to Croissant 3, and Croissant 3 to Croissant 1. Finally, the last connector segment corresponds to the end of Croissant 1 and completes the loop back to the junction box.

To explore the data further, I examined the fiber's response across the three components—two horizontal and one vertical—for all three Croissants, analyzing the full set of twenty-four shots from line 41. Consistent patterns were observed across the three acquisitions conducted in 2023, 2024, and 2025. Notably, the vertical components consistently show strong first-break amplitudes, as evident in Figure 4.3.

Assuming a direct ray path impinging nearly horizontally on the shallow sensors (buried at approximately one meter), we would expect higher amplitudes in the inline horizontal component (H1 or H2, depending on the orientation relative to the source) and lower amplitudes in the crossline horizontal and vertical components. However, the qualitative data from L41 suggests different behavior.

Starting from the premise that the first arrival of seismic energy at a detector offset from a seismic source always represents either a direct ray or a refracted ray (Kearey and Brooks 1987), the observations made may indicate the presence of a refracted ray arriving at the Croissant sensors with a dominant vertical component, as illustrated in Figure 4.8.

This point of view may explain two key features in the data: (1) strong vertical component amplitudes, regardless of source location, and (2) relatively weak amplitudes across both horizontal components. This behavior supports the well-known phenomenon of broadside sensitivity in DAS measurements, where incident wave fields approaching perpendicular to the fiber axis produce minimal recorded strain, particularly for horizontal fiber geometries like those used in the Croissant.

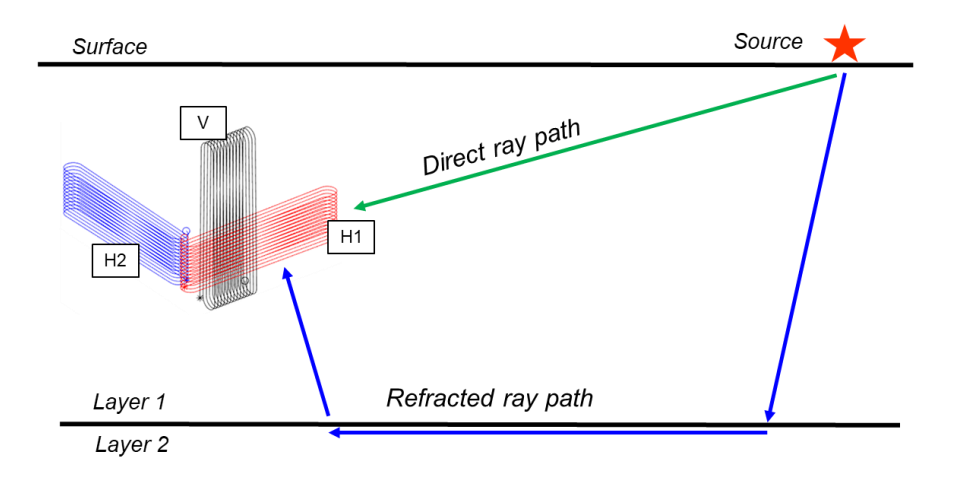


FIG 4.8. Sketch of refracted ray path impinging on the Croissant with a vertical dominant component (blue). Direct ray path impinging on the Croissant with a horizontal dominant component (green)

To further investigate and validate these qualitative observations, the next chapter presents a series of synthetic data modeling experiments. Some questions that I address through this modeling are: do the data acquired make sense? Is the Croissant responding in the way it should? By simulating wave propagation through controlled elastic media and the geometry of the fiber, such as the Croissant, we can better understand the impact of wave incidence on DAS response. These models will help clarify whether the observed vertical amplitude dominance and horizontal attenuation are indeed caused by refracted wave arrivals striking the Croissant from near-vertical angles. Through this approach, the modeling will provide a better basis for evaluating the refracted wave hypothesis and its implications for interpreting the experimental data.

5. CHAPTER 5. Analytical, geometrical and numerical model of the Croissant - synthetic seismograms

To effectively interpret and understand DAS data, it is crucial to develop synthetic models that simulate the physical conditions of the subsurface, accurately represent the geometry of the fiber-optic cable, and capture the fiber's response to seismic sources. These models serve as a reference point for interpreting experimental data and raise important questions: Do the synthetic data resemble what we observe in the field? Are the acquired data physically consistent and interpretable? Addressing these questions helps validate the DAS data, enhances the confidence in the measurements, and clarifies what types of signals can be reasonably expected to be detected.

This chapter begins by introducing an analytical model proposed by (Innanen 2017 Aug 17), offering a workflow for defining fiber geometry and modeling its strain response in a homogeneous, isotropic medium. A simple experiment illustrates a key concept: a straight fiber exhibits broadside sensitivity to an explosive source placed orthogonally to its axis—no strain is recorded due to the geometry of the ray path relative to the fiber. When the same source is applied to a fiber arranged in a helical geometry, however, the strain response becomes detectable. This improvement results from the projection of the seismic strain onto tangential segments of the fiber, enhancing sensitivity.

To translate these observations into a more complex geometry—namely the Croissant layout—a detailed geometric model for the Croissant was developed. This geometric model describes the full fiber trajectory from the junction box (as introduced in Chapter 3). Using this configuration, strain responses were computed for 24 seismic sources. The resulting synthetic shot gathers, generated under the assumption of body-wave propagation along simple ray paths (Innanen et al. 2018), were analyzed to test signal detectability.

Early comparisons with experimental data revealed a key discrepancy: the homogeneous model failed to reproduce the strong vertical component observed in the first arrivals, which initially makes sense due to the incidence angle perpendicular to its axis. This led to the hypothesis that these arrivals may result from refracted waves impinging on the fiber at steep incidence angles.

To test this, I modeled ray paths with dominant vertical components and recalculated the corresponding strain responses, yielding a more realistic interpretation of the early arrival patterns.

To move toward a yet more realistic scenario, a full 3D elastic finite-difference model was implemented using the ElasWave3D software, developed by Sánchez et al., (2025). For the simulation, the input parameters involve a velocity profile of the study area derived from inversion data provided by CMC, along with the spatial coordinates of both the sources and the Croissant-shaped receiver layout. Two types of input wavelets were used: a standard Ricker wavelet and the actual source wavelet from the Vibroseis acquisition. The latter was obtained by cross-correlating the recorded data trace with the Vibroseis sweep, thereby approximating the true source signature used in the field. The output obtained from the ElasWave3D include synthetic shot gathers for the Croissant and geophone locations, which will help to interpret the events, times and velocities observed in the Croissant experimental data.

This chapter serves as the foundation for analyzing synthetic data across multiple computational methods and compares them to real field measurements, providing a robust starting point for hypothesis testing.

5.1 Methods for computing synthetic shot gathers

Implementing techniques for computing synthetic seismic data (seismograms / shot gathers) for realistic Earth models is an important element of seismology. In general, the goal is to calculate what would be recorded by a seismograph at a specified receiver location, given an exact specification of the seismic source and the Earth model through which the seismic waves propagate. This is a well- defined forward modeling problem that, in principle, can be solved exactly. However, it is important to account for the errors associated with deficiencies in the approximations in the theory used and the errors caused by using simplified Earth or source models (Shearer 2019).

Two principal methods are employed in this study:

1. Ray-theoretical methods in which ray geometries are explicitly specified and ray paths are computed. These methods include simple (or geometrical) ray theory. In this project, I apply

- the analytical ray-based model developed by Innanen (2017 Aug 17), suitable for modeling strain along fibers in simplified elastic media.
- 2. Finite-difference and finite-element methods that use computational power to solve the wave equation over a discrete set of grid points or model elements. These have the great advantage of being able to handle models of arbitrary complexity. The ElasWave3D simulator (Sánchez et al., 2025) is used for this purpose, enabling full elastic wave field modeling in a realistic velocity structure.

5.2 Analytical Model – Homogeneous and isotropic medium (Innanen, 2017a)

As described by Innanen (2016), this analytical model—also known as the geometrical model—assumes a fiber-optic cable of arbitrary shape embedded in a homogeneous, isotropic medium defined by an orthogonal coordinate system. The DAS response is modelled via a careful accounting of the fiber geometry in the volume (Eaid et al., 2018;Innanen, 2017; Innanen et al., 2018).

The most important quantity of the fiber geometry is the tangent direction. In straight fiber experiments, where the fiber and the cable are coaxial, strain measurements are made along this direction. However, interrogator units typically report strain as a function of arc-length along the fiber. Therefore, it is important to carefully track the arc-length to accurately associate strain measurements with their spatial coordinates (Eaid et al. 2018).

The analytical model developed by Innanen (2016) consists of six main steps, which are detailed below:

- 1. **Define the Earth volume:** In this step, a rectangular Earth model is defined. Also, elastic properties, including P-wave and S-wave velocities are stated.
- 2. **Define DAS fiber(s):** This section describes the definition of fiber(s), including their length, coordinates, and the vectors describing their trajectory. Depending on the geometry, which may be straight, helical, or—specific to this project—Croissant-shaped, the entire fiber trajectory is modelled. The fiber must be discretized with equally spaced points. The gauge length is also defined here. Furthermore, arc lengths along the fiber as well as tangent, normal,

- and binormal vectors, are computed. These elements are essential for projecting the seismic wave field onto the fiber's axial components in the following steps.
- 3. **Define source and trace features:** The seismic source is defined using a moment tensor, which characterizes the deformation at the source location responsible for generating seismic waves. Additional source parameters are specified, including its spatial location, the dominant frequencies of the P- and S-waves.
- 4. **Define DAS Channels:** This step defines the spacing between DAS channels, expressed in meters. The channel locations correspond to specific segments along the fiber and are used to simulate locations for data acquisition. Gauge length is also defined in this step.
- 5. Compute strain and assign to traces: The distance and travel times between the source and fiber positions are calculated. At each point along the fiber, the strain components due to P- and S-wave arrivals are computed based on the source-fiber geometry and moment tensor. These strain values are projected onto the fiber's axial direction. The resulting projections are then used as spike amplitudes on the data traces at the appropriate arrival times.
- 6. **Compute Final Traces:** Pointwise strain traces along the fiber are extracted and averaged over the gauge length at each channel. These averaged traces are then convolved with the wavelets. The final output includes both P-wave (as shown the shot gathers in Figure 5.1 and Figure 5.2) and S-wave responses, which are combined and recorded as seismic traces in the dataset.

Briefly, the fiber is embedded within a snapshot of a 3D elastic wave field, and its response to strain is computed. The P-wave and S-wave strains form a six-component tensor field each, which is later projected onto the tangential direction of the fiber at each point. The output is a vector of pointwise strain traces along the fiber, each extracted and averaged over the gauge length corresponding to every channel position.

Experiment of broadside sensitivity – Straight and Helical fibers

Before modeling and analyzing the Croissant synthetic data, the first step is to evaluate how broadside sensitivity appears in synthetic DAS data using a simple example: a straight or a helical fiber cable embedded in a homogeneous and isotropic elastic medium. This setup provides a controlled environment to explore the basic behavior of DAS responses.

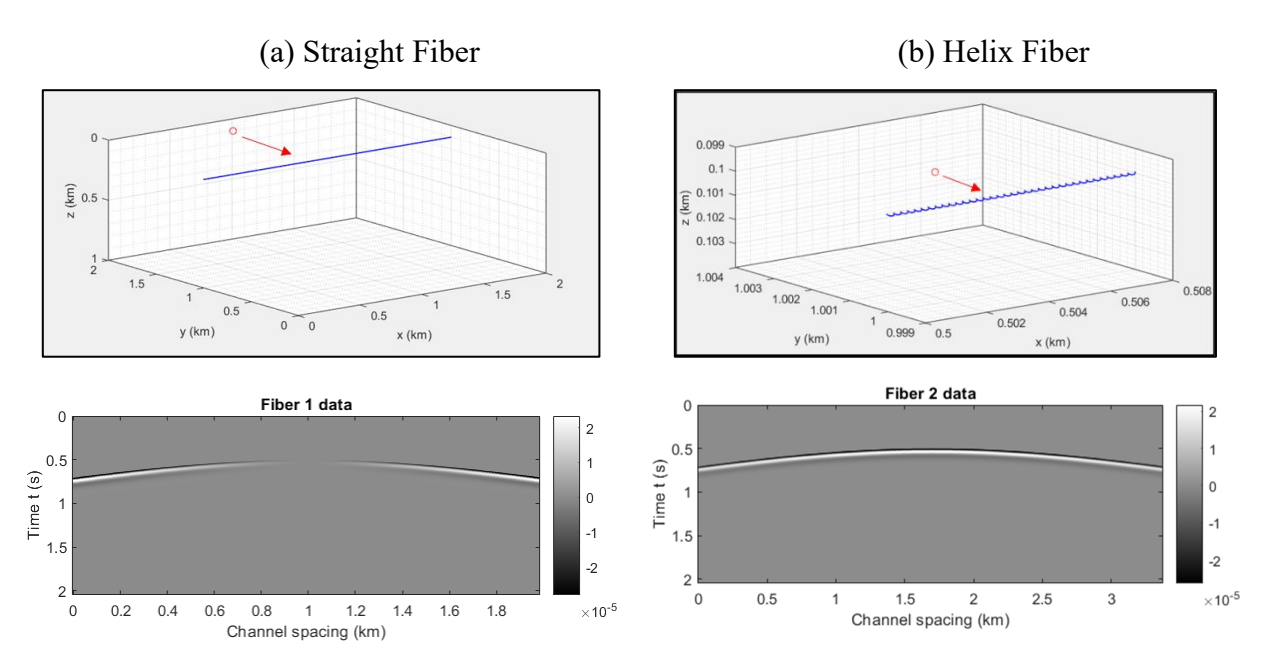


FIG 5.1. (a) Straight and (b) helical fibers lying horizontally, in blue, close to a P-wave source point (red circle). Red arrow points in the radial direction (between the source point and any point on the fiber under consideration. In the second row, the shot gather of the straight (Fiber 1) and helical fiber (Fiber 2).

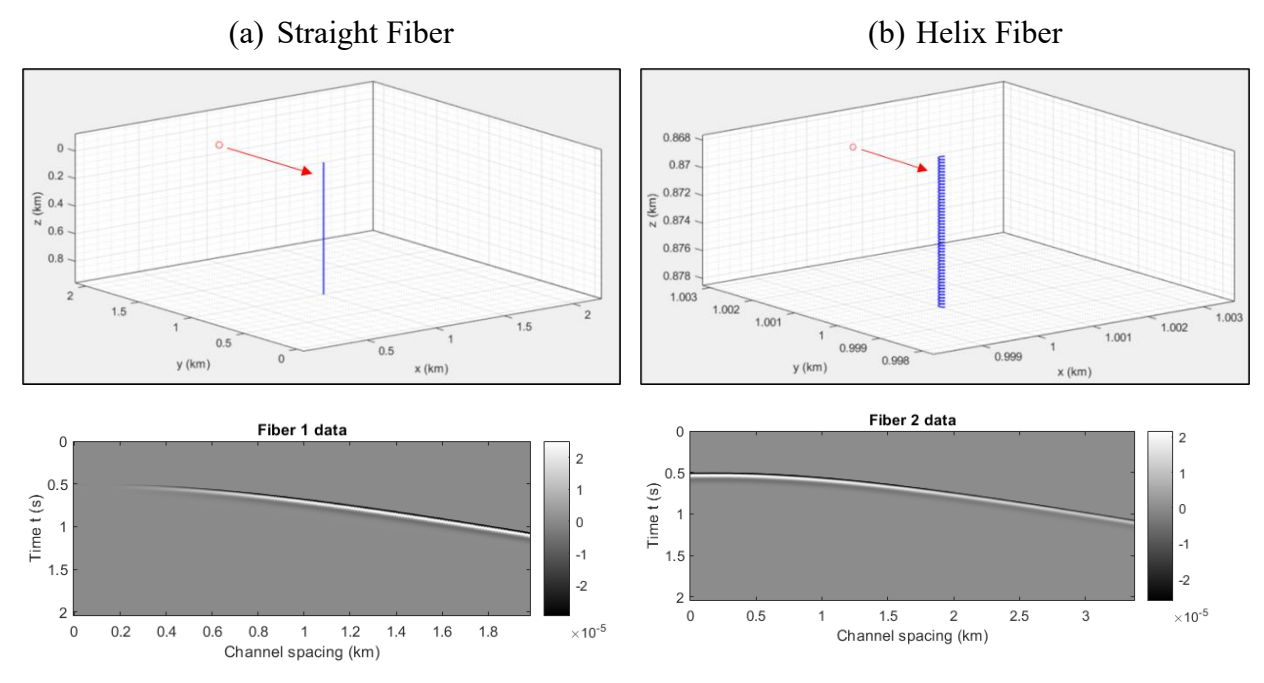


FIG 5.2. (a) Straight and (b) helical fibers laying vertically, in blue, close to a P-wave source point (red circle). Red arrow points in the radial direction (between the source point and any point on the fiber under consideration. In the second row, the shot gather of the straight (Fiber 1) and helical fiber (Fiber 2).

To address and potentially overcome the limitations of broadside sensitivity—where straight fibers show weak responses to wave fields arriving perpendicular to their axis as is shown in Figure 5.1a and Figure 5.2a—alternative fiber geometries have been proposed. Among these, the helical-wound cable (HWC) has gained attention for its ability to capture a broader range of strain orientations, enriching the DAS signal and improving sensitivity to those wave fields arriving perpendicular to the fiber as we can see in Figure 5.1b and Figure 5.2b.

5.3 Geometrical Model of the Croissant

The second step in the analytical model described in Section 5.2 involves defining the geometry of the DAS fiber. This includes determining the fiber's length, spatial coordinates, and the vectors describing its trajectory, which vary depending on the specific layout. In the case of the Croissant shape, a model was developed to accurately represent the position of each segment of the fiber along its curved path.

To construct the geometrical model of the Croissant, I used the dimensions of the plastic frame (Figure 5.3) and the arrangement of the Croissant layout (Figure 4.6). These design details, provided in Hall et al. (2023), were essential for accurately defining the fiber trajectory for the Croissant.

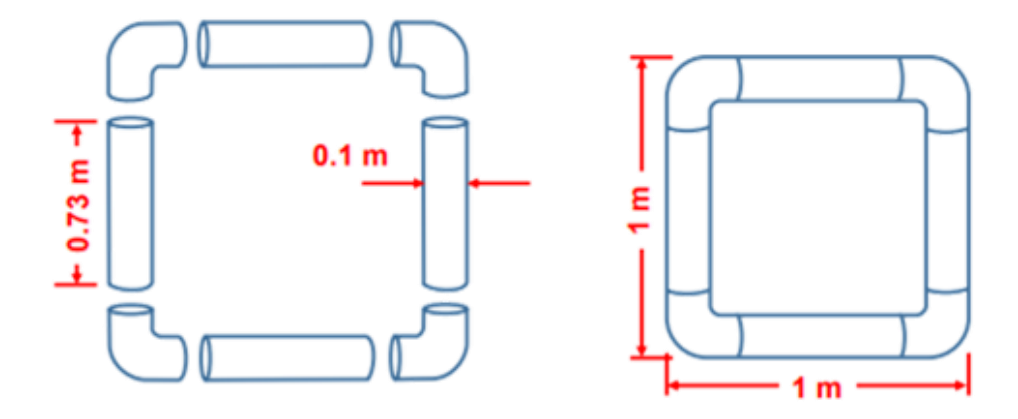


FIG 5.3. Sensors' frame dimensions. The 0.73 m length sides shown will result in a 1 m square for 10.2 cm (4") diameter PVC pipe and corners (from Hall et al., 2022).

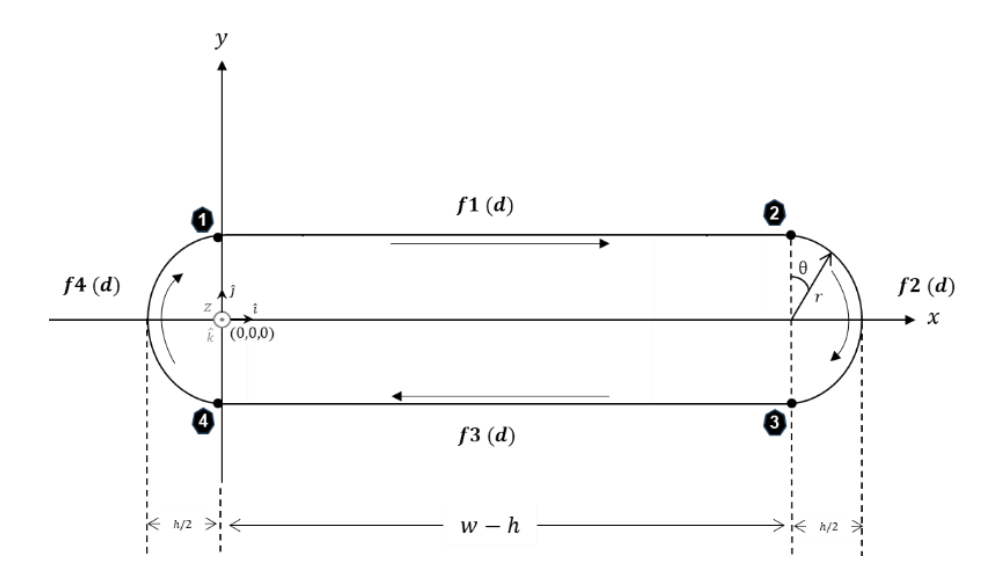


FIG 5.4. Schematic diagram in plan view for the Croissant parametrization with its segments and dimensions

With all layout specifications established, the Croissant fiber path was modeled in MATLAB. The process began by simulating the wrapped cables along invisible frames, incorporating the frame's dimensions. As shown in Figure 5.4, the following parameters were used as inputs:

- Width of the frame (w = 1 m),
- Thickness of the PVC pipe (h = 0.1 m),
- Radius for the semi-circle taken for the wraps/turns (r = h/2),
- Straight segment length (s = w h),
- Constant term for a z variation ($\alpha = 0.01 m$)

A key consideration in any DAS model is ensuring a uniform arc length along the Croissant fiber path, as parameters such as channel spacing and gauge length are critically dependent on it. To address this, the fiber trajectory was parameterized using a constant arc-length step d, allowing for a uniform spatial interval between all fiber segments.

The trajectory was then defined within a field coordinate system consisting of inline (x), crossline (y), and depth (z) axes, along with unit vectors $(\hat{\imath}, \hat{\jmath}, \hat{k})$, The fiber path was expressed

as a discontinuous function, sampled at regular arc-length intervals of d = 0.005 m (5 mm) as showed below in Equation 5.1. Each segment of this function is defined in Figure 5.4.

$$f(d) = f1(d) + f2(d) + f3(d) + f4(d)$$
(5.1)

where:

$$f(d) = \langle x(d), y(d), z(d) \rangle$$
 (5.2)

Equations 5.1 and 5.2 show that the fiber path f(d) depends on the arc-length step d and is defined in a 3D space with three coordinates that define the position of the cable.

Table 5.1 presents the coordinates for points 1, 2, 3, and 4 shown in Figure 5.4, being $d_1, d_2, d_3, d_4, and d_5$ the values of the parametrized function at each point. Below, the function f(d) is defined in 4 segments which will be repeated 14 times to complete the twenty-eight meters of fiber used for each component in the sensors.

Table 5.1. Coordinates for the junction of 4 segments defining the fiber path.

0	2	3	4		
$x_1 = 0$	$x_2 = w - h$	$x_3 = w - h$	$x_4 = 0$		
$y_1 = r$	$y_2 = r$	$y_3 = -r$	$y_4 = -r$		
$z_1 = 0$	$z_2 = \alpha x_2$	$z_3 = z_2$	$z_4 = z_3 + \alpha x_4$		
$d_1 = 0$ $d_5 = d_4 + \pi r$	$d_2 = x_2 \sqrt{1 + \alpha^2}$	$d_3 = d_2 + \pi r$	$d_4 = d_3 + (w - h)\sqrt{1 + \alpha^2}$		

$$x(d) = \begin{cases} \frac{d}{\sqrt{1 + \alpha^2}}, & d_1 < d \le d_2 \\ (w - h) + rsin\left(\frac{d - d_2}{r}\right), & d_2 < d \le d_3 \\ (w - h) - (d - d_3), & d_3 < d \le d_4 \\ -rsin\left(\frac{d - d_4}{r}\right), & d_4 < d \le d_5 \end{cases}$$
 (5.3)

$$y(d) = \begin{cases} r, & d_1 < d \le d_2 \\ rcos\left(\frac{d - d_2}{r}\right), & d_2 < d \le d_3 \\ -r, & d_3 < d \le d_4 \\ -rcos\left(\frac{d - d_4}{r}\right), & d_4 < d \le d_5 \end{cases}$$
 (5.4)

$$z(d) = \begin{cases} \frac{\alpha d}{\sqrt{1 + \alpha^2}}, & d_1 < d \le d_2\\ \frac{\alpha d_2}{\sqrt{1 + \alpha^2}}, & d_2 < d \le d_3\\ \frac{\alpha d_2}{\sqrt{1 + \alpha^2}} + \frac{\alpha (d - d_3)}{\sqrt{1 + \alpha^2}}, & d_3 < d \le d_4\\ \frac{\alpha d_2}{\sqrt{1 + \alpha^2}} + \frac{\alpha (d_4 - d_3)}{\sqrt{1 + \alpha^2}}, & d_4 < d \le d_5 \end{cases}$$
(5.5)

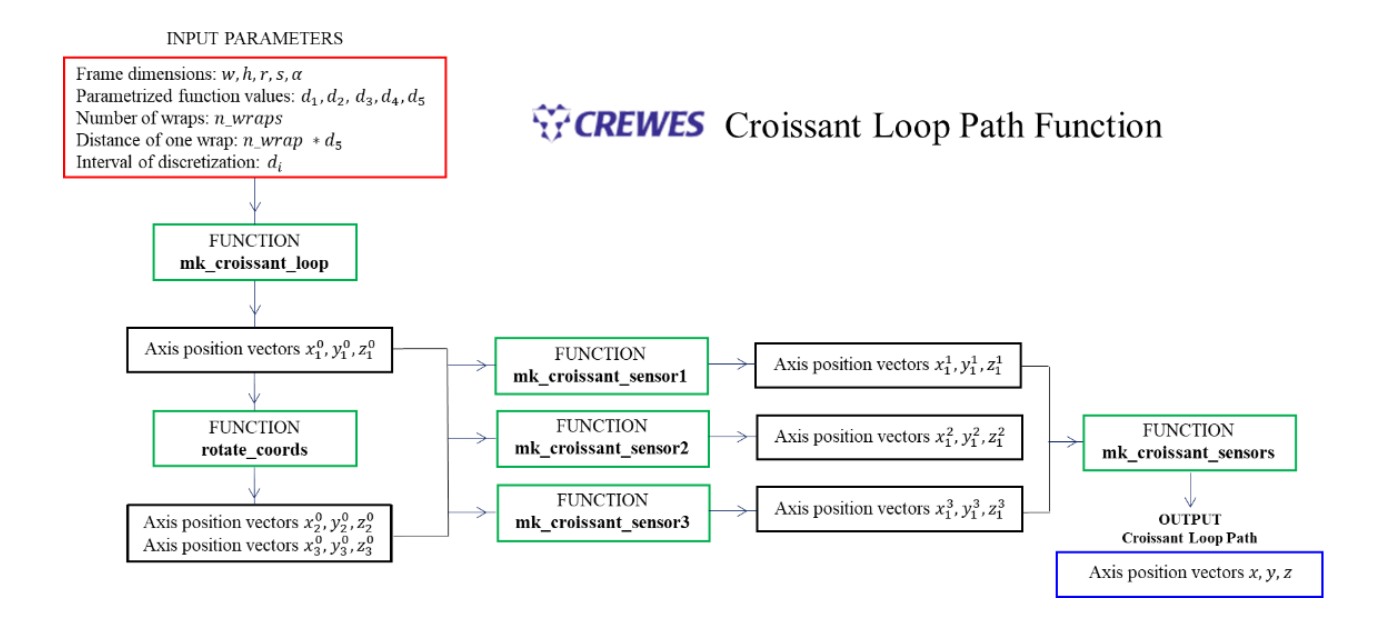
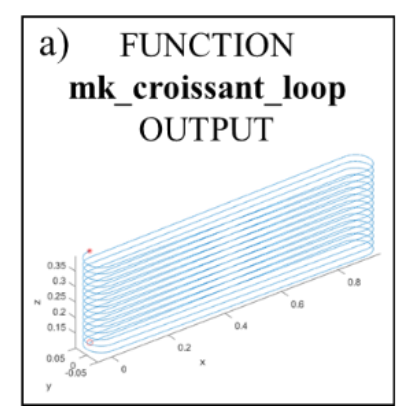
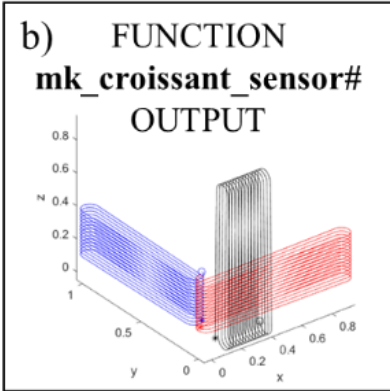


FIG 5.5. Workflow implemented to create the Croissant Loop Path in MATLAB. Input parameters and constants are in the red box, functions in green box, internal outputs in black box and final output of the Croissant Loop Path Function in the blue box.

Figure 5.5 shows the workflow used to create the Croissant Loop Path in MATLAB. Equation 5.2 is defined in the function $mk_croissant_loop$ (see Appendix) which generates three vectors x_1^0, y_1^0 and z_1^0 modeling the twenty-eight meters of fiber for a single component as shown in Figure

5.6a. After applying rotation and translation of those initial coordinates, I used $mk_croissant_sensor\#$ (where #=1, 2, or 3) to obtain a three-component (Figure 5.6b). Then, considering the distances and straight trajectories shown in Figure 4.6 starting from the junction box to Croissant 2 (red cable section), Croissant 2 to Croissant 3 (green cable section), Croissant 3 to Croissant 1 (blue cable section), finishing with the trajectory from Croissant 1 back to the junction box (black cable section), the Croissant Loop path was built with the function $mk_croissant_sensors$ (Figure 5.6c). Finally, the Croissant Loop Path Function generates a set of three vectors that describe the position in 3D space of the fiber cable.





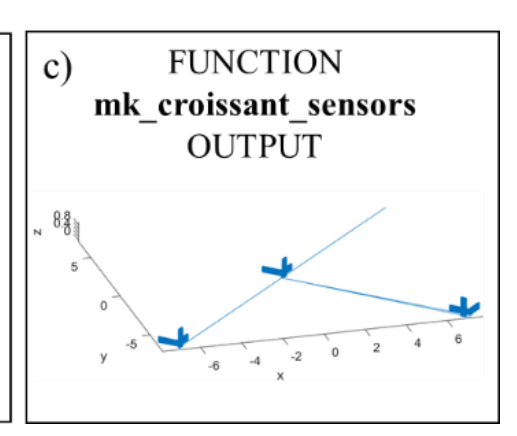


FIG 5.6. Visualization of the internal outputs of the Croissant Loop Path Function. a) output of the mk_croissant_loop function, b) output of the mk_croissant_sensor1, c) output of mk_croissant_sensors which define the complete Croissant Loop Path; in following sections this Croissant Loop Path will be seen as a small "T: in Map View.

The geometrical model of the Croissant was designed to generate data in the same recording order as shown in Figure 4.3. Later, I will refer to "the trajectory of the fiber", this means the trajectory in Figure 5.6c that simulate the trajectory of the fiber as it is displayed in Figure 4.6.

With the fiber trajectory defined and coordinates specified at every 0.001 m of arc length, it was possible to apply the analytical model, as described in the previous section. This enabled the numerical calculation of the tangent, normal, and binormal vectors, which together define an orthogonal coordinate system along the entire fiber path.

An explosive source was modeled using a moment tensor that radiates energy uniformly in all directions. Following the setup used in Line 41, I generated twenty-four shots positioned in a

circular array, equally spaced at a radius of 120 meters, consistent with the layout shown in Figure 4.4.

The gauge length was set to 7 meters and the channel spacing was defined as 1 meter, consistent with the experimental field data.

Synthetic gathers were generated under the assumption that the earliest arrivals at the fiber correspond to body waves transmitting characteristic strain along simple ray paths (Innanen et al. 2018). The P-wave and S-wave velocities, as well as the frequency of the Ricker wavelet used, were not chosen to represent any specific lithology or geological scenario. Rather, they were selected arbitrarily to provide a quick assessment of the strain expected.

Preliminary results were obtained by producing the shot gathers shown in Figure 5.7—using an inline source with the Horizontal 1 (H1) component—and in Figure 5.8—using an inline source with the Horizontal 2 (H2) component.

In Figure 5.7, the connector segments—indicated by the grey box labeled "C"—are visible, as also shown in Figure 4.3. Each component of the Croissant is labeled as V, H1, or H2, indicating the vertical and horizontal orientations, respectively. Positive amplitudes at approximately 5 milliseconds mark the first arrivals of the P-wave. A strong first-break amplitude is observed in the H1 components, dimmed amplitudes in the H2 components, and no signal in the vertical (V) components. The second arrival, at approximately 12 milliseconds, corresponds to the S-wave. This type of body wave oscillates the ground perpendicular to the direction of propagation, contributing to both the inline (H1) and vertical (V) components. In contrast, the crossline components (H2) continue to exhibit weak amplitudes.

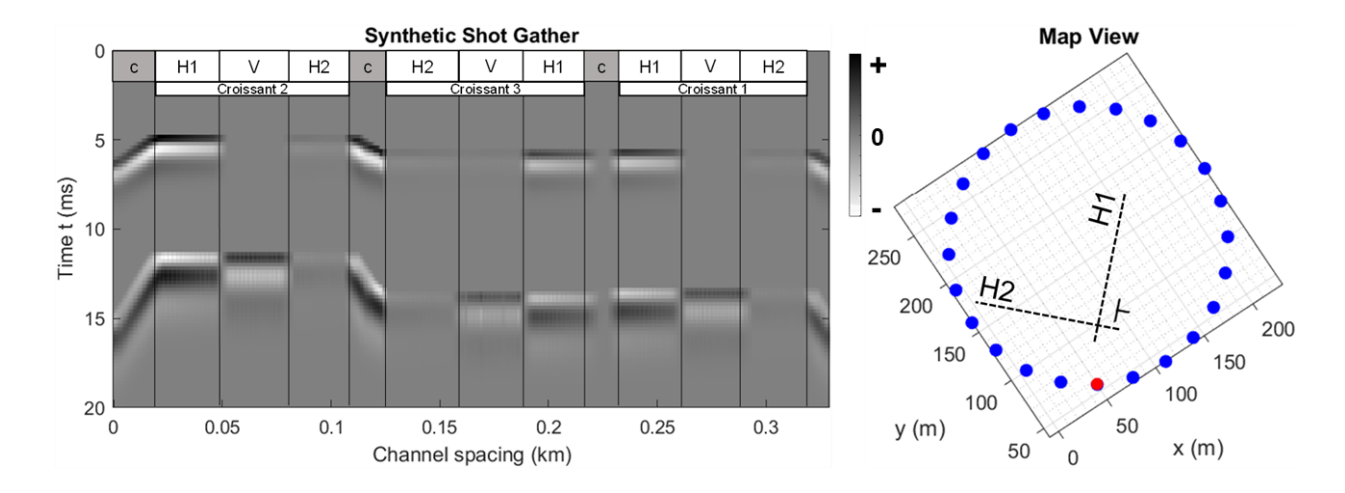


FIG 5.7. Shot gather of the Croissant obtained from the analytical model (left). The map view (right) shows the source-receiver layout, where the trajectory of the fiber is indicated by small black "T" symbol. The orientations of the H1 and H2 components are shown with dotted lines. The red dot marks the source used to generate the shot gather inline with H1 component.

In Figure 5.8, the shot is aligned with the H2 components. As with the previous case, the P-wave arrival shows higher amplitudes in all the H2 components, reduced amplitudes in the crossline components (H1), and no signal in the vertical (V) components. For the S-wave arrival, the behavior is consistent with that observed previously contributing to both the inline (H2) and vertical components, while the crossline (H1) remains weak.

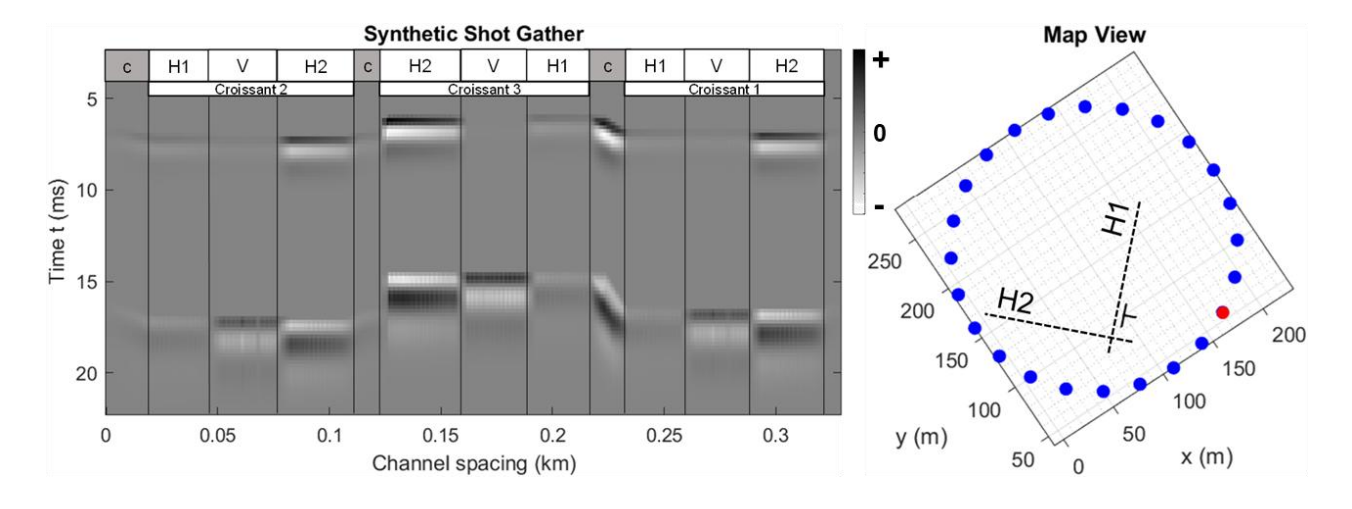


FIG 5.8. Shot gather of the Croissant obtained from the analytical model (left). The map view (right) shows the source-receiver layout, where the trajectory of the fiber is indicated by small black "T" symbol. The orientations of the H1 and H2 components are shown with dotted lines. The red dot marks the source used to generate the shot gather inline with H2 component.

Since the activated source was aligned with the H1 and H2 direction respectively, the measured strain and corresponding first breaks in the sensors are consistent with expectations. The absence of signal in the V component suggests that the particle motion associated with the P-wave was predominantly horizontal, resulting in negligible vertical strain.

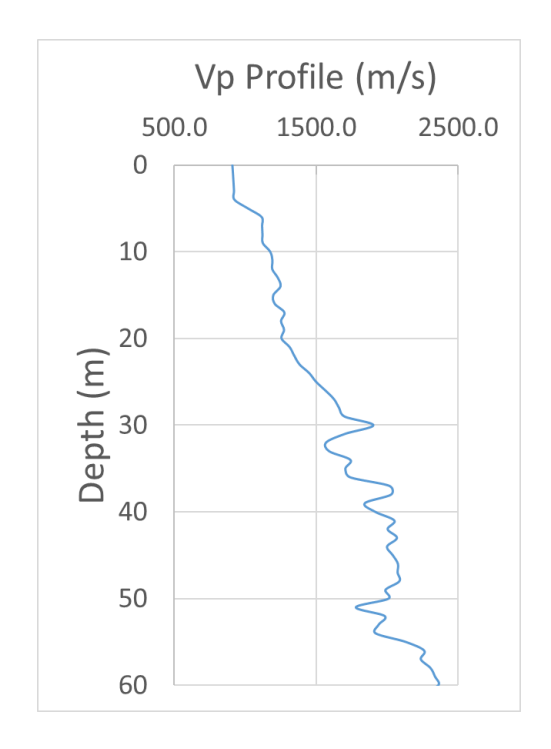


FIG 5.9. P-velocity profile from inversion data (provided by CMC)

Given this observation—and considering the possibility of a refracted wave arrival—modeling the subsurface as a homogeneous medium is unlikely to be the most appropriate approach. In the next section, an incident wave vector with a dominant vertical component is introduced to emulate a refracted ray path. The objective is to assess whether this new wave orientation alters the strain response in the other components.

This approach is supported by Figure 4.1 (Section 4.2), which presents local stratigraphy from geologic data. The figure identifies a bedrock interface at approximately 29.5 meters depth, consistent with a velocity model developed using a rock physics approach (Hu et al. 2021). This model predicted the shallow sections of the velocity and density logs, which were missing from

the original well log data. The results show good agreement with the local geology, including a notable increase in P-wave velocity at around 30 meters, as shown in Figure 5.9.

5.4 Geometrical Model of the Croissant in 2-layers medium

To generate a refracted wave, it is essential to introduce a refractive interface. This can be achieved by assuming the presence of a second subsurface layer with a higher velocity than the overlying layer (i.e., $v_2 > v_1$). This configuration allows refraction to occur according to Snell's Law.

Figure 5.10 shows a plan view of the Croissant, modeled as a point sensor (in blue), and a source point (in red), within a Cartesian coordinate system. From this view, the angle ϕ between the source and the sensor is defined relative to the x-axis, and the distance between them is denoted by L. Figure 5.11 depicts the source-sensor plane, showing the geometry of wave propagation, including the wave direction, refracted ray path, critical angle, and velocity values in each layer.

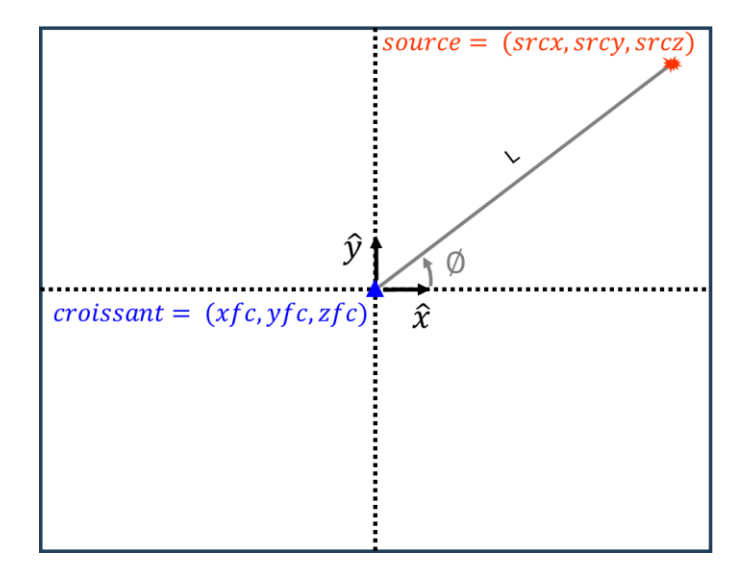


FIG 5.10. Plan view showing the location of a Croissant (blue), representing a point sensor, and a source point (red) in a Cartesian coordinate system. The angle between the point sensor and the source is denoted by \emptyset , measured with respect to the x-axis. L represents the distance between the point sensor and the source point.

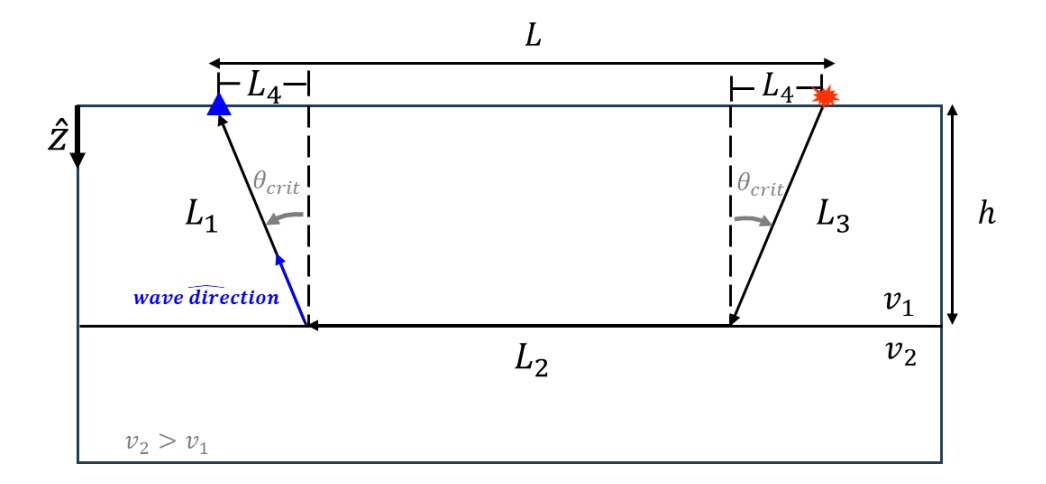


FIG 5.11. Cross-section view of the point sensor—source plane. Relevant distances, wave direction, critical angle, and P-wave velocities in each layer are indicated.

Steps to Compute the Strain Projection to the Croissant

- 1. Define the incident wave vector components in the Cartesian coordinate system in $(\hat{x}, \hat{y}, \hat{z})$.
- 2. Choose P-wave, and wave vector aligned coordinate system $(\hat{w}, \hat{v}, \hat{u})$, where:
 - \widehat{w} : direction of wave propagation (aligned with the wave vector),
 - \hat{v} , \hat{u} : orthogonal to \hat{w}

In this coordinate system, the strain tensor $\varepsilon^{(w)}$ for a P-wave is:

$$\varepsilon^{(w)} = \begin{pmatrix} 1 & 0 & 0 \\ 0 & 0 & 0 \\ 0 & 0 & 0 \end{pmatrix}$$

3. Transform the strain tensor to the global field coordinate system using:

$$\varepsilon^{(field)} = R\varepsilon^{(w)}R^{-1}$$

where *R* is the rotation matrix from the wave-aligned to the global coordinate system.

- 4. For every point along the Croissant, get the tangent vector t(d), which defines the local direction of the fiber.
- 5. Project the transformed strain tensor onto the fiber (as show in Figure 5.12) by computing:

$$\varepsilon_{fiber}(d) = \boldsymbol{T}(d)^T \varepsilon^{(field)} \boldsymbol{T}(d)$$

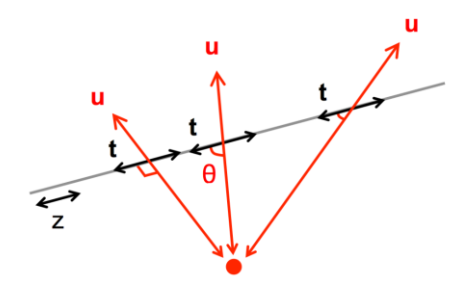


FIG 5.12. Source / straight fiber configuration and visualization of the tangent component of any displacement on the fiber.

This procedure allows the simulation of the strain response observed along the Croissant due to a refracted P-wave incident at an angle with a strong vertical component.

As a result, in Figure 5.13, higher amplitudes in the vertical component can be observed as the first arrival; weaker amplitudes in the H1 component; and no signal recorded in the H2 component.

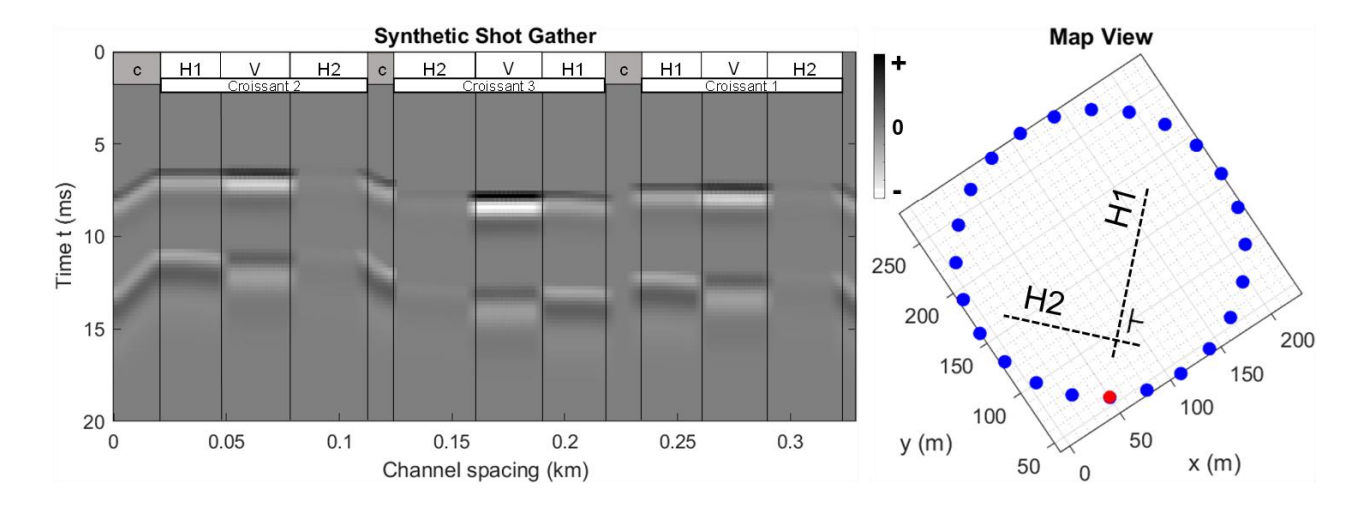


FIG 5.13. Shot gather of the Croissant obtained from the analytical model (left). The map view (right) shows the source-receiver layout, where the trajectory of the fiber is indicated by small black "T" symbol. The orientations of the H1 and H2 components are shown with dotted lines. The red dot marks the source used to generate the shot gather inline with H1 component.

Figure 5.14 also shows high amplitudes in the vertical component, along with significant amplitudes in the H2 components.

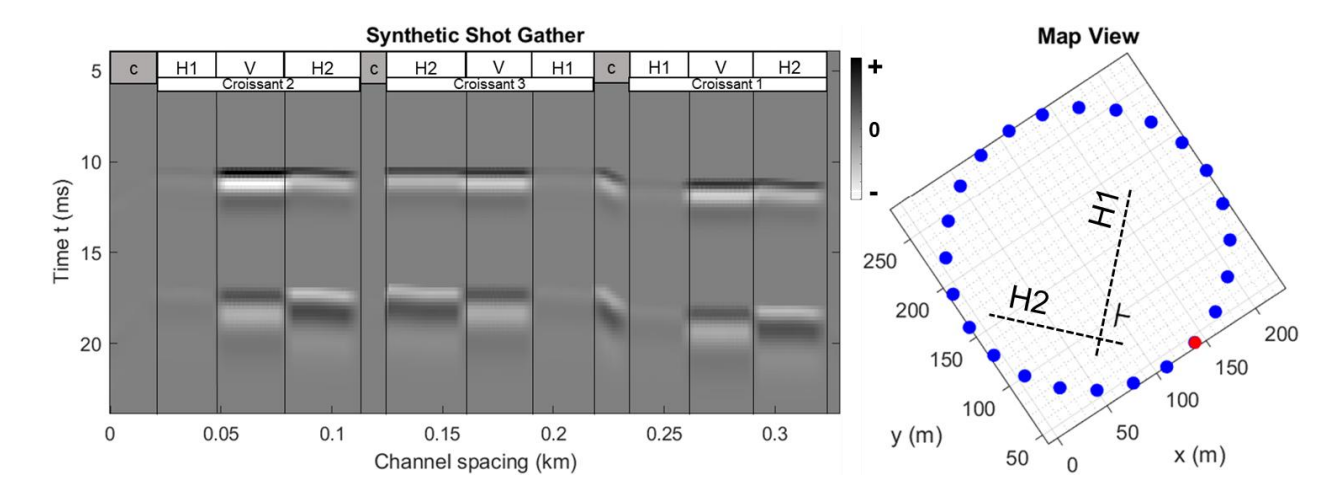


FIG 5.14. Shot gather of the Croissant obtained from the analytical model (left). The map view (right) shows the source-receiver layout, where the trajectory of the fiber is indicated by small black "T" symbol. The orientations of the H1 and H2 components are shown with dotted lines. The red dot marks the source used to generate the shot gather inline with H2 component.

The analytical model of the Croissant geometry in both homogeneous and two-layer isotropic media has demonstrated how the direction of wave propagation influences the recorded strain response. In the homogeneous case, P-wave arrivals produced strong signals in the components aligned with the source direction, while the vertical components showed no significant signal. However, by introducing a refracted ray path with a dominant vertical component, the simulated strain response changed noticeably, producing clear first arrivals in the vertical components and highlighting the directional sensitivity of the fiber. These later results more closely resemble the initial observations from the experimental data.

To advance toward a more realistic representation of the subsurface and recorded data, the next section presents a 3D elastic finite difference model. This implementation integrates the Croissant's geometrical model, the circular source layout from Line 41, and a velocity model derived from inversion of the study area.

The goal of this modeling step is to corroborate the strain rate response observed in the experimental data using a more complex and realistic simulation. By incorporating an approximate velocity model representative of the FRS, this approach aims to assess how well the synthetic response replicates the characteristics of the recorded data. This provides a more robust validation

of the analytical results and offers further insight into the assumptions regarding refracted wave arrivals reflected in the observed strain patterns on the Croissant.

5.5 Numerical Model – Finite Difference 3D Elastic Model

To further expand and validate the analysis of the Croissant, the open-source software ElasWave3D (Sánchez et al., 2025) was employed. ElasWave3D is a GPU-accelerated 3D finite-difference elastic wave solver, capable of generating synthetic seismic data by simulating the propagation of seismic waves. This solver is particularly suitable for both homogeneous and heterogeneous media, offering high-accuracy results. Although originally designed for near-surface applications with complex topographic features, its flexibility allows the integration of the parameters established in previous chapters, making it well suited for the Croissant data simulation.

Initially, the output from ElasWave3D represents conventional three-component (3C) seismic data, simulating what would be recorded by geophones and producing standard shot gathers. However, to replicate the behavior of a Distributed Acoustic Sensing (DAS) system such as the Croissant, it was necessary to project the simulated particle velocity onto the local fiber geometry. This involves computing the strain rate along the tangential vector at each point along the Croissant's path, thereby converting the 3C velocity data into DAS-compatible strain rate measurements.

Starting from the strain rate tensor defined as:

$$\varepsilon_{ij} = \frac{1}{2} \left(\frac{\partial v_i}{\partial x_j} + \frac{\partial v_j}{\partial x_i} \right); (i,j) \in (x,y,z)$$

this quantity is computed from the velocity grid output of ElasWave3D using a finite-difference approximation. The goal is to derive the strain rate projected along the local tangential direction of the fiber, denoted ε_{ij} , which represents what a DAS system would record. To generate then a model of the local DAS fiber response, the strain rate tensor $(\hat{x}, \hat{y}, \hat{z})$ must be transformed into the local system describing the fiber, which the tangential component is extracted.

To transform the full strain rate tensor into the local fiber coordinates, the analytical tangents to the Croissant fiber were computed using derivatives of the parametric equations that define the fiber geometry (Equations 5.3, 5.4, and 5.5). The resulting expression gives the tangential direction T(d) as a function of arc length d, and is defined according to the curvature and orientation of the Croissant:

$$T(d) = \begin{cases} \left(\frac{1}{\sqrt{1+\alpha^2}}, 0, \frac{\alpha}{\sqrt{1+\alpha^2}}\right); & d_1 < d \le d_2, \\ \left(\cos\left(\frac{d-d_2}{r}\right), -\sin\left(\frac{d-d_2}{r}\right), 0\right); & d_2 < d \le d_3, \\ \frac{1}{\sqrt{1+\alpha^2}}\left(-\sqrt{1+\alpha^2}, 0, \alpha\right); & d_3 < d \le d_4, \\ \left(-\cos\left(\frac{d-d_4}{r}\right), \sin\left(\frac{d-d_4}{r}\right), 0\right); & d_4 < d \le d_5, \end{cases}$$
(5.6)

The global coordinate system remains fixed throughout, but the local fiber coordinates vary with arc-length d. The projection of the full strain rate tensor onto the fiber's tangential direction gives the DAS-recorded strain rate:

$$\dot{\varepsilon_{tt}}(d) = (\hat{t} \cdot \hat{x})^2 \dot{\varepsilon_{xx}} + (\hat{t} \cdot \hat{y})^2 \dot{\varepsilon_{yy}} + (\hat{t} \cdot \hat{z})^2 \dot{\varepsilon_{zz}} + 2(\hat{t} \cdot \hat{x})(\hat{t} \cdot \hat{y}) \dot{\varepsilon_{xy}} + 2(\hat{t} \cdot \hat{x})(\hat{t} \cdot \hat{z}) \dot{\varepsilon_{xz}} + 2(\hat{t} \cdot \hat{y})(\hat{t} \cdot \hat{z}) \dot{\varepsilon_{yz}}$$

where $t = (t_x, t_y, t_z)$ is the local unit tangent vector at position d are components of the strain rate tensor computed from the particle velocity grid.

As a user of ElasWave3D, various parameters were introduced; and several key input parameters were consistently adjusted across all following experiments presented in this chapter. These parameters include:

- 1. **Model dimensions:** The size of the 3D domain through which elastic waves propagate and spatial step size.
- 2. **Velocity model:** The distribution of seismic wave velocities, included P-wave, S-wave velocities and density.

- 3. **Modeling parameters:** These include the total simulation time shot gather time recording; defined spatial step size.
- 4. **Source wavelet:** Two different wavelets were employed in the simulations:
 - 4.1 **First simulation:** A zero-phase theoretical Ricker wavelet with a central frequency of 40 Hz was used (Figure 5.15).

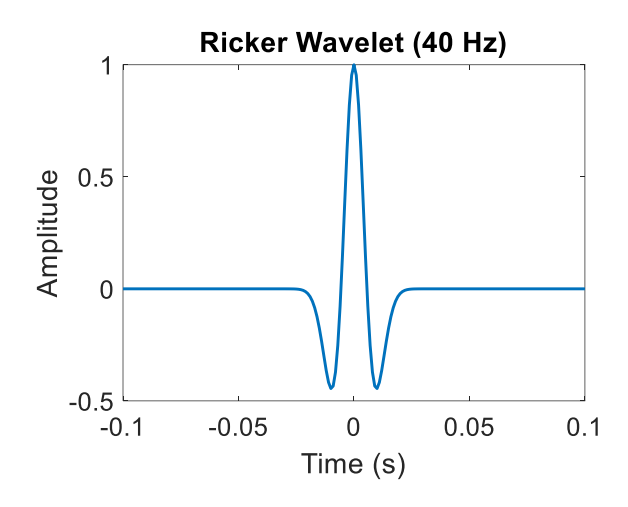


FIG 5.15. Ricer wavelet. Frequency content of 40 Hz.

- 4.2 **Second simulation:** A raw cross-correlated wavelet was derived from experimental data by cross-correlating the source sweep signal used in the field. This wavelet contains frequency content ranging from 10 to 150 Hz (Figures 5.16a and 5.16b, respectively). To use this raw wavelet as input, several preprocessing steps were required:
 - Low-pass filtering: Frequencies above 60 Hz were filtered using a low-pass filter (Figure 5.16d), to reduce computational cost and avoid numerical dispersion.
 - **Cropping:** The first 300 ms were cropped from the original signal, which was sampled at 0.002 seconds. The total cropped duration was approximately 600 ms, resulting in a wavelet whose peak occurs at 0.4 seconds (Figure 5.16c).
 - Resampling: The wavelet was resampled using a time step of $\Delta t = 4x10^{-5}$ seconds; This resampling step is necessary to satisfy the stability condition for the numerical solution implemented in ElasWave3D (see Equation 17 from Sánchez et al., 2025).

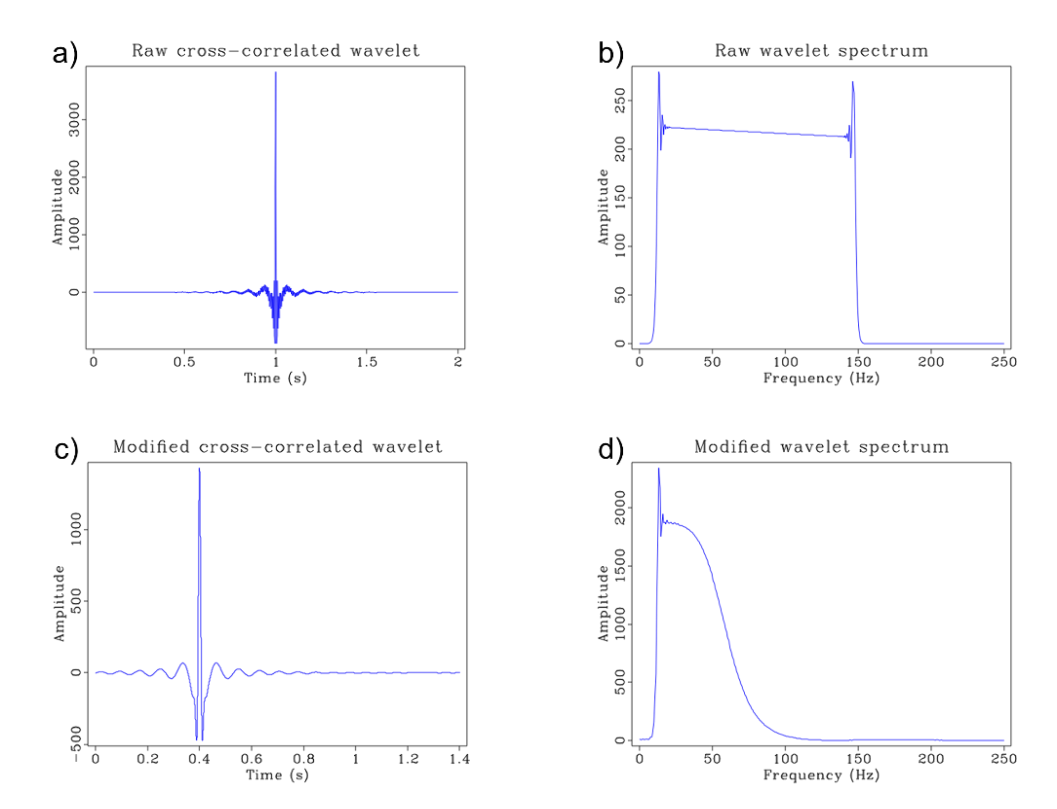


FIG 5.16. Cross-correlated wavelet from sweep; a) Raw cross-correlated wavelet; b) Raw wavelet spectrum, initial frequency content: 10-150 Hz; c) Modified cross-correlated wavelet with low-pass filter of 60 Hz applied, cropped 0.6 s, and resampled; d) Modified wavelet spectrum, frequencies content 0-60 Hz.

- 5. **Geophone receivers' coordinates:** Traditional geophone receiver locations were defined to enable interpretation of seismic events in the conventional geophysical framework. These coordinates were strategically positioned so that the geophone line was aligned with the middle of Croissant and source locations, facilitating direct comparison and interpretation of events between geophone and DAS data.
- 6. **Source coordinates:** The spatial locations of all sources used in the simulations were exported from MATLAB and introduced into the model as input file.
- 7. **DAS acquisition parameters:** These include the number of DAS receiver points, the spacing between them, the channel spacing, and the gauge length—parameters that control the spatial sampling and resolution of the DAS system.
- 8. **Receiver coordinates:** These were derived from the geometrical model of the Croissant presented in Chapter 5.3. The coordinates were exported from MATLAB and introduced into

ElasWave3D as receiver input files. The corresponding tangential vectors, also computed in MATLAB, were used to project displacement fields into axial strain along the fiber path.

These parameters allow for the construction of a realistic elastic model, ensuring consistency across all simulations and enabling robust comparisons between synthetic and experimental data.

In the following sections, I will present two simulations. The first is an ideal case: a homogeneous and isotropic medium modeled with a Ricker wavelet (Figure 5.15). The goal is to observe the amplitude behavior in a setting without geological complexity and to identify any expected patterns in how the Croissant should perform under ideal conditions. The second simulation introduces geological complexity, using a homogeneous layered model with a velocity model derived from the rock physics model (Hu et al. 2021) and the cross-correlated wavelet (Figure 5.16c).

5.5.1 1st Simulation: Homogeneous half-space model (Ricker wavelet)

In this first experiment, a homogeneous and isotropic medium was considered, characterized by the following idealized elastic properties:

- o P-wave velocity $(V_n) = 2000 \text{ m/s}$
- o S-wave velocity $(V_s) = 700 \text{ m/s}$
- O Density (ρ) = 2000 kg/m³

These values were selected as reference parameters, not intended to represent any specific lithology. Instead, they define an idealized medium that allows for controlled analysis of wave propagation behavior without geological complexity.

For this experiment, a 40 Hz Ricker wavelet was used. The gauge length was set to 7 meters, and the channel spacing to 1 meter. Figure 5.17 shows a synthetic shot gather generated with Elaswave3D. In this example, the source is aligned with the H1 component, and no Automatic Gain Control (AGC) was applied. The connection segments are visible and labeled with "c," along with the three Croissant components.

In this model, a direct wave propagating from the source to the sensors is expected. However, a first arrival is visible in the vertical component, which was not expected and was not observed in Section 5.3. However, this may be attributed to particle motion in the model that contributes to the vertical (axial) component and the proximity of the shot. The H1 component of the three Croissants presents higher amplitudes compared to the H2 component. Around 100 ms, surface waves with higher amplitudes become prominent and are better visualized in Figure 5.18. This figure displays the H1, V, and H2 traces, clearly showing the first breaks and surface waves across all three components, noticing the amplitude relationships and differences among them.

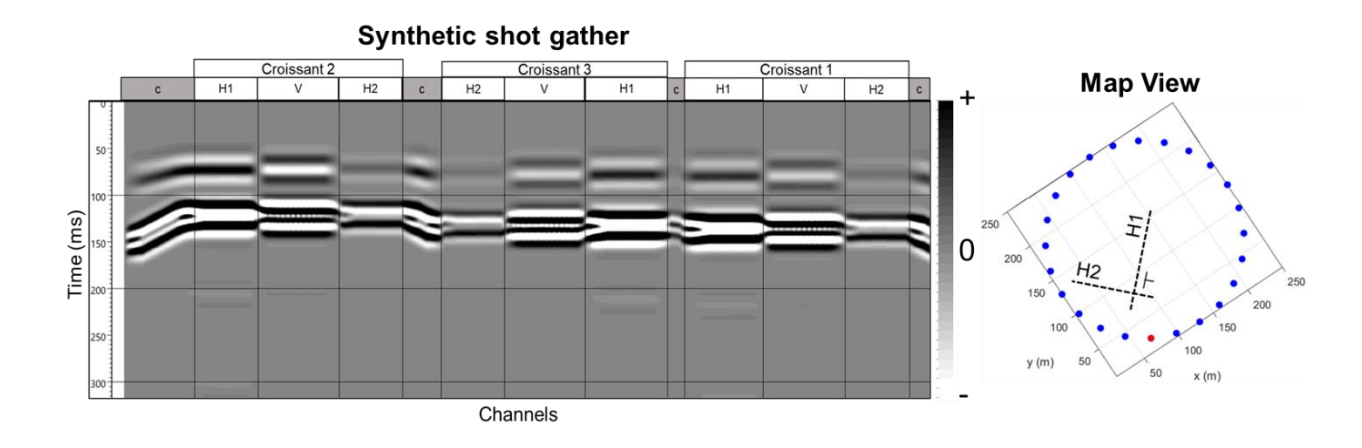


FIG 5.17. Shot gather of the Croissant obtained from the finite difference model (left). The map view (right) shows the source-receiver layout, where the trajectory of the fiber is indicated by small black "T" symbol. The orientations of the H1 and H2 components are shown with dotted lines. The red dot marks the source used to generate the shot gather inline with H1 component.

Figure 5.19 presents another shot gather; in this case, the source is aligned with the H2 component. Compared to the previous shot in Figure 5.17, this gather has a larger source-receiver offset, and the amplitudes of the first arrivals have decreased significantly. The first arrival is still visible—though with diminished amplitudes—on the vertical component. The H2 component shows the highest amplitudes, as expected due to the source orientation, while the H1 component displays very low amplitudes, not visible in this representation. Additionally, all three components exhibit increased amplitudes for the surface waves. Among them, the H1 component shows the

weakest response, followed by the vertical component, with the H2 component displaying the strongest surface wave amplitudes.

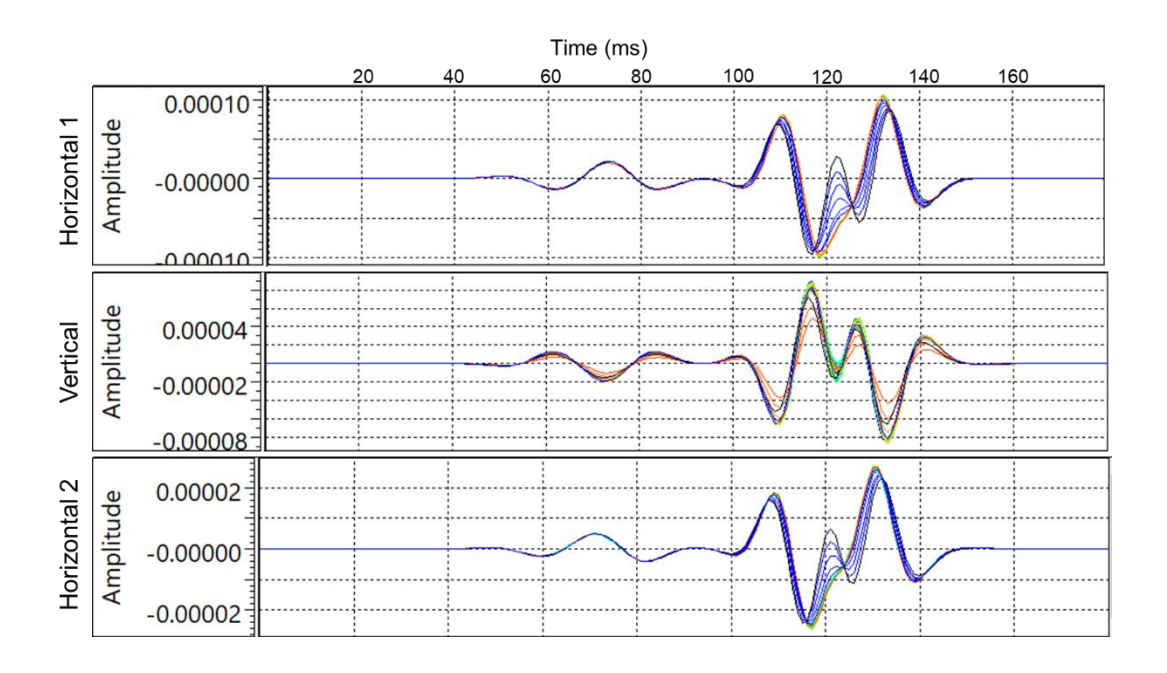


FIG 5.18. In blue, average trace amplitudes for the three components, H1, V, and H2 for Croissant 2.

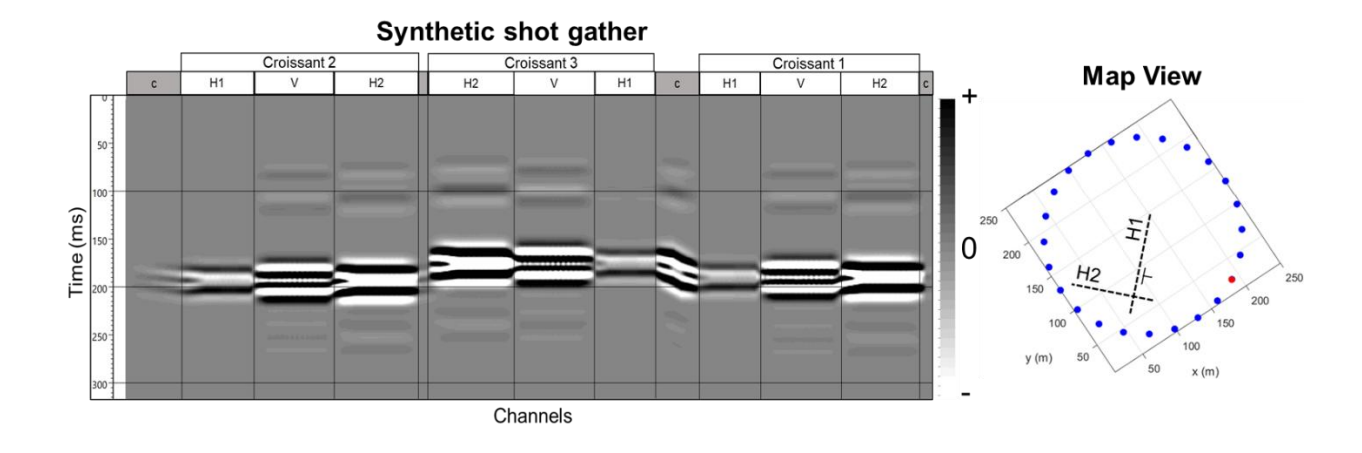


FIG 5.19. Shot gather of the Croissant obtained from the finite difference model (left). The map view (right) shows the source-receiver layout, where the trajectory of the fiber is indicated by small black "T" symbol. The orientations of the H1 and H2 components are shown with dotted lines. The red dot marks the source used to generate the shot gather inline with H2 component.

An important observation is the significantly higher amplitudes of the surface waves compared to the body waves, as well as the noticeable sensitivity to the angle of incidence—an aspect that

will be explored further in the next chapter. Specifically, Section 6.4.1 will present a quantitative analysis of the amplitude behavior of each Croissant across twenty shots. The goal is to gain a broader understanding of the expected amplitude patterns in an idealized modeling scenario.

5.5.2 2nd Simulation: homogeneous layered model - CMC Velocity Model (cross-correlated wavelet)

The first 60 meters of the velocity model provided by CMC were shown in Figure 5.9; however, a depth of 100 meters was used as input for this experiment sampled every 0.5 m. The modified cross-correlated wavelet was used, with the processing explained in section 5.5 (low-pass filtered of 60 Hz, cropped and resampled). As shown in Figure 5.16c, the peak of this wavelet occurs at 0.4 s (400 ms), meaning that any signal appearing before this time in the shot gather corresponds to the wavelet's tail. Therefore, the reflections of interest begin at 400 ms, which is why the shot gathers presented in the following figures start from that time.

Figure 5.20 shows the shot gather generated by ElasWave3D for shot 4, which corresponds to the farthest shot in the field. To enhance the visualization of the data, an automatic gain control (AGC) with a 250 ms window was applied to bring up weaker signals in the first arrivals. Once again, high amplitudes can be observed in the vertical component for the first arrivals, occurring around 510 ms. This observation indicates strong consistency with the experimental data, as well as with the initial observations and hypotheses previously stated.

The reason for applying AGC becomes clear when examining Figure 5.21, which displays the average amplitude of raw traces for the H1, V, and H2 components over a larger time window. Understanding the amplitude relationships between different events helps guide the application of appropriate processing tools and supports more accurate data interpretation. As previously discussed in Section 5.5.1, surface waves are expected to exhibit higher amplitudes than body waves under this model. The first breaks are relatively weak and occur between the 500 and 600 ms (traces in Figure 5.21).

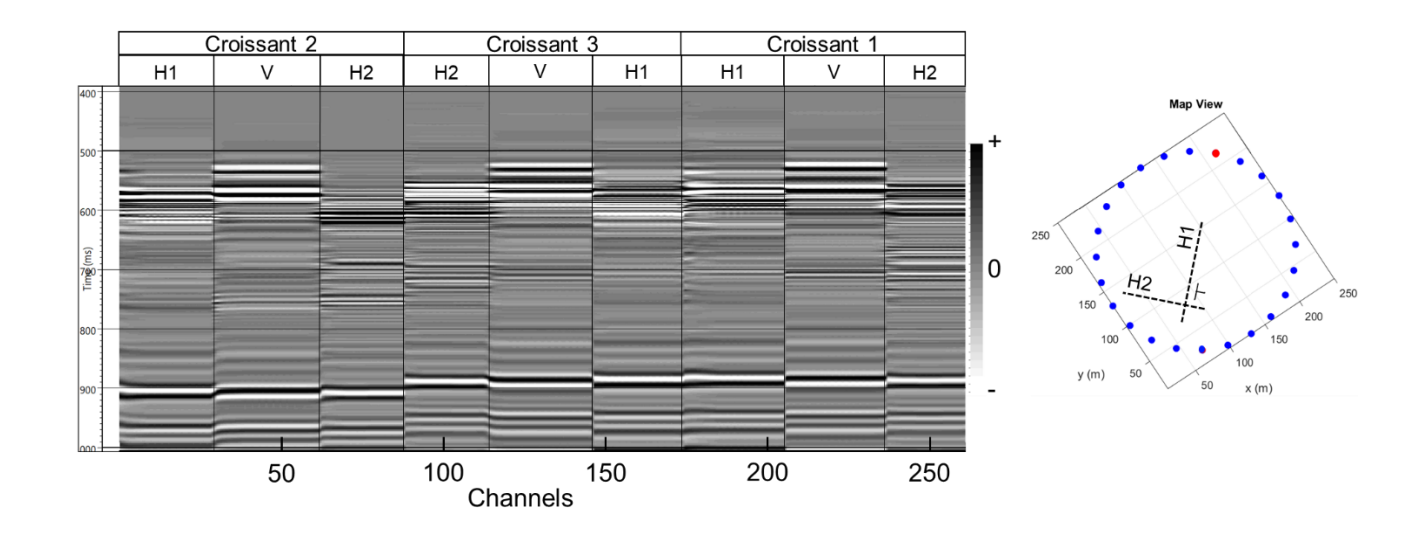


FIG 5.20. Shot gather source 4, farthest source, inline with H1 component (250 ms AGC applied)

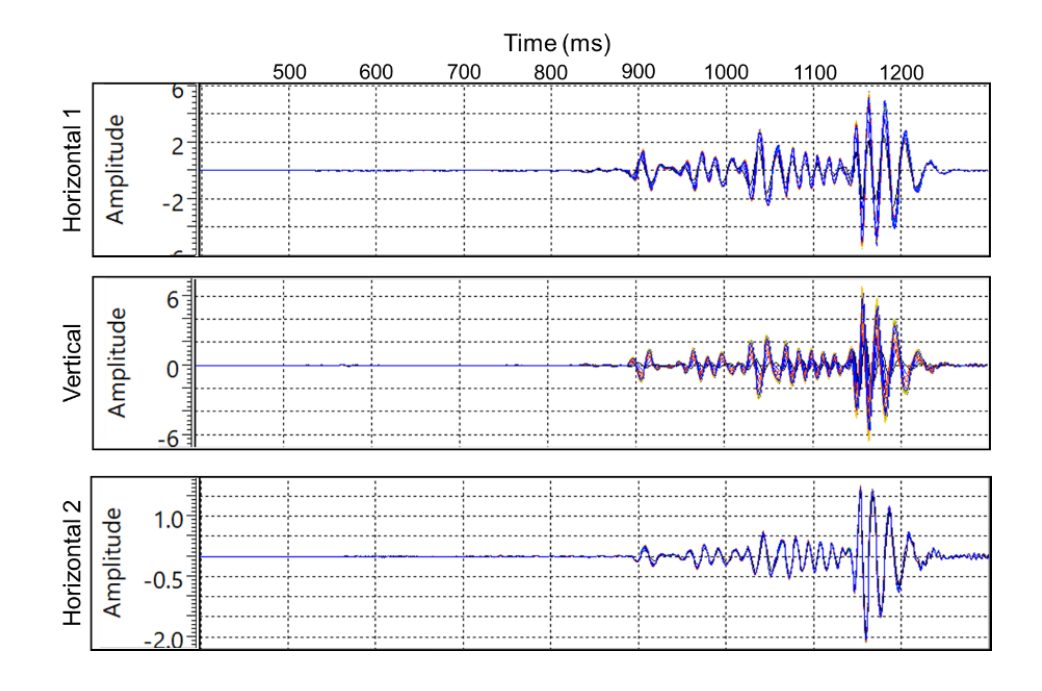


FIG 5.21. In blue, average trace amplitudes for the three components, H1, V, and H2 for shot 4 of Croissant 2.

Figures 5.22 and 5.23 show shot gathers for two sources: Figure 5.22 corresponds to a source aligned with the H1 component (inline), while Figure 5.23 corresponds to a source aligned with the H2 component. An interesting observation in Figure 5.22 is that, under the same AGC settings for both shots, the first-break amplitudes recorded by Croissant 2 are noticeably lower than those recorded by Croissants 1 and 3, even though the surface wave amplitudes remain high across all three. The primary spatial difference is that Croissant 2 is located closer to source 15

than the other two (see offset differences in Table 5.2). Additionally, the horizontal components show higher amplitudes than the vertical component.

Table 5.2. Differences in offset for Croissants 1, 2 and 3 respect to shot 15.

Offset – Croissant 1	Offset – Croissant 2	Offset – Croissant 3
72.09 m	63.18 m	71.45 m

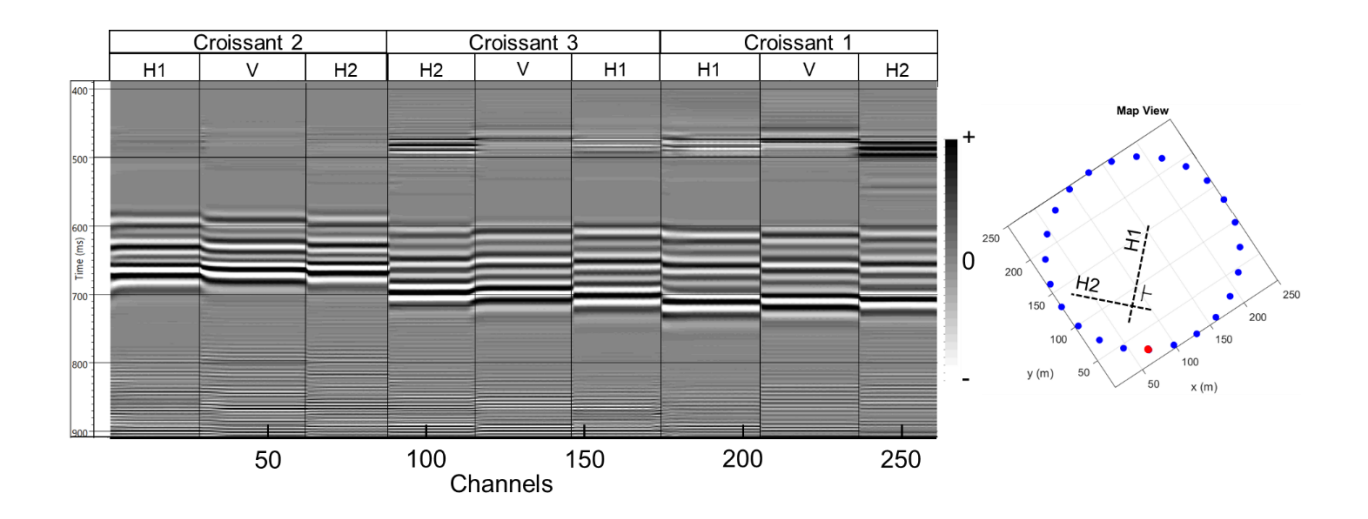


FIG 5.22. Shot gather source 15, nearest source, inline with H1 component (250 ms AGC applied)

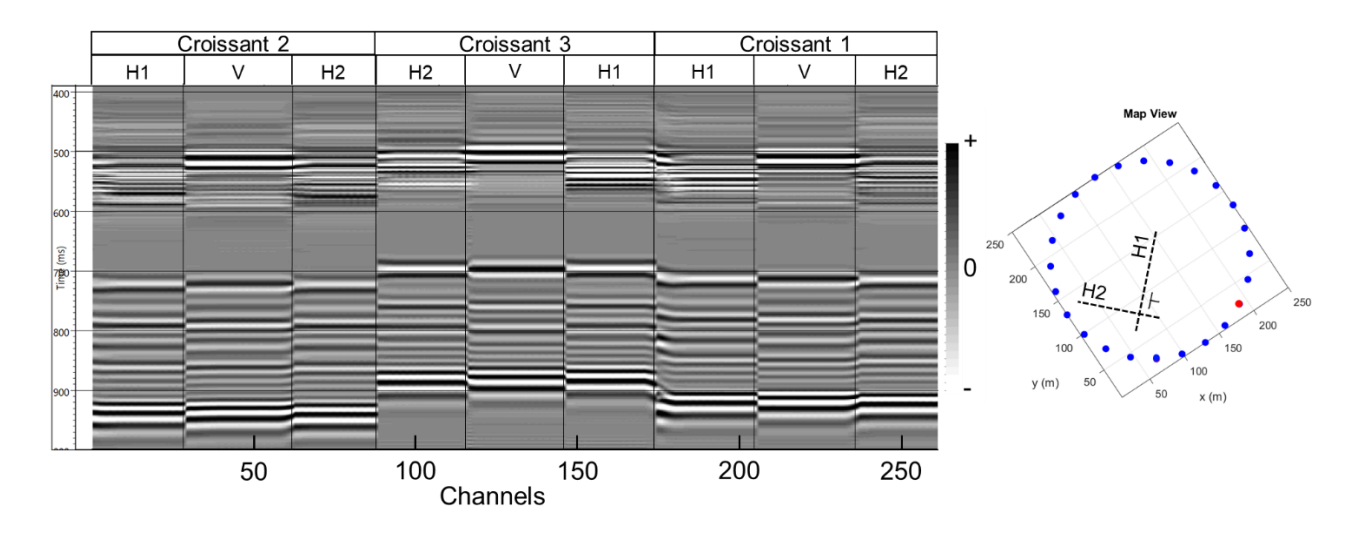


FIG 5.23. Shot gather source 10, inline with H2 component (250 ms AGC applied)

Figure 5.23, on the other hand, shows the shot gather from shot 10 (offset of ~115 m), aligned with the H2 components. Once again, high amplitudes are observed in the vertical components; however, it is qualitatively difficult to discern the relative amplitude behavior between the H1 and H2 components.

Understanding the differences in Croissant offsets and the corresponding responses in the horizontal components—particularly for the closest shot (Shot 15, Figure 5.22)—compared with those from a higher-offset shot (Shot 10, Figure 5.23), where vertical component amplitudes increase noticeably, suggests that critical distance and cross-over distance are likely playing significant roles in the observed arrivals in the Croissant model data. The lower vertical amplitudes in Shot 15, in contrast with the higher vertical amplitudes in Shot 10, indicate that wave mode conversions and arrival types (e.g., direct vs. refracted waves) may be influencing the recorded signals depending on the source-receiver offset.

The good news is that, as mentioned at the beginning of this section, one of the outputs of the ElasWave3D software is a particle velocity shot gather recorded by geophones (Figure 5.24a), which allows for a more detailed analysis of seismic events. In Figure 5.24, I present the shot gather for Shot 15, recorded by geophones arranged along a straight line that intersects both the Croissant location and the source. The position of the Croissant is also indicated, providing spatial context for the seismic events captured at that location and along the receiver line (Figure 5.24b).

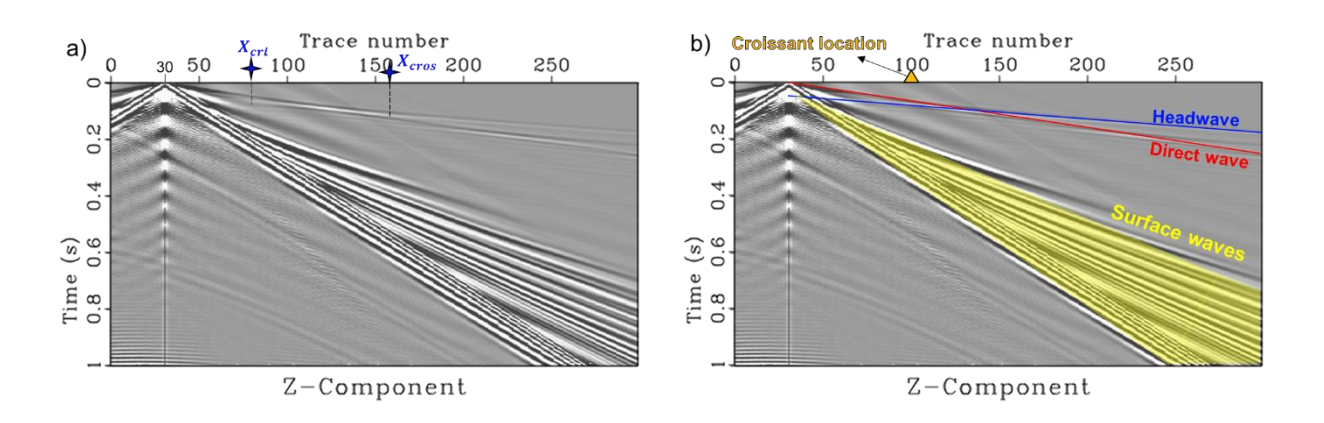


FIG 5.24.Particle velocity shot gather from line of geophones passing through the source and Croissant location.

Based on seismic refraction theory for a two-layer model with a horizontal interface, it is possible to estimate several key parameters from Figure 5.24, such as the velocities of the first and

second layers, the critical angle of refraction, the critical and crossover distance, and the depth to the refractor. These values help verify, within the context of this velocity model, the offset at which the refracted wave begins to arrive earlier than the direct wave.

Using the equations presented in Section 3.3, I calculated key parameters from the synthetic seismic shot gather in Figure 5.24. These results (see Table 5.3), based on the velocity model derived from inversion provided by CMC, offer an understanding of the minimum offsets at which refracted waves are expected to arrive before the direct wave.

Table 5.3. Estimated values for the synthetic shot gather from geophones for shot 15

V_1	V_2	$ heta_{crit}$	t_i	Z	X_{cri}	X_{cros}
~1170 <i>m/s</i>	~1992 <i>m/s</i>	~35.96913816°	~0.046s	~33.2 m	~48.2m	~125.5 <i>m</i>

As introduced in Section 5.3, and in agreement with these calculations, the refractor interface lies at approximately 33 meters depth—closely matching the bedrock surface at 29.5 meters, as indicated by well completion data provided by CMC and discussed in Section 4.2.

The velocities for layers 1 and 2 were estimated as the average velocities within the first 30 meters and below, respectively. The calculated critical distance X_{cri} was approximately 48 meters, which is shorter than the minimum offset in the L41 shot arrangement. The crossover distance X_{cros} was found to be about 125 meters, meaning that at least half of the shots in the L41 line exceed this offset.

This analysis may help explain the low amplitudes observed for the first arrivals at Croissant 2 in Shot 15 (Figure 5.22). Because Croissant 2 is located closer to the source (63 meters), its first arrivals are likely dominated by the direct wave, which typically exhibits lower amplitudes. In contrast, Croissants 1 and 3—located roughly 70 meters farther from the source—may be receiving a combination of direct waves (affecting the horizontal components) and

refracted head waves (contributing to the increased vertical amplitudes). This difference in wave type could account for the comparatively lower vertical amplitude observed at Croissant 2.

In the following chapter, I will explore the consistency between the modeled and experimental field data, which so far appears promising. A detailed analysis of seismic events—including trace behavior, velocity estimation, and amplitude characteristics—will provide a comprehensive understanding, both visually and quantitatively, of the expected wave phenomena and what is being detected by the Croissant.

6. CHAPTER 6: Amplitude response of the Croissant

The previous chapters have laid the groundwork for understanding the Croissant fiber layout, the underlying principles of DAS, and the fundamental seismic concepts relevant to this study, including body waves, surface waves, and refraction seismic theory. The context of the seismic acquisition has also been described, with particular attention to the design of the Croissant layout, arranged to capture more than one component of the seismic wave field through its 3D orientation.

Acquisition geometry includes a key source configuration: a circular source line (Line 41) designed to provide multiple source-receiver azimuths, and a variety of source-receiver offsets. These design choices aim to enhance the fiber's sensitivity to a broader range of wave field components.

The experimental field data enabled preliminary observations and the formulation of the study's hypothesis. This hypothesis was tested and supported through computational modeling, including both ray-based and full-wave field simulations. These models had appropriate geological context, and velocity models derived from inversion of the rich conventional dataset at this test site. Altogether this modeling effort provided deeper insights into the amplitude response characteristics of the Croissant layout.

In the upcoming sections, I am going to show and analyze quantitatively the amplitudes recorded by the Croissant. The synthetic shot gathers obtained from model data, including Croissant and geophones responses will serve as a starting point to what is expected and what the Croissant is sensing in each of its components.

6.1 Establish consistency of model and experimental data

Now that the modeled data have been generated using field-based conditions—including the velocity model, source wavelet and type of source, vertically (P-vibe source)—a side-by-side comparison with the experimental data can help identify similarities and assess how closely the model replicates real observations.

The modeled data reproduced the presence of high amplitudes in the vertical components. Figure 6.1 presents a comparative view of shot gather 4 (source 4, farthest shot) where Figure 6.1a: Experimental data and Figure 6.1b: Synthetic data generated using ElasWave3D.

To ensure consistency in processing and data comparison, an automatic gain control (AGC) with a 250 ms window was applied to both datasets.

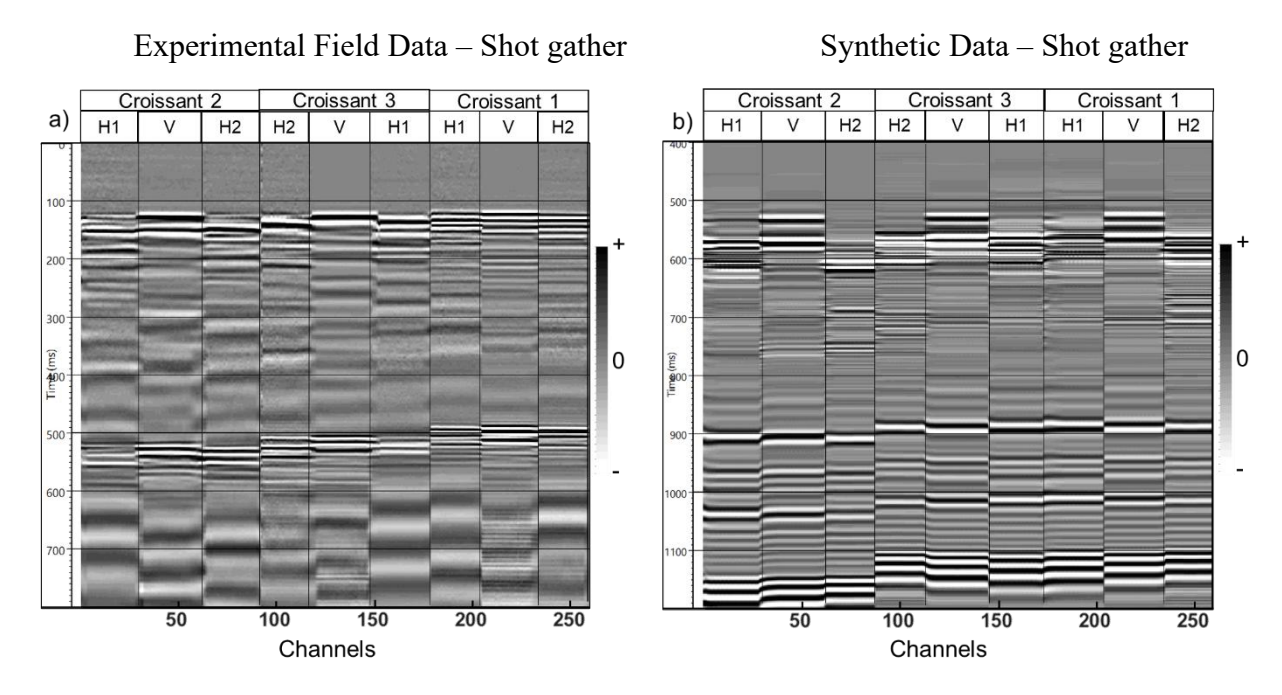


FIG 6.1. Croissant shot gathers for shot 1 from L41: a) experimental data, AGC win 250ms; b) synthetic data, AGC win 250m.

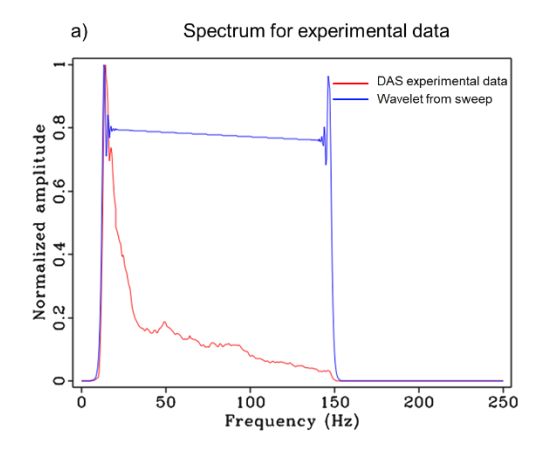
Arrival times are the first point of comparison. Visually, body-wave arrivals for vertical components appear to coincide well between the experimental and modeled data. However, for the horizontal components those first breaks may have dimmed amplitudes in the synthetic data that may not be visible and even comparable with the experimental data. Surface waves present significant timing differences, as can be observed in Croissant 2 in Figure 6.1 around 500 and 900 ms respectively.

The alignment in first arrival times for vertical components suggests that the velocity model provided by CMC offers a reliable approximation of the subsurface velocity structure.

In terms of frequency content, however, there is a clear difference. As discussed in previous chapters, the experimental data predominantly contain frequencies between 10 and 150 Hz, while

the synthetic data include frequencies up to 60 Hz due to the applied low-pass filter, and avoid numerical dispersion. Figure 6.1a (experimental data) shows first arrivals characterized by higher frequencies and surface waves dominated by lower frequencies. In contrast, Figure 6.1b (synthetic data) exhibits more prominent high-frequency content.

These qualitative frequency observations are clarified in Figure 6.2, which provides spectral comparisons:



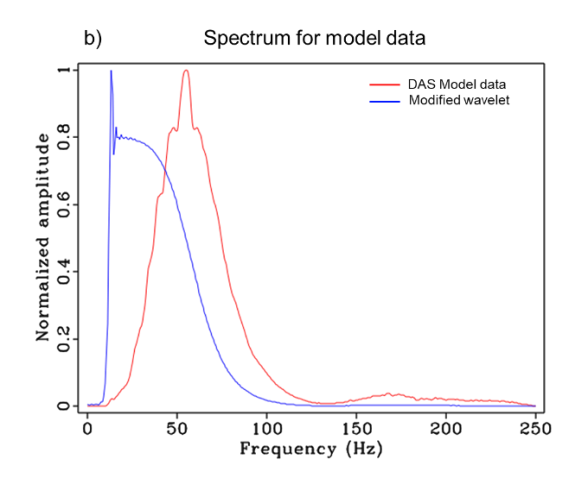


FIG 6.2. Normalized spectra for experimental and model data a) Spectrum for experimental data; in blue, wavelet extracted from cross-correlation between the source sweep with the DAS trace; in red, the spectrum for the Croissant DAS experimental data. B) Spectrum for model data; in blue, the spectrum of the modified wavelet (low-pass filter of 60 Hz); in red, the spectrum of the DAS model data.

The comparisons show that the experimental data tend to have suffered a loss of higher frequencies, likely due to natural attenuation and the Earth acting as a low-pass filter. In contrast, the modeled data retain higher frequencies which initially was unexpected.

To investigate this further, spectral analyses were performed on the modeled data. The spectra were calculated for Croissant DAS data (non-zero offset) and vertical particle velocity data (including both non-zero and zero-offset traces; see Figure 5.24), using both homogeneous half-space and homogeneous layered models. Additionally, the source type was varied between a vertical source (used in the simulations to approximate the motion of a P-vibrator) and an explosive source.

For the homogeneous medium, the Croissant data (non-zero offset) showed high-frequency content above 60 Hz when a vertical source was used. In contrast, when an explosive source was employed, the spectral content was mostly confined within the original wavelet frequency band (Figure 6.3a). A similar trend was observed in the particle velocity data: high-frequency content was preserved with the vertical source, whereas the explosive source produced a spectrum limited by the 60 Hz low-pass characteristics of the wavelet (see Figure 6.3b).

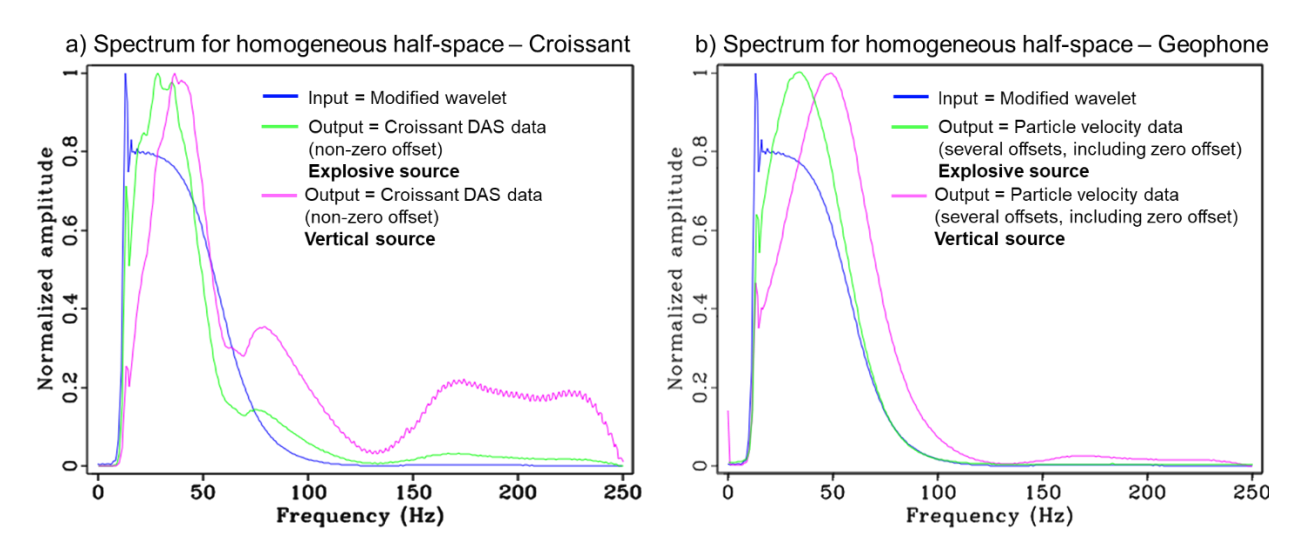


FIG 6.3. Normalized spectra for model data in homogeneous half-space; a) Spectrum for the Croissant DAS data; b) Spectrum for the Particle velocity data.

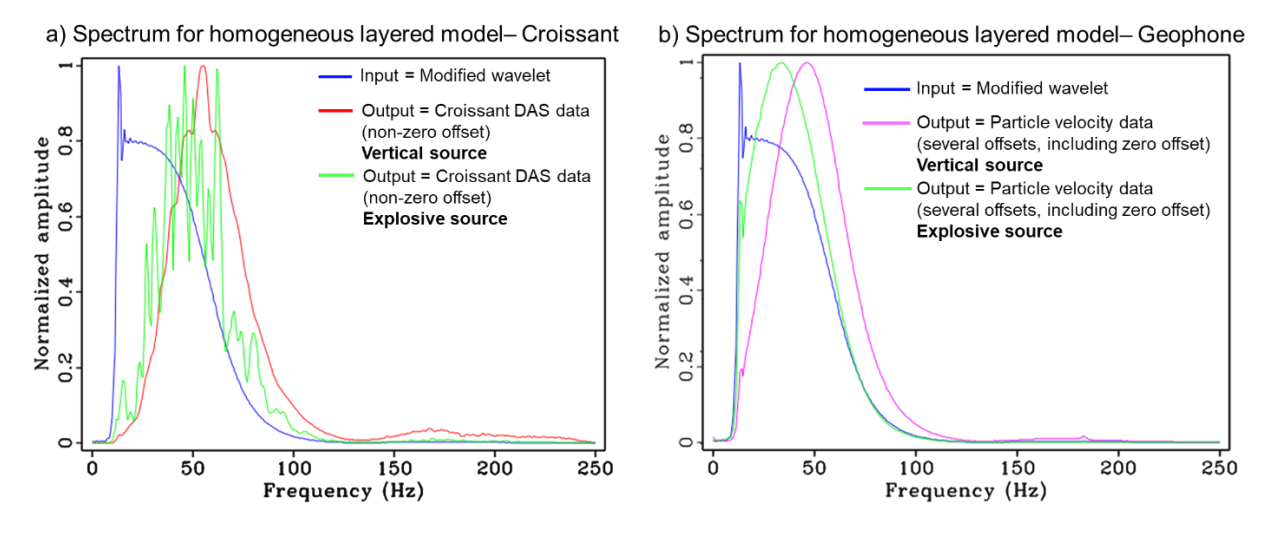


FIG 6.4. Normalized spectra for model data in homogeneous layered model; a) Spectrum for the Croissant DAS data; b) Spectrum for the particle velocity data.

This preliminary analysis highlights how source type in the ElasWave3D model influences frequency content, with the explosive source more effectively preserving the original wavelet spectrum.

For the spectra from homogeneous layered model shown in Figure 6.4, the spectrum for the Croissant data (Figure 6.4a) exhibit amplitudes extending beyond the original wavelet frequency band. Although the explosive source shifts the spectrum slightly toward lower frequencies compared to the vertical source, significant high-frequency content is still present.

In Figure 6.4b, which displays the spectrum for the particle velocity data using a vertical source, the tendency to preserve higher frequencies persists. In contrast, for the explosive source, the spectrum remains confined within the original wavelet frequency band.

To explain the frequency behavior observed in these experiments, it is important to recall that ElasWave3D simulations are based on a purely elastic, layered velocity model. In such models, the only scenario in which a recorded trace preserves the same amplitude spectrum as the input wavelet is under highly idealized conditions:

- o a homogeneous half-space (i.e., no layering or free-surface effects),
- o excitation and recording of the same motion component, and
- o the receiver positioned at the source location (i.e., zero offset).

As soon as any of these ideal conditions are not met—even in a perfectly elastic medium—the Earth acts as a linear, frequency-dependent filter (Aki and Richards, 2002).

In the case of the Croissant configuration used (2nd simulation), all three ideal conditions are not met:

- the medium is homogeneous layered,
- the model uses a vertical point source, which primarily excites P-waves, with most energy concentrated in the vertical motion component. The energy coupling into the Croissant horizontal components is reduced, causing the recorded signal to appear spectrally distorted, filtered, or diminished in specific frequency bands.

• the Croissant sensors are not located at the zero-offset position relative to the L41 sources.

In contrast, an explosive source radiates energy more isotropically, coupling more uniformly into all three receiver components. As a result, the sensors are more likely to record a wave field that closely resembles the original wavelet, regardless of direction. In a layered medium, energy from the source wavelet splits into several modes (direct rays, reflections, refractions, mode conversions, Rayleigh surface waves, and guided body waves); because each mode reaches the receiver at a different time, their superposition boosts some frequencies and cancels others, reshaping the recorded spectrum relative to the input wavelet.

These factors explain why the Croissant data tend to produce shaped spectra with more pronounced high-frequency components, particularly when using a vertical source in a homogeneous layered model.

To establish a quantitative perspective on the model and experimental data in terms of amplitude variations with azimuth and offset, the following section outlines the methodology used for automatic first-break picking as a pre-process to calculate the root mean square (RMS) amplitudes within defined time windows. This approach will facilitate the visualization and comparison of what each Croissant and component is sensing.

6.2 Automatic first break picking for amplitude analysis workflow

In Section 5.5, different simulations were performed and the analysis of traces, in the homogeneous and heterogeneous models, helped to understand the wave arrivals sensed by the Croissant and its response in the synthetic shot gathers. It was also insightful to compare the modelled and the real data in Section 6.1.

In seismic data analysis, first-break picking refers to the process of identifying the arrival time of the first detectable seismic wave at each receiver. This is a critical step in seismic data processing, as it forms the basis for velocity estimation, stacking, and time-windowing for further analysis.

In the context of this study, first-break times help defining the time windows used to analyze the amplitude response of the Croissant layout. Before delving into the interpretation of amplitude variations, first-break picking was performed automatically using a Modified Energy Ratio (MER) attribute, as proposed by (Wong, 2023).

This method performs well in high signal-to-noise ratio (SNR) conditions, producing consistent and accurate first-break estimates. However, in low SNR scenarios, the algorithm may yield random variations and outliers, causing deviations from the expected smooth time-pick trend across receivers or frequency bands (Wong 2023).

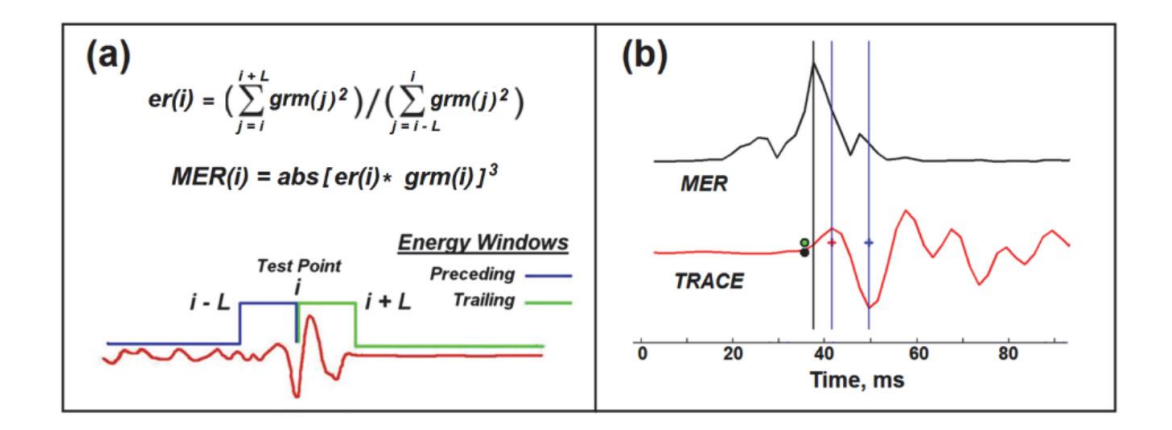


FIG 6.5. (a) Definition of the MER attribute of a seismic trace. The preceding and trailing energy collection windows have equal lengths L located at a test point i. (b) The vertical black line is the time of the peak MER value; the black and green dots indicate manually picked first-break times (extracted from Wong, 2023).

From Figure 6.5, er(i) is the energy ratio at the test point i; gmr(j) is the amplitude of the trace j; and MER(i) is the Modify Energy Ratio attribute.

The SNR2 value in decibels was taken from the output of the MER algorithm. This value is calculated by trace using the following formula:

$$SNR2(j) = 10 * log(SNR)$$
(6.1)

where SNR = er(i).

6.3 Amplitude analysis of the Croissant

To implement the Modified Energy Ratio (MER) algorithm described above, the connector segments of the fiber—traces that do not correspond to a specific component of interest—were removed from the dataset. Only the traces corresponding to the Vertical, Horizontal 1, and Horizontal 2 components of each Croissant were retained for analysis, as illustrated in Figure 6.6.

A key parameter in the MER algorithm is the window length (L as shown in Figure 6.5), denoted as winMER. Selecting an appropriate winMER value is essential for accurate first-break picking. According to Wong (2023), some practical guidelines can be followed: for noisy data, the window length should be approximately two to three times the dominant period of the seismic arrival, whereas for noise-free data, it may be a fraction of the dominant period.

Figure 6.6 presents a shot gather within a time window from 0 to 300 ms. Each component includes 21 traces, accounting just for the traces within the 1-meter frame of each component and trying to avoid connector segments. This figure illustrates the amplitude relationships among the vertical and horizontal components during the first breaks (with no AGC applied). The vertical component clearly shows strong amplitudes at the first arrivals, whereas in the horizontal components—particularly H2—these arrivals are more difficult to identify with precision.

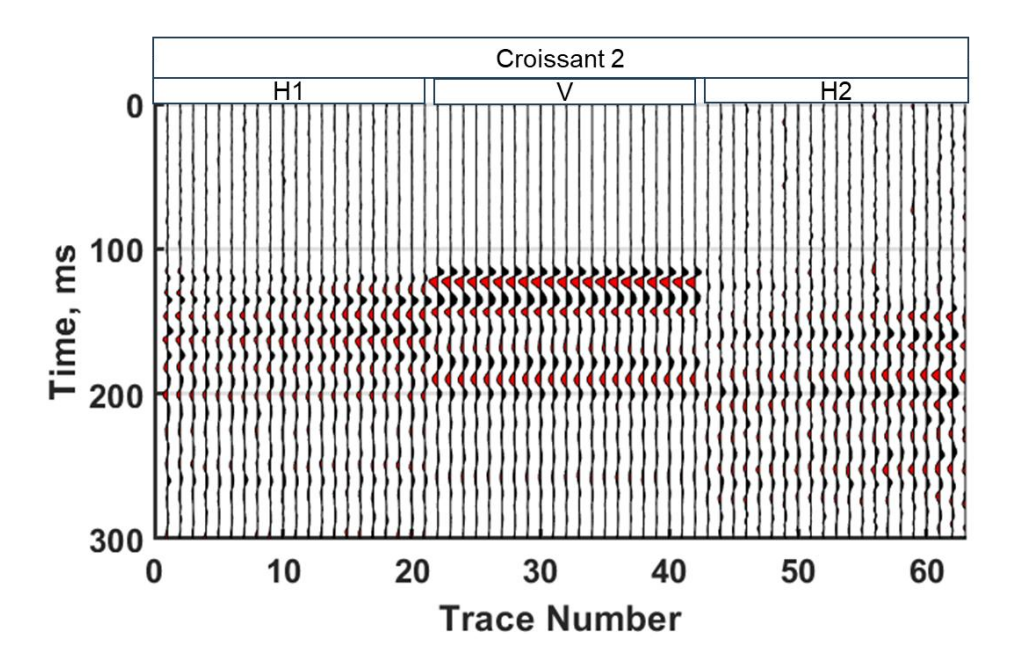


FIG 6.6. Shot gather for shot 1 (L41) for Croissant 2, with H1, V and H2 components. Traces in wiggle display are shown.

For the vertical component, one signal period corresponds to approximately 18 ms, while for H1 and H2 it is closer to 15 ms. Several winMER values were tested to evaluate how window size influences the Signal-to-Noise Ratio (SNR), in order to determine an optimal setting for automatic first-break picking.

Figure 6.7 presents the SNR results, using Equation 6.1, for three different window lengths: 10 ms, 30 ms, and 45 ms. The 10 ms window corresponds to a fraction of the dominant period, while the 30 ms and 45 ms windows correspond to approximately two and three times the dominant period, respectively—particularly relevant for the noisier H1 and H2 components. The vertical component consistently exhibits a higher SNR than the horizontal components at both 30 ms and 45 ms. At the shorter window length of 10 ms, the SNR for the vertical component decreases slightly but remains significantly higher than that of H1 and H2. A few outliers are observed, likely due to noisy traces in the data.

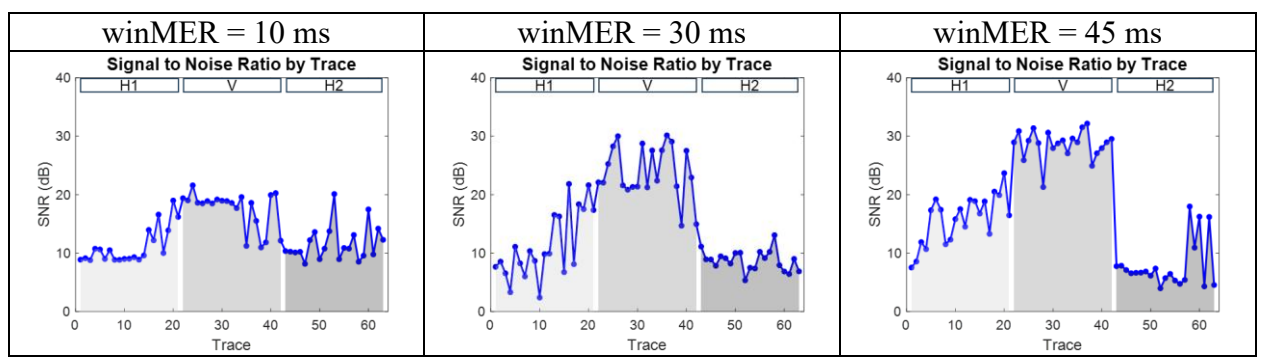


FIG 6.7 Signal to noise ratio by trace for shot 1 (L41) - Croissant 2 by components

As a baseline for the next steps, the MER algorithm was initially applied using a winMER of 10 ms. The automatically picked first breaks for Shot 1 from Line 41 (2023 – 2-sweep dataset) are shown in blue in Figure 6.8. The first break picks for the vertical components appear accurate, whereas no reliable picks are identified for the horizontal components. This result supports the observation made by Wong (2023), which states that for low-noise data, the window length can be a fraction of the dominant period. However, in the presence of higher noise levels—as seen in the horizontal components—this shorter window becomes insufficient for accurate picking.

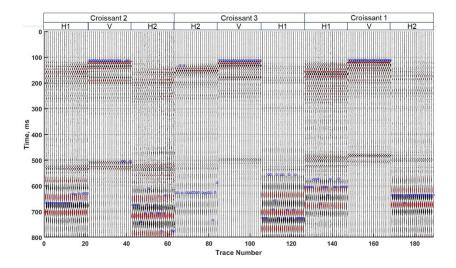


FIG 6.8. Shot gather for shot 1 (L41). Traces for Croissant 2, 3 and 1 with their respective components are visible. Blue circles are the automatic first-break picking from MER. winMer=10ms

When the winMER is increased to 45 ms, as shown in Figure 6.9, there is a noticeable improvement in the automatic first-break picks for the horizontal components. However, these

picks are still not fully reliable or consistently accurate. Conversely, the precision of the vertical component picks begins to degrade, illustrating a trade-off between window size and picking accuracy across the different components. This emphasizes the importance of optimizing winMER based on the dominant signal characteristics and noise levels specific to each component.

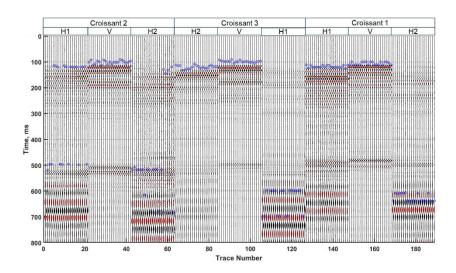


FIG 6.9. Shot gather for shot 1 (L41). Traces for Croissant 2, 3 and 1 with their respective components are visible. Blue circles are the automatic first-break picking from MER. winMer=45ms

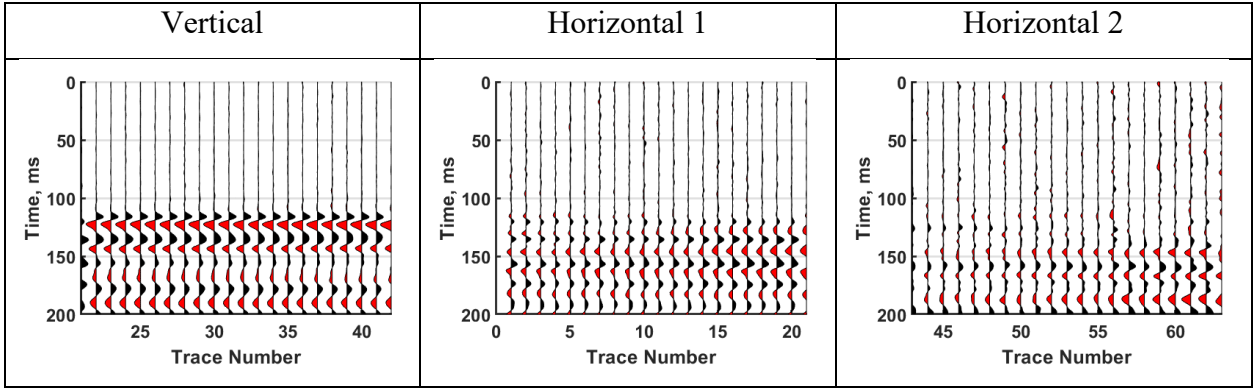


FIG 6.10 Croissant data separated in three components Vertical, Horizontal 1 and Horizontal 2. Window showed 0-200ms

To address this, and considering that the trace signatures within each component are generally consistent—with limited variation aside from the noisy traces—the following steps were carried out:

1. Stack the traces by component to enhance signal quality and suppress noise (Figure 6.10).

- 2. Apply the MER algorithm independently to each of the three stacked traces corresponding to the vertical (V), horizontal 1 (H1), and horizontal 2 (H2) components in a limited time-window from 0 150 ms, to avoid the picks in higher energy ratios such as the surface waves.
- 3. Assign the first-break time obtained from each stacked trace to all individual traces within the corresponding component.

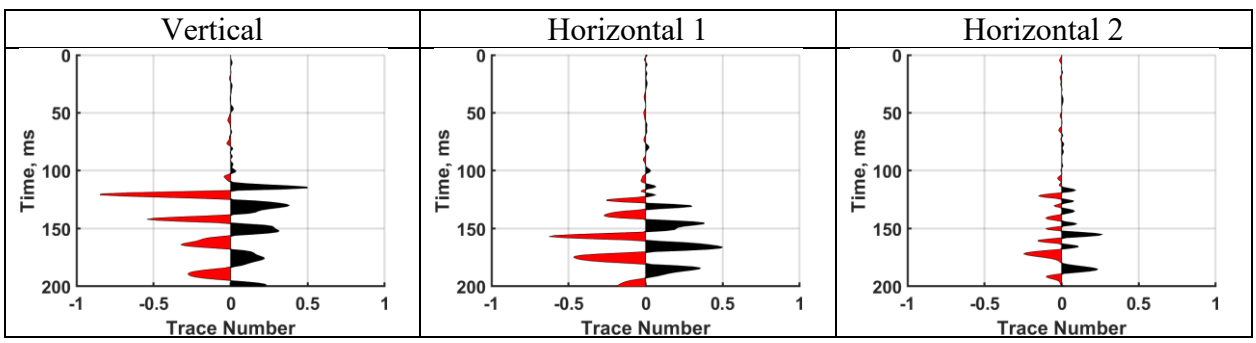


FIG 6.11 Stacked traces by components by Croissant - This Data correspond to Croissant 1 Shot 1 (L41)

However, several limitations were encountered in accurately picking first breaks on the horizontal components. These were primarily due to low amplitudes in the first arrivals and poor signal-to-noise ratios (SNR) in the surrounding time windows—challenges that persisted even after stacking the traces. As a result, accurate first-break picking was not feasible for some horizontal traces.

To address this issue, I focused exclusively on the vertical component, which consistently exhibited high SNR across all Croissants (1, 2 and 3) and twenty-four shots. Since the primary goal of this step is to calculate the RMS amplitude within a time window centered on the first arrivals for all three components, using a reliable reference time is crucial and do not need to be exactly.

The revised steps were as follows:

- 1. Stack the vertical component traces to enhance signal quality and reduce noise (see Figure 6.11).
- 2. Apply the MER algorithm to the stacked vertical (V) trace to identify the first-break time.

3. Assign the first-break time obtained from the stacked vertical trace to all corresponding individual traces, including H1 and H2.

The MER algorithm selects the time on the MER value peak which represent the first break in the trace (see Figure 6.5 (b)), giving as a result a first break picks as presents Figure 6.12. Gain was applied to visualize the first breaks for the horizontal components.

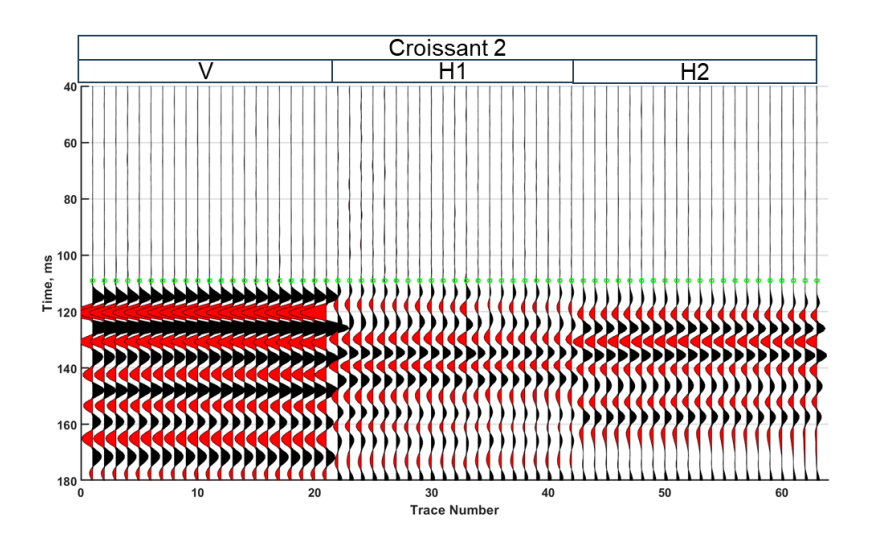


FIG 6.12. First break picking for experimental field data. In green circles after use the vertical stacked trace. Gain applied.

An important clarification regarding the first break picking in Figure 6.12 is that the approach shown is appropriate for minimum phase data. However, the Croissant dataset is zero phase due to the use of vibroseis as the source and has not undergone any phase correction. Therefore, the first break should be identified as the highest amplitude of the first peak.

Nonetheless, in the subsequent analysis steps, amplitude measurements will be calculated relative to the first break time on each trace, as illustrated in Figure 6.13.

With this result, it was possible the calculation of the RMS amplitude for the modeled data, and experimental field data in Table 4.1 and 4.2 as well as the geophone data.

6.3.1 Amplitude analysis from Finite Difference Model

Based on the previous results, it was easy to automatize the calculation of the RMS amplitudes by components and Croissants.

As noted in Section 5.5.2, the amplitude differences between body waves and surface waves—arising from different shot gathers with varying azimuths and offsets—appear promising for further analysis.

For that reason, in this section, the amplitude analysis was performed using two distinct time windows:

- 1. **First Arrival Window (FA)** focused on capturing the amplitudes of the initial P-wave (direct or head wave), as observed in the modeling results in previous sections.
- 2. **Surface Wave Window (SW)** aimed at analyzing the amplitudes associated with laterarriving surface waves, which typically exhibit different particle motion and frequency content.

The primary objective is to analyze amplitude behavior in a geological simple medium. This will provide a baseline reference for subsequent evaluations in the heterogeneous model, facilitating the interpretation of complex responses observed in real data (see Section 6.3.2).

To present the results in a clear and concise manner, RMS amplitude was computed trace by trace within each time window and for each component. For instance, the vertical component in Croissant 2 consists of 21 traces. The time window for the first arrival analysis was set to 40 ms: after the first-break time. This selection ensures that the measured energy corresponds primarily to the first arrivals (see Figure 6.13). That is why an accurate first-break picking was a critical prerequisite.

This procedure results in 21 RMS amplitude values per component (e.g., for the vertical component of Croissant 1). However, as illustrated in Figure 6.13, the amplitude variation within each component is usually consistent across traces. This allows the calculation of an average RMS amplitude per component, providing a single representative value for each component (V, H1 and H2), that can be plotted by shot, and Croissant.

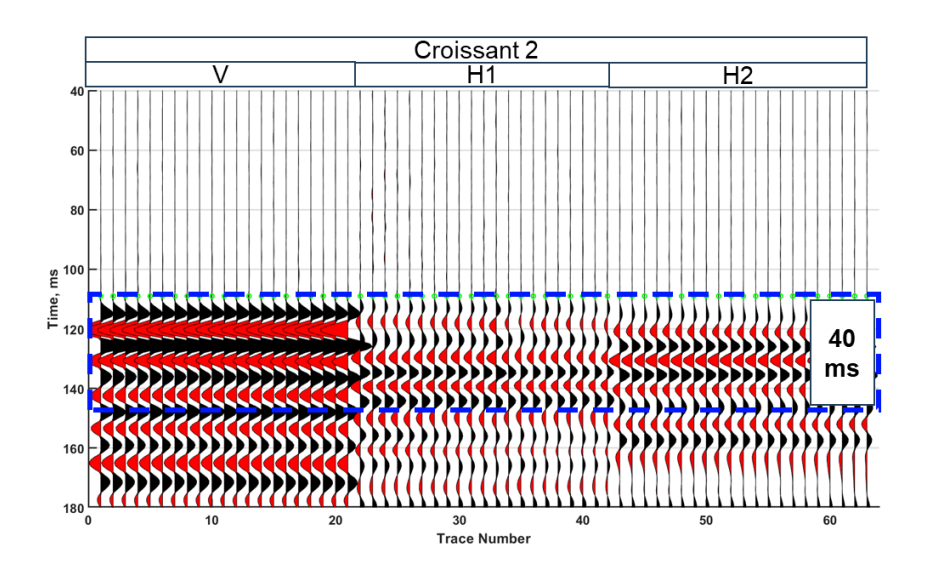


FIG 6.13. Example time window for First Arrival Analysis enclosed in the dotted blue box. In green, the first-break time; RMS window 40 ms below the FB.

The following comparisons aim to identify consistent patterns in amplitude responses across Croissants 1, 2, and 3, as well as among the Vertical, Horizontal 1 (H1), and Horizontal 2 (H2) components for all 24 shots. Each shot introduces a different angle of incidence of the seismic wavefield at the sensors, influencing the recorded amplitudes due to directional sensitivity and strain response.

Before proceeding to the next subsection, Figure 6.14 illustrates the shot positions relative to the Croissants, with color coding indicating the shots most likely to influence the horizontal components (left) as well as their offsets (right). This visual aid supports the understanding of azimuthal relationships that are important for the upcoming amplitude analysis.

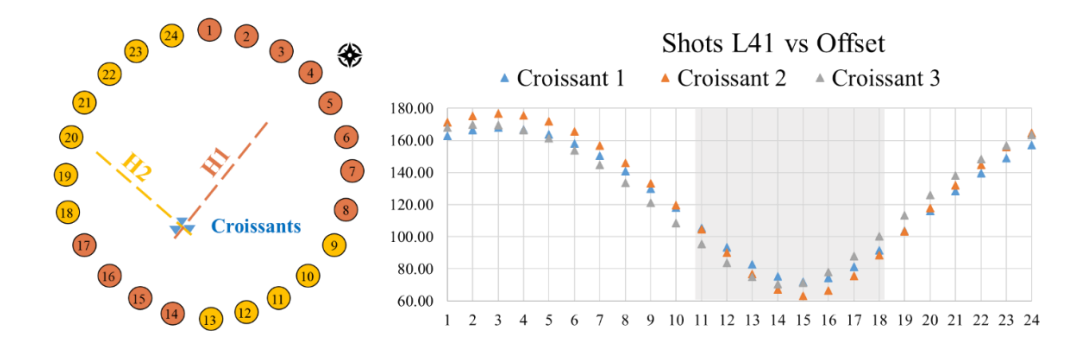


FIG 6.14. Schematic representation of the Line 41 with the twenty-four shots (left). Croissant location in blue. Horizontal 1 component color coded in orange, shots to the NE and SW aligned with the H1 component. Horizontal 2 component color coded in yellow, shots to the SE and NW aligned with the H2 component. (right) Shots vs Offset, shots highlighted in grey are near offset.

6.3.1.1 Amplitude analysis for homogeneous half-space (model data from 1st simulation)

i. First Arrival Analysis - homogeneous half-space

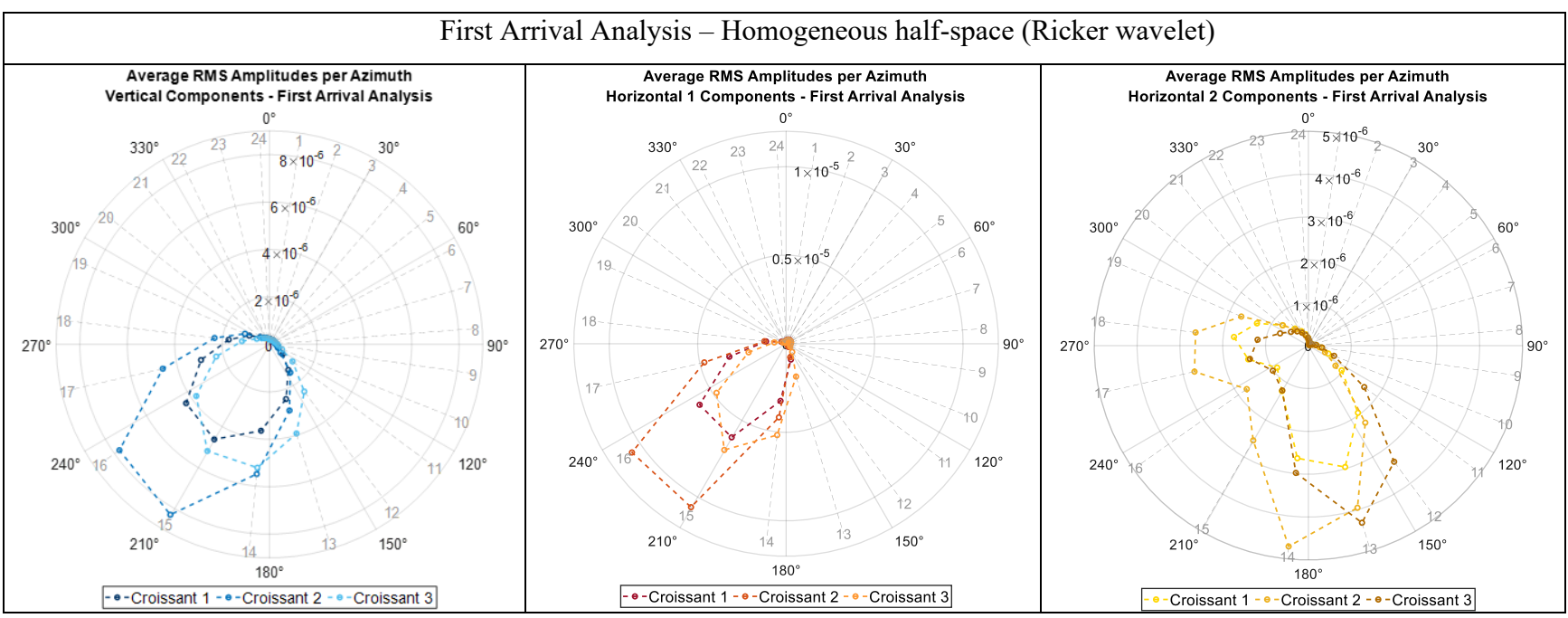


FIG 6.15 Average RMS Amplitudes per Azimuth for First Arrival Analysis for homogeneous half-space (time window 25ms). In light gray are the shot numbers (1-24). Radial axes correspond to the average RMS amplitude, and angles correspond to shot-Croissant azimuth.

The figures in Figure 6.15 show higher amplitudes for azimuths between 120° and 280°, and lower amplitudes for azimuths between 280° and 120°, measured clockwise, particularly for the Vertical (V) and Horizontal 1 (H1) components. Shots 11 through 18 correspond to near-offset sources, with offsets equal to or less than 100 m. These observations indicate that amplitudes are generally higher at near offsets and lower at far offsets across all three components, demonstrating the expected decrease in amplitude with increasing offset.

In this homogeneous half-space model, the vertical component retains higher amplitudes compared to the horizontal components. As discussed earlier, the source used in this simulation was a P-vibrator, which primarily excites P-waves and propagates particle motion in the vertical direction. This results in stronger vertical ground motion and explains the enhanced amplitude observed in the vertical component.

The high amplitudes for the H1component correspond to those near offset shots inline with the H1 component as expected and showed in Figure 6.14 (in orange to the southwest). In contrast, the H2 component tends to show higher amplitudes for shots aligned along its axis, specifically those located to the southeast (SE) and northwest (NW). Notably, a decrease in amplitude is observed for Shot 15 in the H2 component, which corresponds to an incidence angle nearly perpendicular to the H2 orientation. This behavior reflects the broadside sensitivity of the fiber.

Since the Croissant is not centrally positioned within the L41 source array, the amplitude response is asymmetric. This asymmetry is particularly evident in the H2 component, where both source-receiver offset and directional alignment significantly influence the recorded amplitudes of the first arrivals. In this case, the first arrivals are primarily associated with direct waves, making the observed variations especially relevant to understanding directional sensitivity in the Croissant configuration.

ii. Surface Wave Analysis- homogeneous half-space

For the surface wave analysis, amplitudes increase as offset decreases, consistent with a geometrical spreading response. As expected, and as shown in Figure 6.14—shots that are nearly aligned with the H1 and H2 components of the Croissant exhibit minimal effects of broadside insensitivity. A symmetric amplitude pattern is observed for sources with equal or similar offsets, while variations in offset produce correspondingly asymmetric amplitude responses. This behavior further supports the directional and offset-dependent sensitivity of the Croissant DAS sensor to surface wave energy.

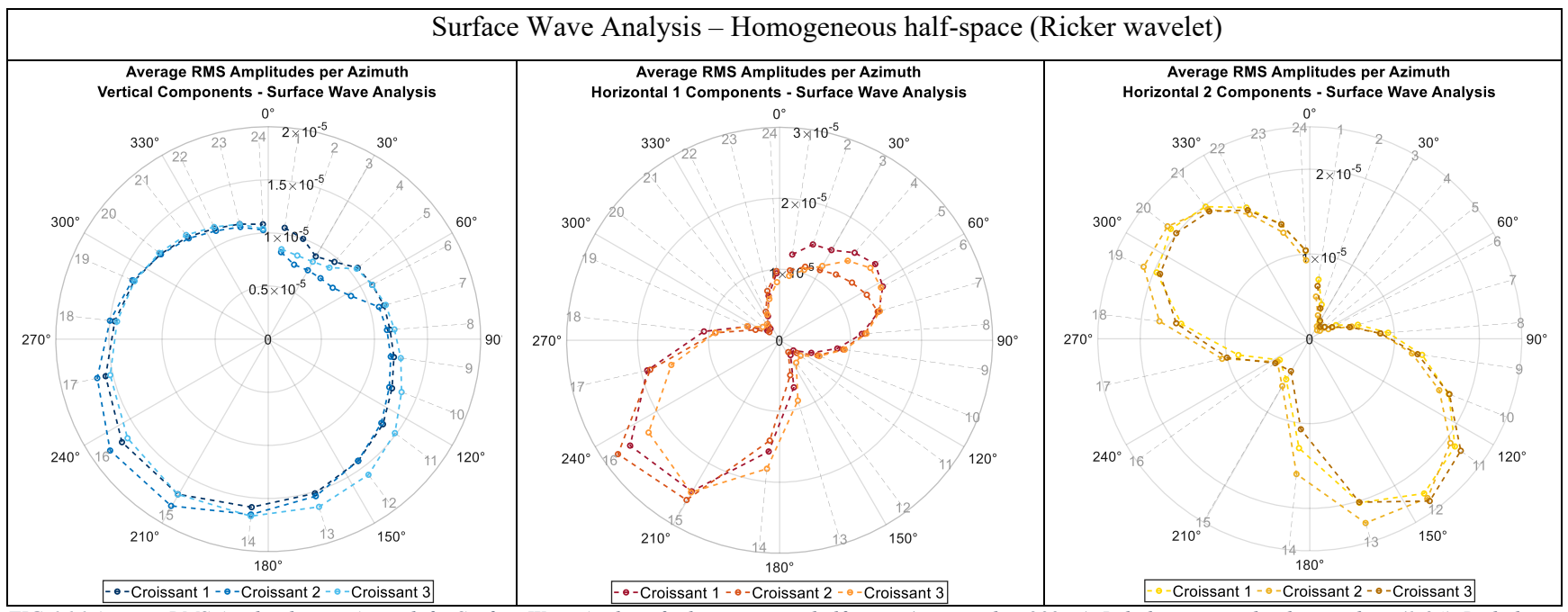


FIG 6.16 Average RMS Amplitudes per Azimuth for Surface Wave Analysis for homogeneous half-space (time window 200ms). In light gray are the shot numbers (1-24). Radial axes correspond to the average RMS amplitude, and angles correspond to azimuth shot-Croissant location.

By analyzing amplitudes of first arrivals and surface waves in a homogeneous half-space context in Figure 6.16—and observing trends with respect to angle and offset—this initial study provides a solid foundation for interpreting the results in the following section for the homogeneous layered model. While the general expectations remain consistent with those established here, insights from Section 6.1 already suggest that, in the case of first arrivals, direct and refracted waves arrive simultaneously.

iii. Geometrical Spreading for homogeneous case

Given the homogeneity of the model, geometrical spreading is expected at larger sourcereceiver offsets, resulting in amplitude attenuation due to geometrical spreading. This effect is anticipated and serves as a baseline for interpreting wave field behavior in more complex models presented later in this study.

As defined in section 3.4, in a homogeneous half-space, energy density decays proportionately to $1/r^2$, where r is the radius of the wavefront for body waves, wave amplitude is proportional the square root of energy density, it decays as 1/r (Shearer, 2019; Yilmaz, 2001). In contrast, for surface waves, the energy density decays proportionately to 1/r, which means that the amplitude decays as $1/\sqrt{r}$.

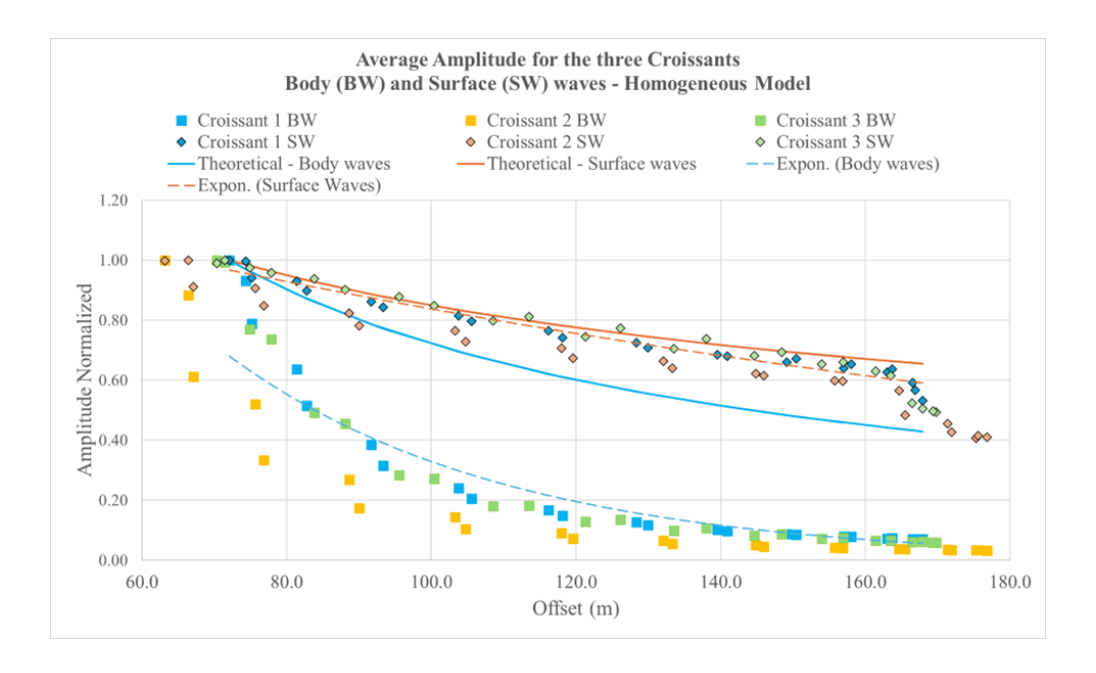


FIG 6.17. Average Amplitude for the three Croissants for Body and Surface waves for the Homogeneous model.

Figure 6.17 shows normalized amplitude versus offset for the three Croissants, with separate analyses for body waves (BW) and surface waves (SW). The theoretical amplitude decay relationships—1/r for body waves and $1/\sqrt{r}$ for surface waves—are plotted as continuous blue and orange lines, respectively. The orange trend line (for surface waves) shows strong agreement

with the observed data for surface waves, confirming the expected geometrical spreading behavior in the homogeneous case.

For the body waves, the observed amplitudes also display an exponential decay trend, consistent with theoretical expectations. However, the blue trend line appears offset by approximately -0.4 units relative to the theoretical curve. This vertical shift may indicate a scaling difference in amplitude or a normalization effect, but the overall decay trend remains consistent with the expected 1/r behavior.

6.3.1.2 Amplitude analysis for homogeneous layered model (data from 2nd simulation)

i. First Arrival Analysis - homogeneous layered model

The amplitude analysis of first arrivals in the homogeneous layered model (see Figure 6.18) yields the following key observations:

Spherical spreading is evident, as amplitudes decrease with increasing offset.

- The vertical component consistently preserves higher amplitudes compared to the horizontal components due to the source used and the presence of refraction waves.
- Azimuths between 120° and 280° introduce stronger strain responses in both the vertical (V) and horizontal 1 (H1) component.
- The horizontal 2 (H2) component shows a tendency for higher amplitudes from shots aligned along its axis, particularly from directions toward the southeast (SE) and northwest (NW).

It is important to note that, for this homogeneous layered model, direct and refracted waves may arrive simultaneously in the first-arrival window. This superposition may influence the observed amplitude behavior, especially at the cross-over point/offset.

Figure 6.18 presents the amplitude distributions for each component across all shot positions, providing further support for the trends described above.

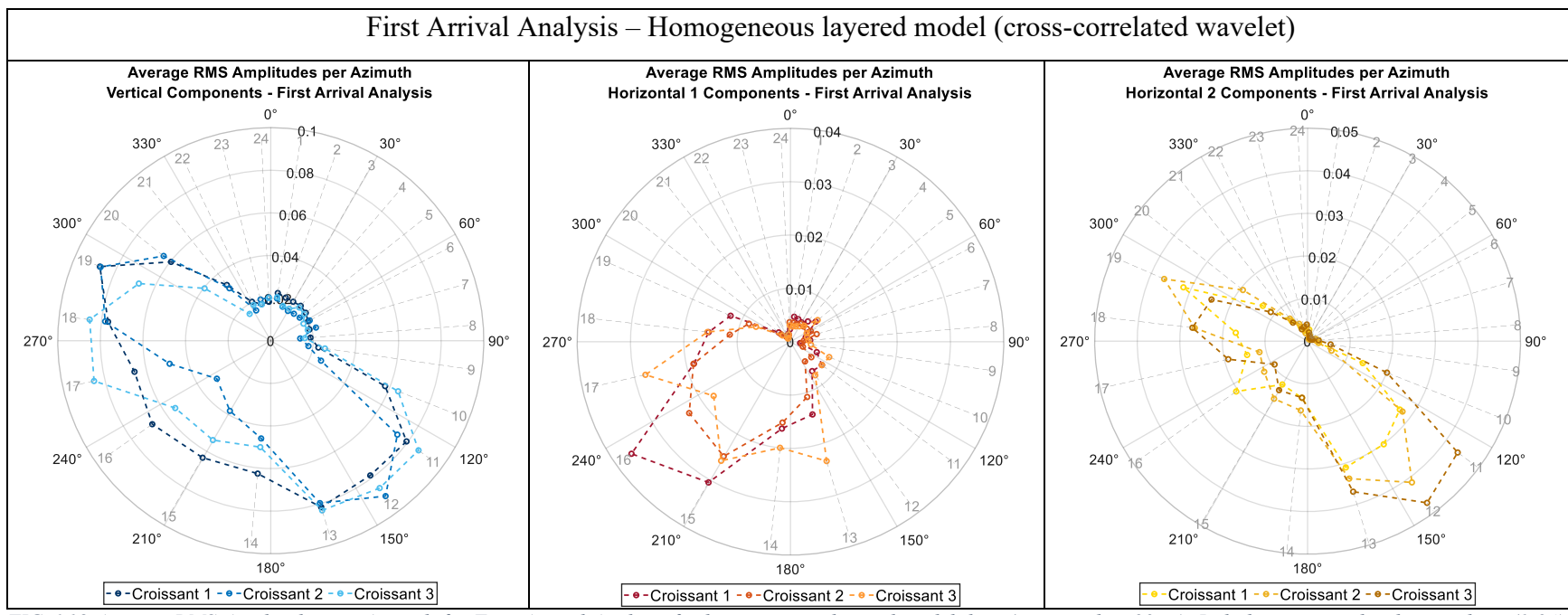


FIG 6.18 Average RMS Amplitudes per Azimuth for First Arrival Analysis for homogeneous layered model data (time window 20ms). In light gray are the shot numbers (1-24). Radial axes correspond to the average RMS amplitude, and angles correspond to azimuth shot-Croissant location.

Once again, all components exhibit low amplitudes at far offsets, reinforcing the expected geometrical spreading behavior in the homogeneous layered model. In this case, high amplitudes for the vertical component are observed over a broader azimuthal range, between approximately 110° and 310°, corresponding to source–receiver offsets of 140 m and less. Beyond this distance, amplitudes decay sharply and remain nearly constant up to offsets of 160 m.

However, it is important to note a decrease in amplitude values for shots 14, 15, 16, and even 17 in Croissants 1 and 2, which correspond to the closest source–receiver offsets. Based on previous calculations from the First Arrival Analysis of the homogeneous

half-space model, the critical distance is approximately 50 m, and the crossover distance is around 125 m. The offsets for shots 14 through 17 are all below 80 m, placing them within the range dominated by the direct wave arrival.

In contrast, the higher amplitudes observed for shots with offsets beyond 80 m suggest that, at those distances, the energy from the refracted wave becomes more dominant than that of the direct wave. This shift in wave field contribution may explain the amplitude increase at intermediate offsets and the relative drop at very short offsets.

For the H1 component, high amplitudes are concentrated in the southwest direction (as shown in Figure 6.14), where the shots are aligned with the H1 axis. A relative increase in amplitude is also observed for shots in the northeast direction, although the absolute amplitudes remain low.

The H2 component displays the expected directional sensitivity: high amplitudes are recorded for shots aligned along the H2 axis (i.e., in the SE–NW direction), and lower amplitudes are observed for shots oriented perpendicular to this component.

These results are consistent with previous observations made in the homogeneous half-space model and further support the interpretation involving the increasing influence of refracted waves with offset.

ii. Surface Wave Analysis - homogeneous layered model

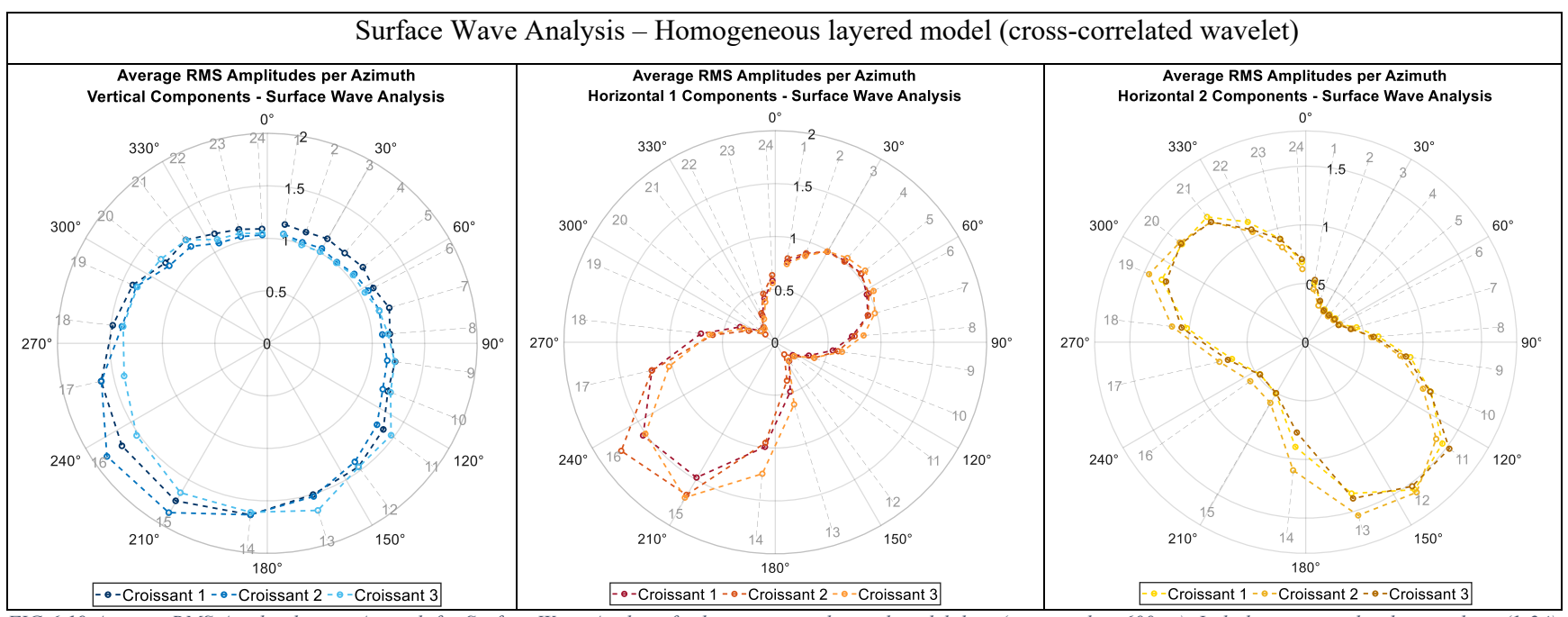


FIG 6.19 Average RMS Amplitudes per Azimuth for Surface Wave Analysis for homogeneous layered model data (time window 600ms). In light gray are the shot numbers (1-24). Radial axes correspond to the average RMS amplitude, and angles correspond to azimuth shot-Croissant location.

For the surface wave analysis in the homogeneous layered model, amplitudes increase as offset decreases—consistent with the behavior observed in the homogeneous half-space model. The H1 and H2 components exhibit clear symmetry in amplitude response for shots aligned along their respective axes and similar offsets, and an asymmetric response for shots with different offsets. This pattern reflects the directional sensitivity of the fiber orientation and is consistent with the fiber response.

The amplitude analysis conducted using two synthetic models—the homogeneous half-space and the homogeneous layered model—establishes a baseline for interpreting the experimental data. The key takeaways from Section 6.3.1 regarding amplitude behavior, which are expected to be observed in the field, are as follows:

- 1. Spherical spreading is expected for both first arrivals and surface waves arrivals.
- 2. The presence of a second, higher-velocity layer (representing the bedrock surface at ~30 meters) will give rise to head waves in the experimental data.
- 3. The vertical component is expected to preserve higher amplitudes for the first arrivals compared to the horizontal components, especially in response to the refracted wave arrivals.
- 4. For the vertical component, a decrease in amplitude is expected at near source–receiver offsets (i.e., before the critical and crossover distances). This reduction may be attributed to the dominance of the direct wave in that range.
- 5. Directionality is expected in the horizontal components, particularly for surface waves. While some directionality may also be present for first arrivals, it will be less prominent. This is because, for most shot locations producing head waves, the incidence angle to the horizontal components will be approximately vertical, reducing their sensitivity to those arrivals.

6.3.2 Amplitude analysis from Experimental data

The motivation for analyzing amplitudes in the Croissant start from the desire to understand how sensitivity varies across components (V, H1, and H2) as a function of source-receiver azimuth and offset. This analysis provides insight into the directional response of the Croissant and the relative behavior of each component.

The amplitude analysis was performed as presented in the previous section within two distinct time windows: First Arrival Window (FA) and Surface Wave window (SW).

i. First Arrivals Analysis – Croissant experimental data

An important observation was made during the March 2025 field campaign: Croissant 1 was not fully buried underground, with part of its frame and vertical-component cabling visibly exposed. This installation issue likely contributed to the persistent high-frequency content observed in the amplitude spectra of Croissant 1 across all three acquisition years—particularly in the vertical component, as shown in Figure 6.20.

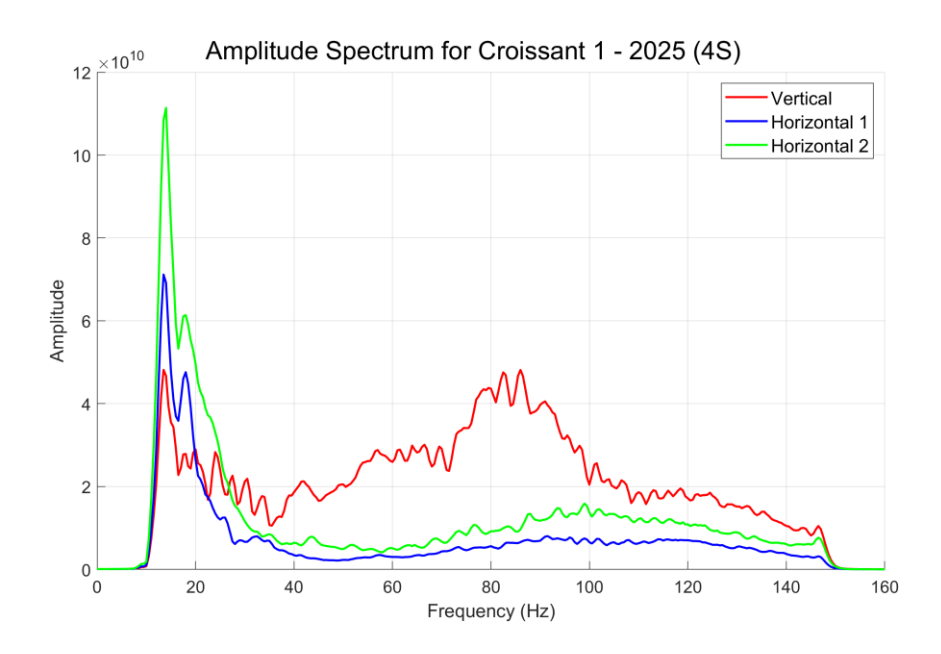


FIG 6.20. Amplitude Spectra for Croissant 1, from data acquisition of 2025, 4 sweeps.

Figures 6.21, 6.22, and 6.23 present the average RMS amplitudes for the First Arrivals Analysis of the Vertical, Horizontal 1, and Horizontal 2 components, respectively, across the 2023, 2024, and 2025 data acquisitions.

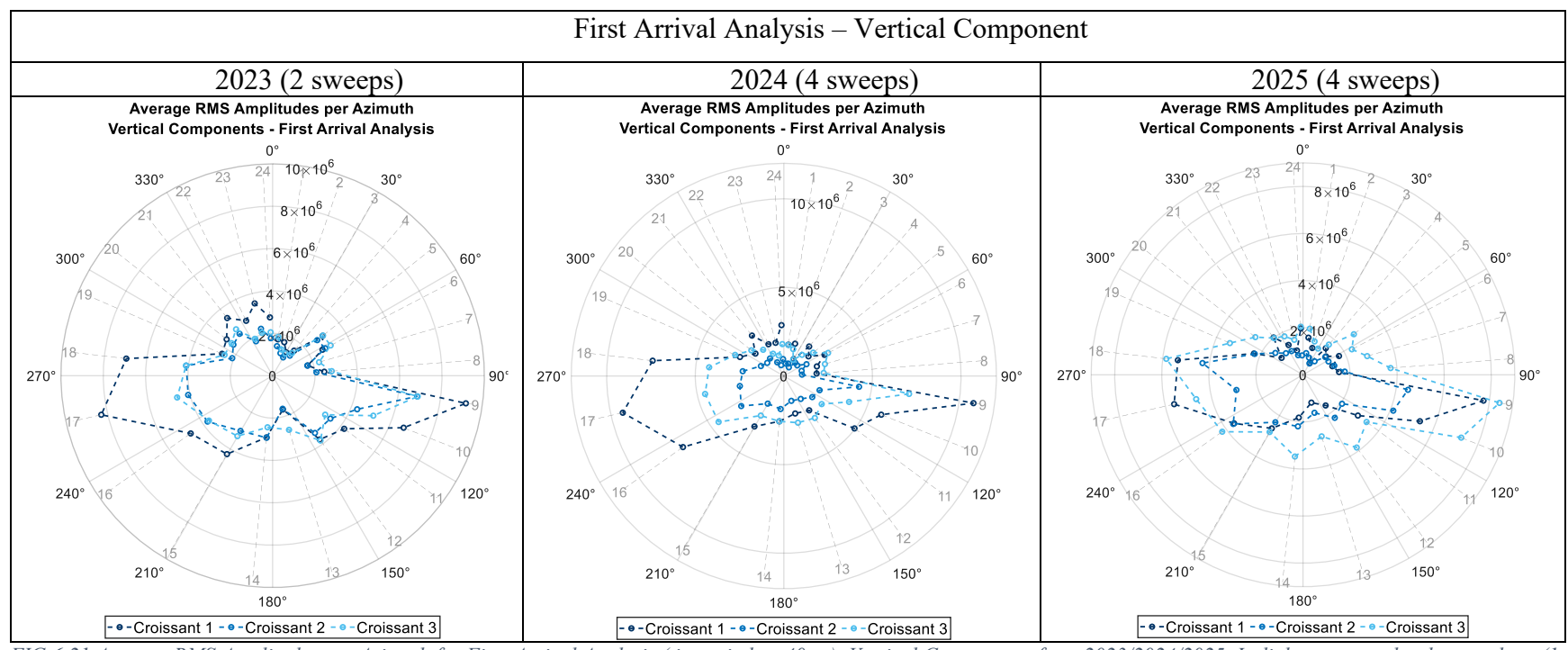


FIG 6.21 Average RMS Amplitudes per Azimuth for First Arrival Analysis (time window 40ms). Vertical Components from 2023/2024/2025. In light gray are the shot numbers (1-24). Radial axes correspond to the average RMS amplitude.

Vertical component amplitudes tend to be lower for azimuths from 290° through 85° counting clockwise, corresponding to shots 19 through 8 and for an azimuth range of 125° to 210° corresponding to shots 11 to 15. Shots 9, 10, 16, 17 and 18 consistently exhibits high values across the three Croissants throughout the 2023, 2024, and 2025 acquisitions.

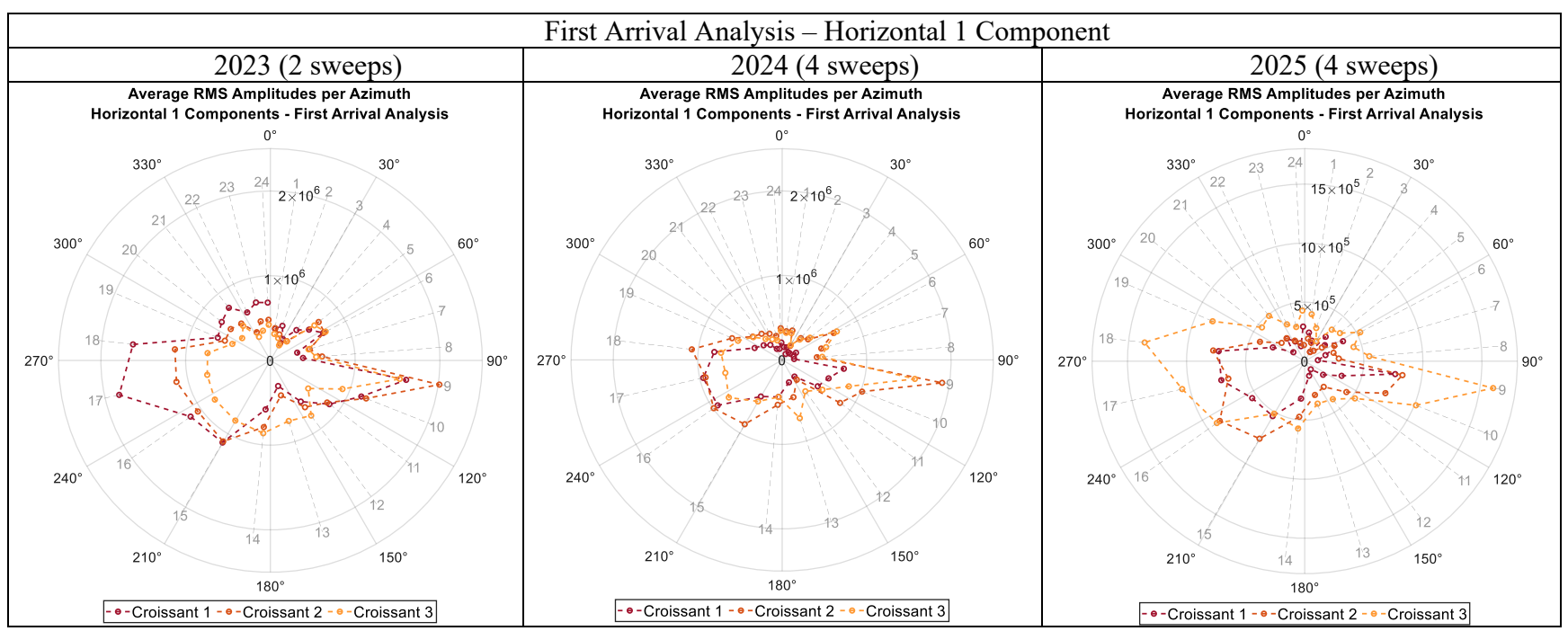


FIG 6.22 Average RMS Amplitudes per Azimuth for First Arrival Analysis (time window 40ms). Horizontal 1 Components from 2023/2024/2025. In light gray are the shot numbers (1-24). Radial axes correspond to the average RMS amplitude.

For the H1 component, Figure 6.22 reveals a similar pattern to that observed in the vertical component: Shots 9, and 18 consistently produce the highest amplitudes across all Croissants. In general, lower amplitudes are associated with azimuths ranging from 290° to 85°, corresponding to Shots 19 through 8. Similarly, reduced amplitudes are also observed for azimuths between 125° and 185°, particularly for Shots 11 through 14. In contrast, increased amplitudes are observed for Shots 15 through 18, which cover azimuths from approximately 185° to 285°, counting clockwise.

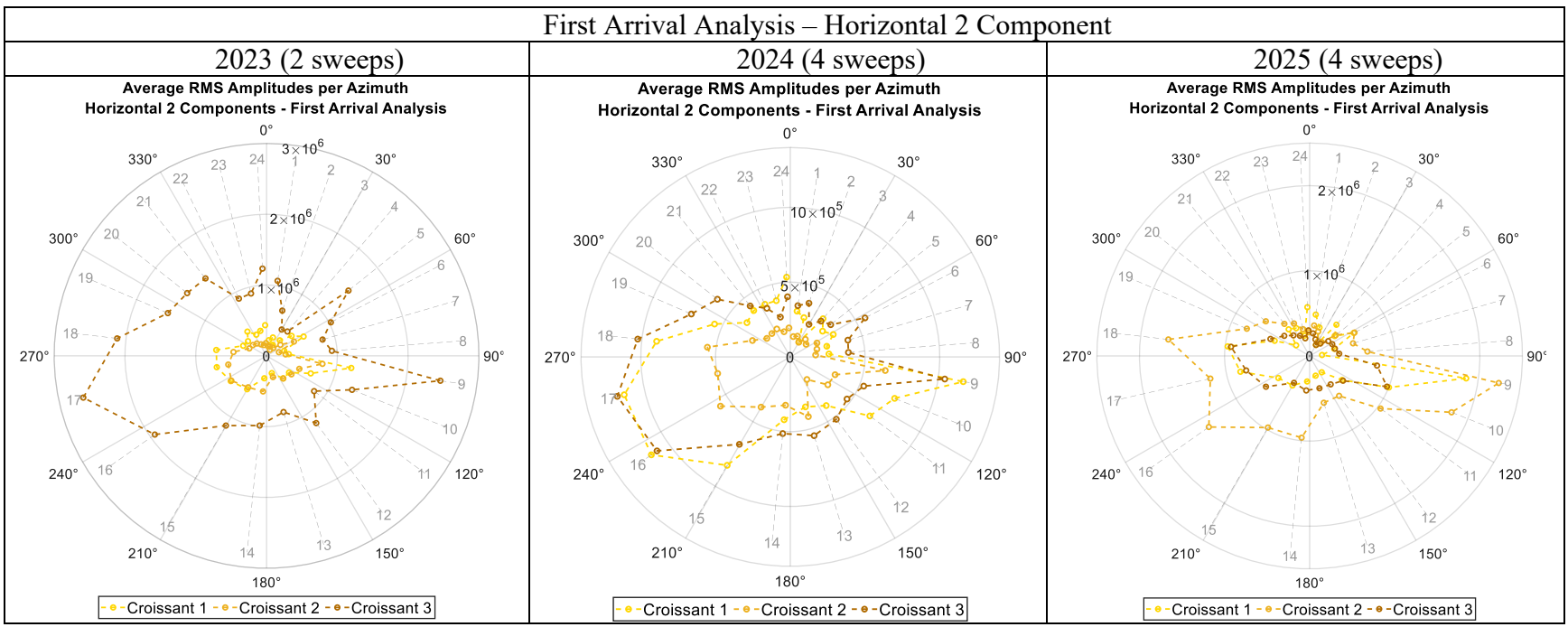


FIG 6.23 Average RMS Amplitudes per Azimuth for First Arrival Analysis (time window 40ms). Horizontal 2 Components from 2023/2024/2025. In light gray are the shot numbers (1-24). Radial axes correspond to the average RMS amplitude.

In terms of amplitudes for the H2 component, Figure 6.23 shows a consistent pattern of high amplitudes for Shots 9, 16, 17, and 18 across all three Croissants, similar to the Vertical and H1 components. Low amplitudes across azimuths ranging from 310° through 85° corresponding to shots 22 through 8, as well as for azimuths ranging from 125° through 185° corresponding to shots from 11 to 14.

Overall, shots 9, 10, 17 and 18 consistently exhibits high values across all three components (V, H1, and H2) and all three Croissants in the 2023, 2024, and 2025 acquisitions. This persistent trend suggests that there may be location-specific factors—such as

surface conditions or anisotropy—that consistently generate stronger energy due to their spatial relationship with the array or site characteristics.

Amplitude difference between vertical and horizontal components is noticeable. Range of RMS amplitudes for vertical components are higher than $2x10^6$ up to $10x10^6$, whereas the horizontal components remain below $2x10^6$; emphasizing the stronger vertical motion response.

Low amplitudes for far source-receiver offsets azimuth ranges 300° through 85° are expected for the first arrivals and a considerable increase for closer offsets, showing a geometric spreading behavior.

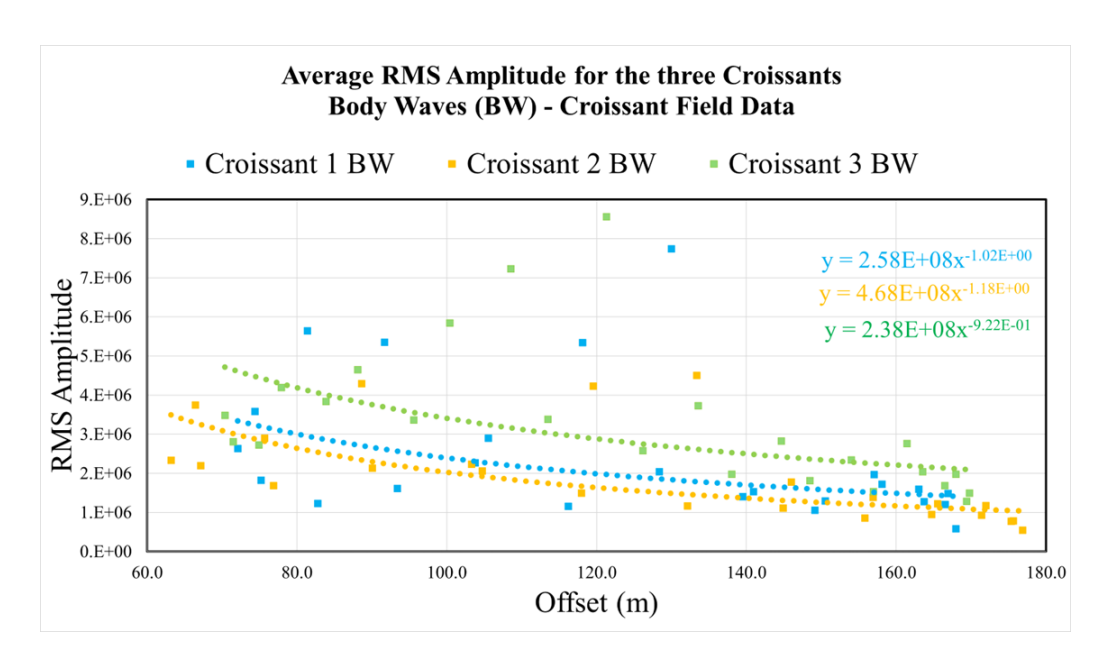


FIG 6.24. Average RMS amplitude vs Offset for the three Croissants for body waves (first arrival characterized by P-wave) from the Croissant experimental data.

To remove the offset-related influence from the Average RMS Amplitude per Azimuth plots, a geometric correction is applied to the First Arrival Analysis. Figure 6.24 illustrates the trend power functions that describe RMS amplitude decay for first arrivals (body waves, specifically P-waves) as a function of offset. The functions shown in blue, yellow, and green represent the geometric correction factors for Croissant 1, Croissant 2, and Croissant 3, respectively. In each function, x denotes the source-receiver offset, meaning that each Croissant has its own set of offset values.

The corrected average RMS amplitude is calculated as follows:

Additionally, Figure 6.25 presents a LiDAR-derived elevation map of the study area, with Croissant locations marked in red and vibration point (VP) locations in black. A key observation from the field acquisitions in November 2023 and March 2025 is that low-elevation areas were damp and wet due to melting snow. These site conditions may have influenced the recorded seismic data by affecting amplitude levels, coupling efficiency, and wavefield propagation.

The low-elevation areas during the vibroseis operations—visible in Figure 6.25—correspond to shots 9, 10, 17, 18, 21, 23, and 24. Notably, the consistently high amplitudes observed for shots 9, 10, 17, and 18 may be attributed to these wet conditions. As a result, these four shots will be removed as outliers to better observe the overall amplitude trends for each component in the 2025 dataset.

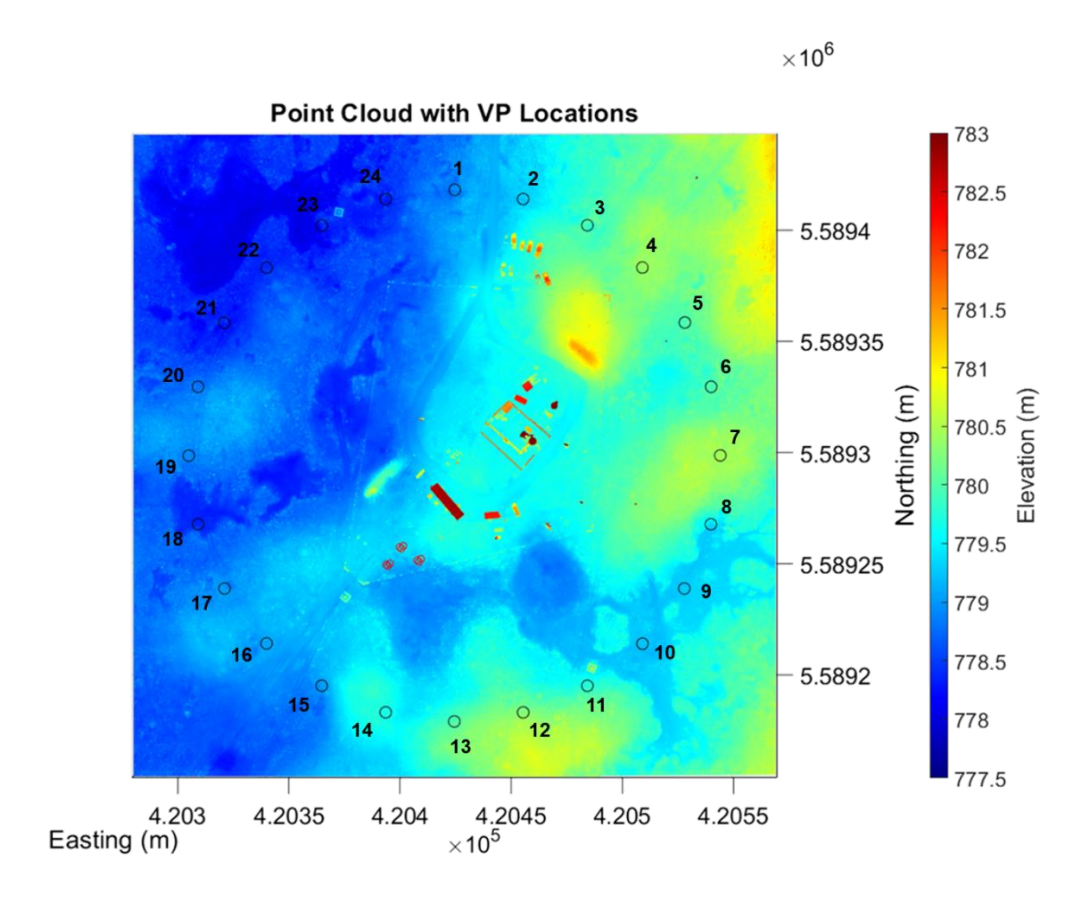


FIG 6.25. LiDAR image, elevation map, provided by CMC. VP Locations are the black circles enumerated from 1 to 24. Croissant locations in red.

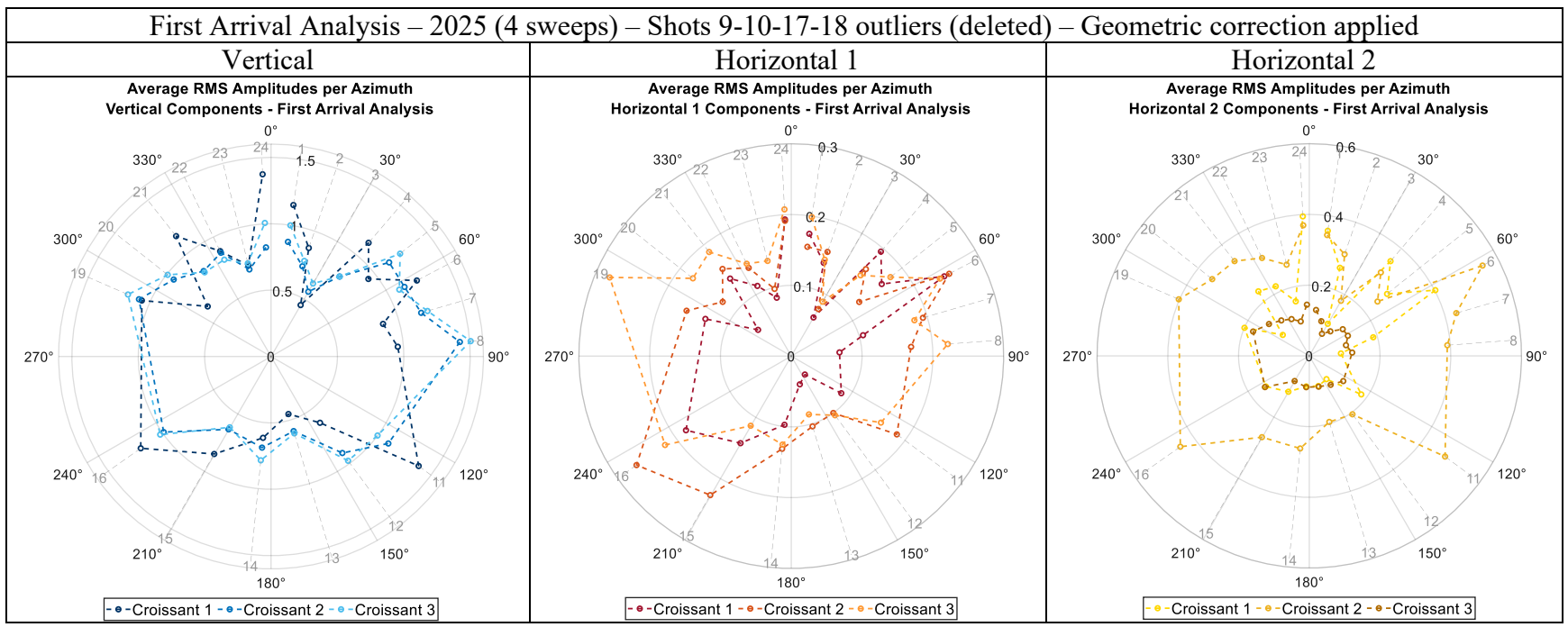


FIG 6.26. Average RMS Amplitudes per Azimuth for First Arrival Analysis (time window 40ms). Vertical, Horizontal 1 and Horizontal 2 components from 2025 dataset. In light gray are the shot numbers (1-24). Radial axes correspond to the average RMS amplitude corrected by the geometric factor by Croissant.

Figure 6.26 provides a clearer visualization of the amplitude behavior by component. The vertical components display a more symmetric amplitude distribution across the twenty-four sources. For the H1 component, an increase in amplitude is observed for shots aligned along the inline direction, resulting in improved symmetry. These include shots 14, 15, and 16, as well as shots 24, 1, 4, 5, and 6. In contrast, the H2 component does not exhibit a similar amplitude increase for the shots aligned along its inline direction. Instead, the amplitude behavior seems to be symmetrical across the twenty-four sources.

Adjustments such as removing outlier values to reduce the influence of environmental conditions and applying geometric corrections to account for offset-related variations, allowed the true component-based amplitude behavior to emerge more distinctly.

ii. Surface Wave Analysis - Croissant experimental data

Figures 6.27, 6.28 and 6.29 present the RMS amplitudes for the Surface Wave Analysis of the Vertical, Horizontal 1, and Horizontal 2 components, respectively, across the 2023, 2024, and 2025 data acquisitions.

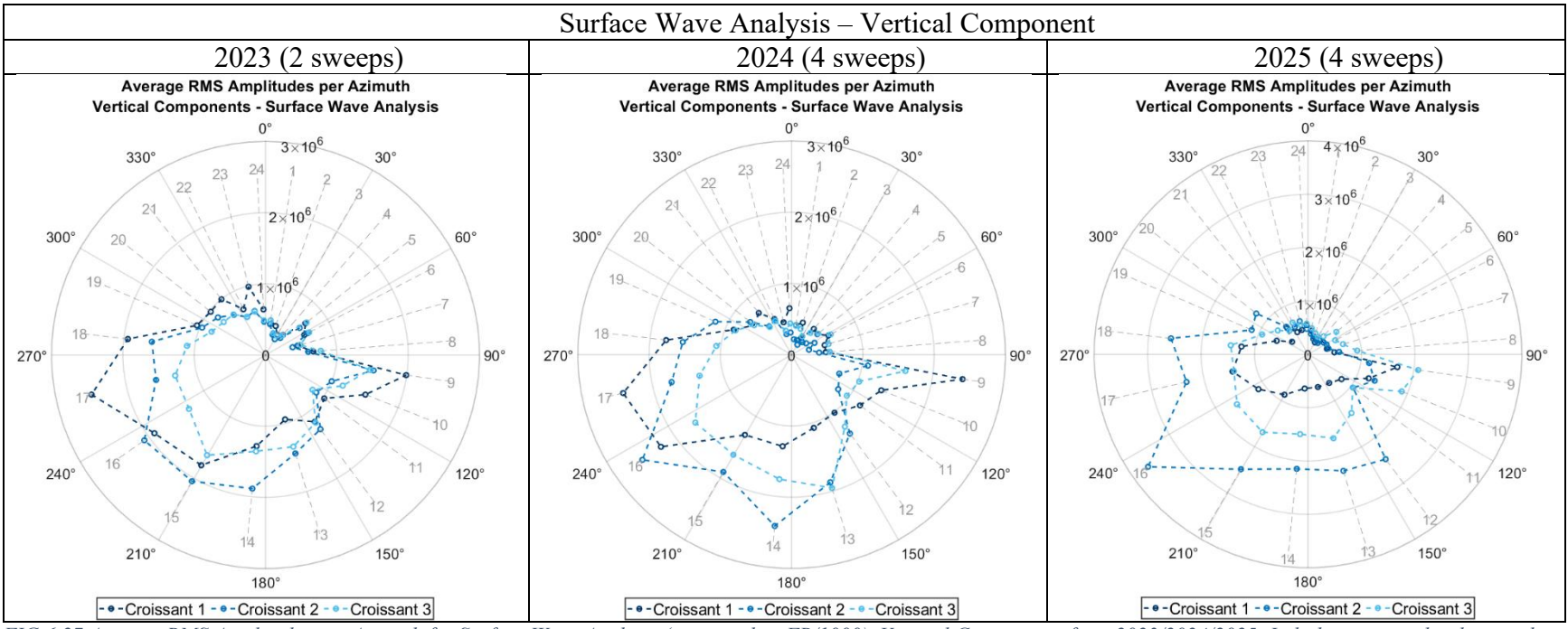


FIG 6.27 Average RMS Amplitudes per Azimuth for Surface Wave Analysis (time window FB/1000). Vertical Components from 2023/2024/2025. In light gray are the shot numbers (1-24). Radial axes correspond to the average RMS amplitude.

Amplitudes for vertical components in the surface wave analysis show a decrease in amplitudes for far offsets and an increase in amplitudes for near source-receiver offsets. Shot 9 still preserves the abrupt amplitude increase for 2023 and 2024 dataset.

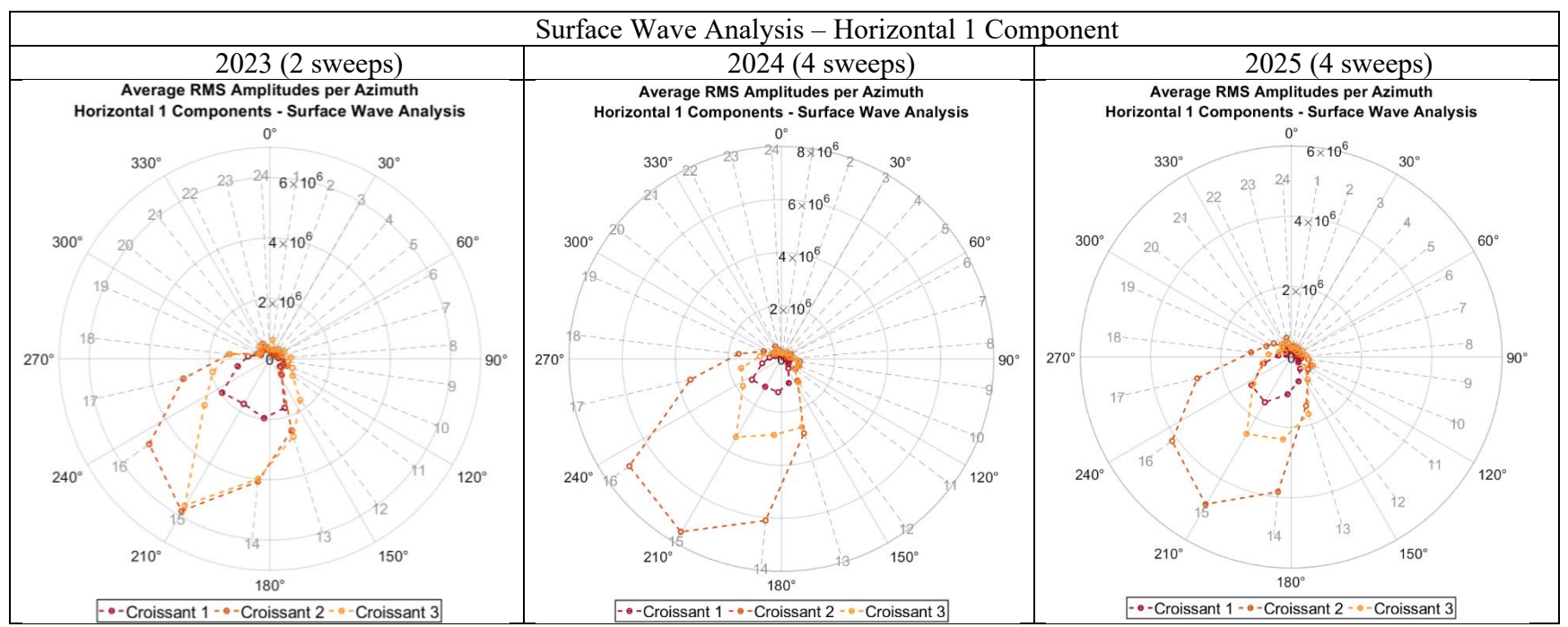


FIG 6.28 Average RMS Amplitudes per Azimuth for Surface Wave Analysis (time window FB/1000). Horizontal 1 Components from 2023/2024/2025. In light gray are the shot numbers (1-24). Radial axes correspond to the average RMS amplitude.

For the H1 component, amplitudes increase for azimuths ranging from approximately 180° to 280°, which is consistent with sources aligned along the axis of the H1 component. This observation supports the expected broadside sensitivity of the fiber, confirming that the DAS system is effectively capturing strain along its axial direction. Additionally, low amplitudes observed at far source–receiver offsets further confirm the expected geometrical spreading behavior, where wave amplitude diminishes with increasing distance, as observed also for the vertical component.

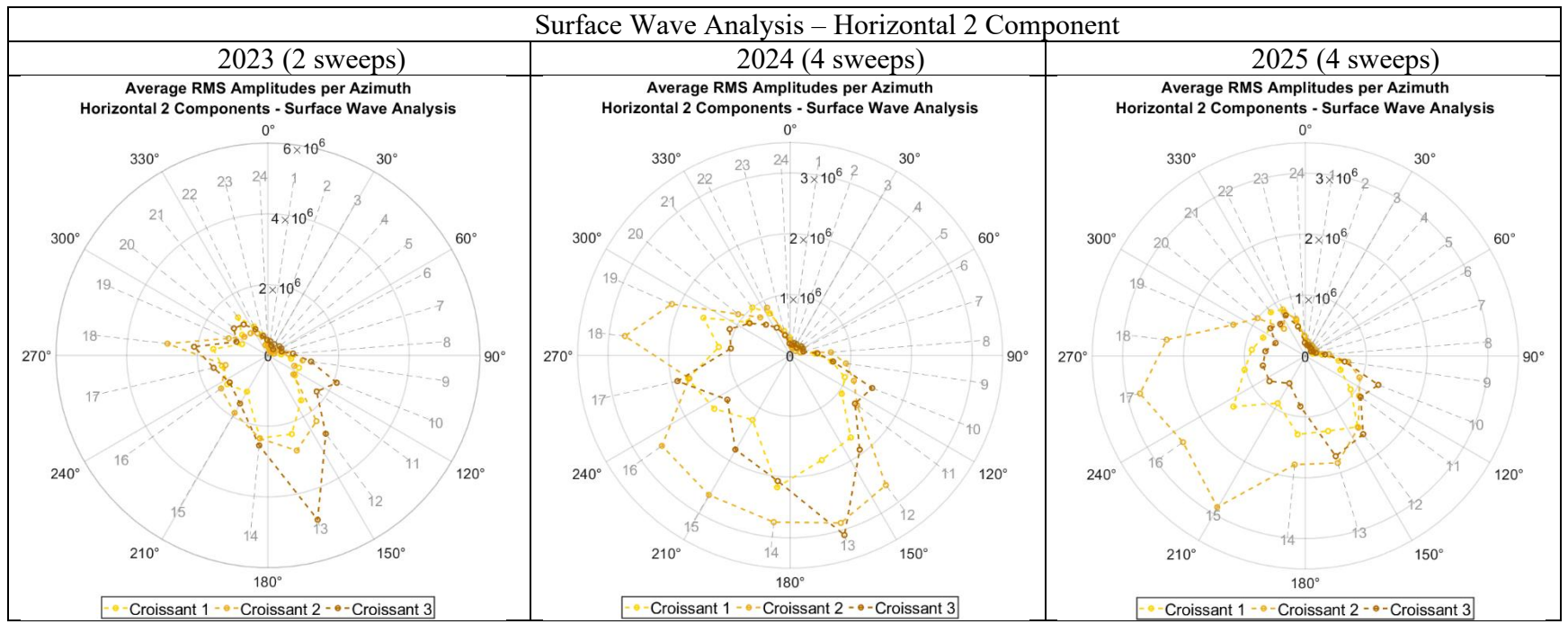


FIG 6.29 Average RMS Amplitudes per Azimuth for Surface Wave Analysis (time window FB/1000). Horizontal 2 Components from 2023/2024/2025. In light gray are the shot numbers (1-24). Radial axes correspond to the average RMS amplitude.

The H2 component, on the other hand, exhibits clear directional sensitivity in the 2023 dataset, with higher amplitudes observed for shots aligned along the H2 axis. However, this directional pattern appears less consistent in the 2024 and 2025 acquisitions.

Key observations for the surface wave analysis can be summarized as follows:

- 1. All three components (Vertical, H1, and H2) exhibit amplitude decay with increasing offset, consistent with the expected geometrical spreading behavior in a surface wave context (see Figure 6.30).
- 2. Geometric correction must be applied in order to account for the offset variation along the twenty-four shots.
- 3. No amplitudes anomalies are recorded by specific shot locations.

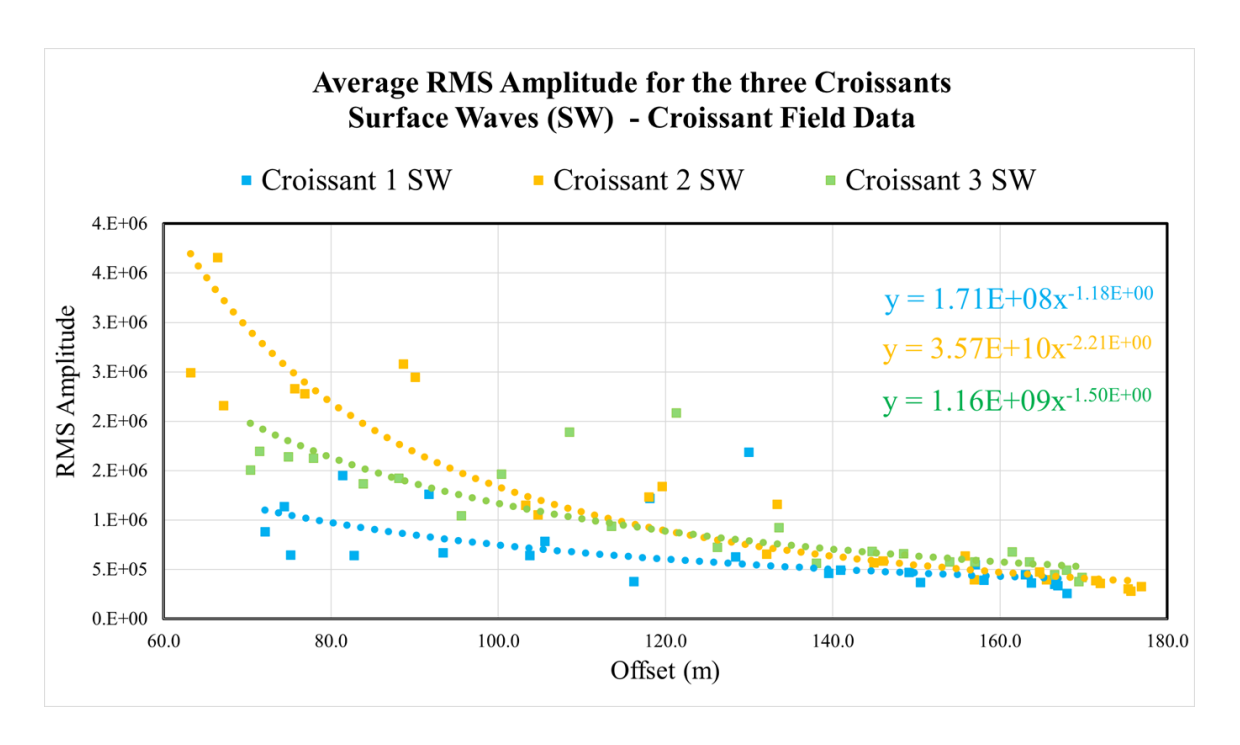


FIG 6.30. Average RMS amplitude vs Offset for the three Croissants for surface waves from the Croissant experimental data.

Power functions visible in the Figure 6.30 correspond to geometric corrections for Croissant 1, Croissant 2, and Croissant 3 respectively for surface wave RMS amplitudes.

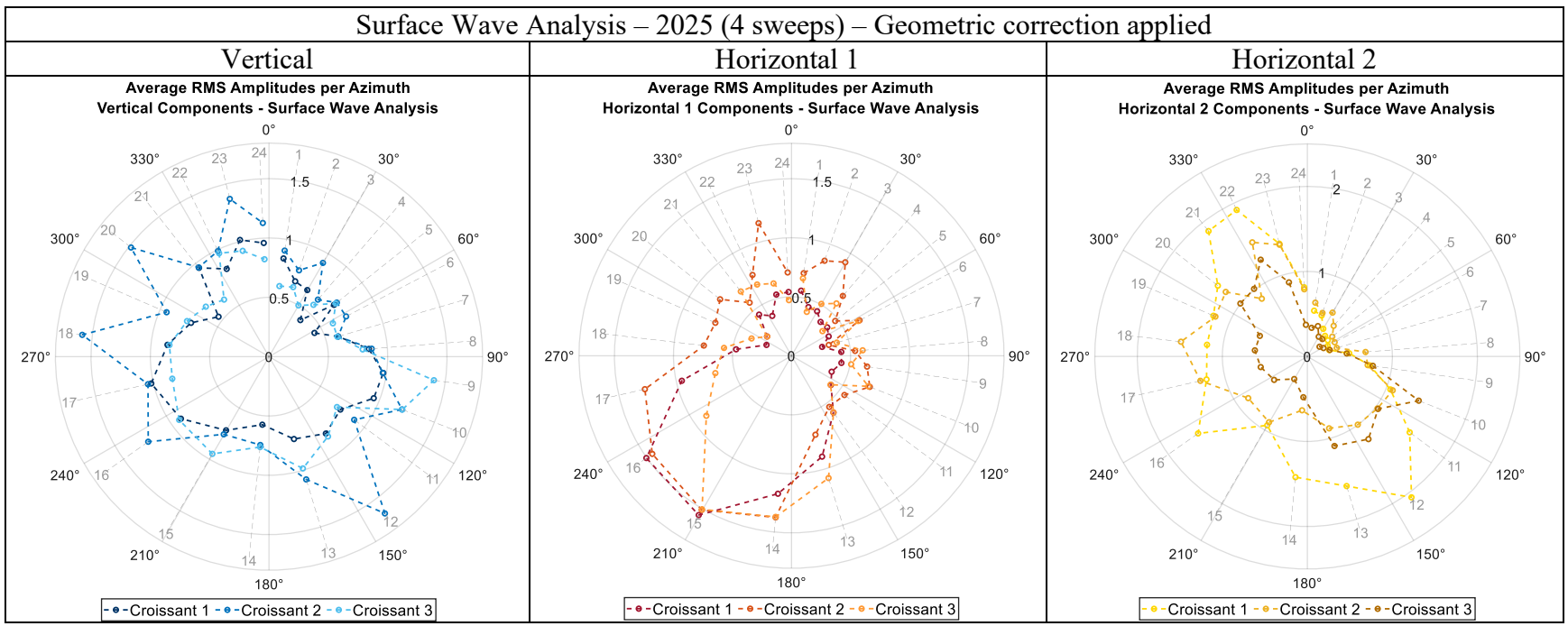


FIG 6.31. Average RMS Amplitudes per Azimuth for Surface Wave Analysis (time window 800ms). Vertical, Horizontal 1 and Horizontal 2 components from 2025 dataset. In light gray are the shot numbers (1-24). Radial axes correspond to the average RMS amplitude corrected by the geometric factor by Croissant.

Following the application of geometric corrections, several observations can be made for each component, as illustrated in Figure 6.31: 1) The vertical component displays a symmetric behavior. Surface waves—specifically Rayleigh waves—are characterized by retrograde elliptical particle motion, which combines both vertical and horizontal displacements. This elliptical motion influences the vertical component similarly across different azimuths, resulting in the observed symmetry. 2) Both horizontal components (H1 and H2) exhibit clear directionality and symmetry for inline sources and a decrease in amplitude for crossline sources. This behavior aligns with the expected response based on fiber orientation and the propagation characteristics of surface waves.

6.5 Signal to Noise Ratio Analysis

This section evaluates the signal-to-noise ratio (SNR) across multiple years of data acquisition, aiming to address key questions related to data quality and sensor performance:

- 1. Has there been any improvement in signal clarity in recent acquisitions, potentially due to better soil compaction or improved sensor coupling?
- 2. Does increasing the number of correlated sweeps lead to a measurable enhancement in SNR?
- 3. Considering that each Croissant component currently uses approximately 28 meters of wrapped fiber, how much of that length contributes reliably to the recorded signal?
- 4. Is it feasible to reduce the length of fiber per component to make the system more cost-effective and practical, without compromising signal quality?

By addressing these questions, this analysis will help guide future improvements in both data acquisition strategies and Croissant sensor design.

6.5.1 Effects of Soil Compaction and Sweep Count on SNR Improvement

The coupling of fiber-optic cables to the ground is crucial for the effective detection of seismic vibrations in DAS systems. Poor coupling can significantly degrade signal quality and limit the reliability of seismic interpretations. In surface deployments, achieving good coupling is particularly challenging due to loose soil, air gaps, or surface irregularities. To address this, the Croissant sensor array was buried approximately one meter underground to ensure stable and consistent contact with the surrounding soil, thereby enhancing its sensitivity and coupling efficiency. As noted by some authors ground coupling is a key consideration in the performance of surface-deployed DAS systems(Harmon et al. 2022).

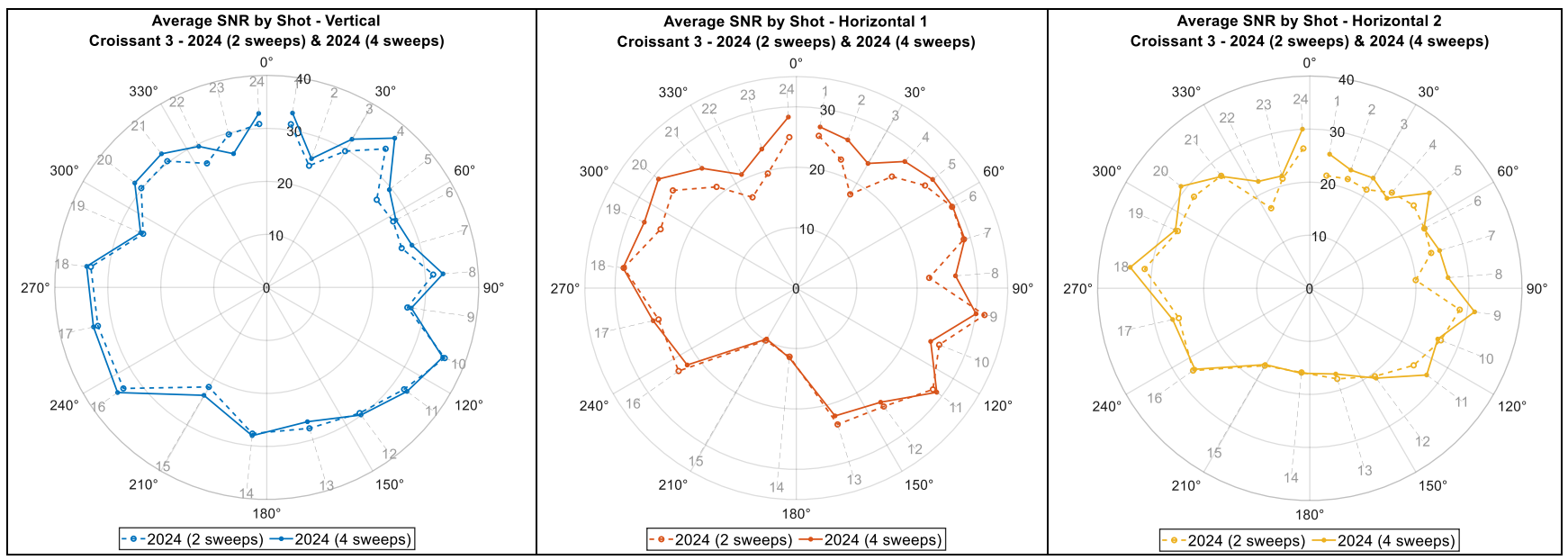


FIG 6.32 Representative signal to noise ratio for Croissant 3, comparing 2024 (2 Sweeps) and 2024 (4 Sweeps) data

Figure 6.32 shows the representative signal-to-noise ratio (SNR) for Croissant 3, which follows the same trend observed in the other two Croissants. Across all three components, a slight increase in SNR is evident with the increase in the number of sweeps. This observation supports the processing approach described in Section 4.4, where stacking additional sweeps enhances the recorded signal quality. Vertical components have a high signal to noise ratio, around 30dB and higher as compared to the H1 and H2 component, which are less than 30dB.

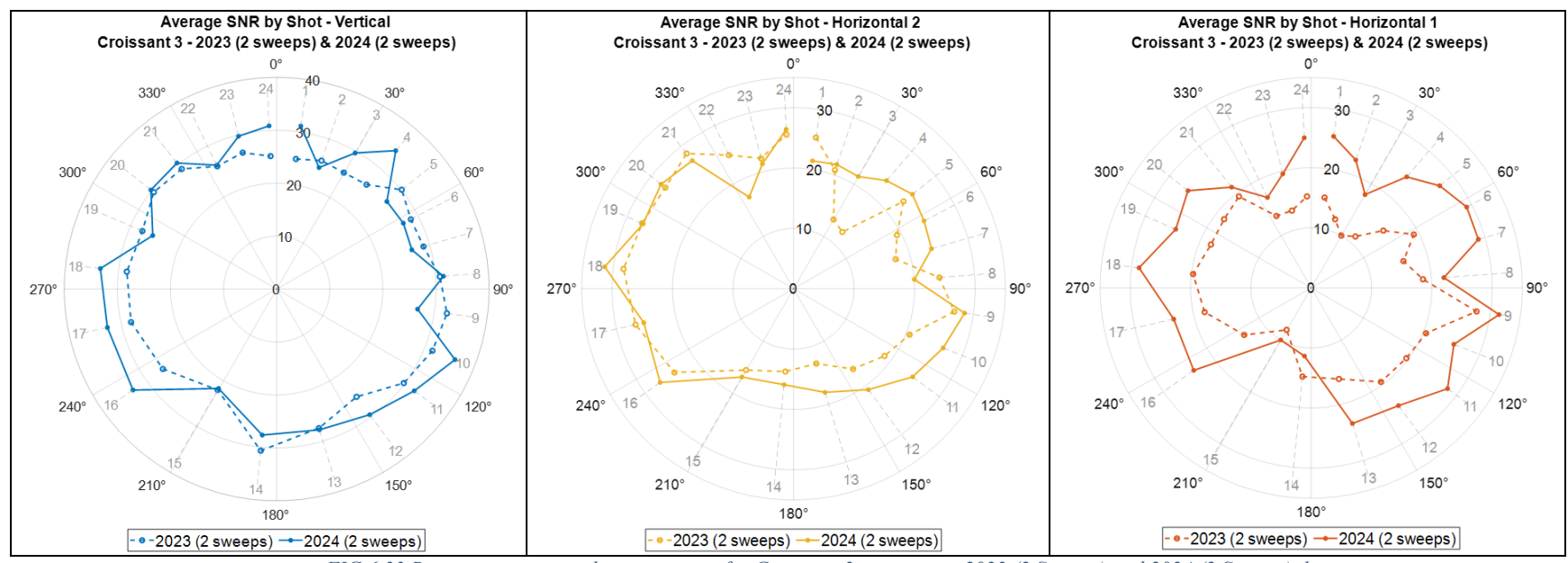


FIG 6.33 Representative signal to noise ratio for Croissant 3, comparing 2023 (2 Sweeps) and 2024 (2 Sweeps) data

Figure 6.33 presents a representative signal-to-noise ratio (SNR) for Croissant 3, with similar trends observed in the other two Croissants. In this case, the comparison is between datasets with the same number of stacked sweeps (2) but acquired a year apart—2023 and 2024. Overall, the 2024 dataset shows an increase in SNR. This supports the statement by Hall et al. (2024) that one year of soil or clay compaction can lead to improved signal-to-noise ratios for data recorded by Croissant sensors. Observation about the relative signal to noise ratio between components, show that the vertical component maintains a higher decibel values.

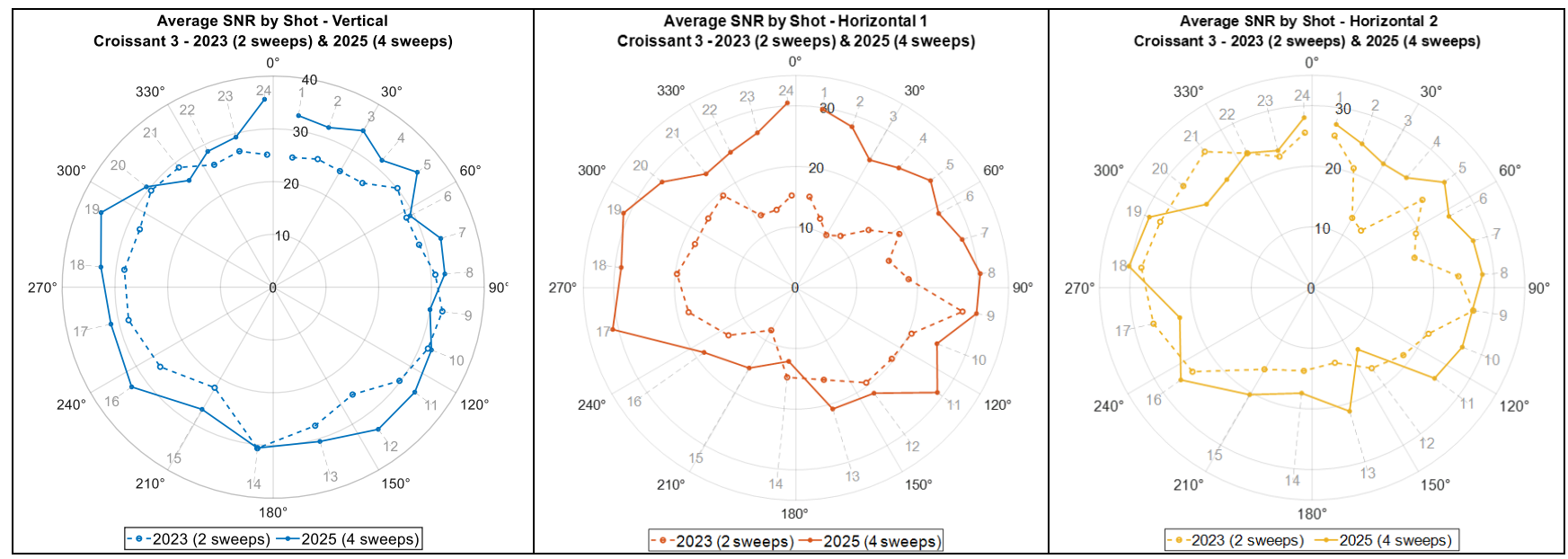


FIG 6.34 Representative signal to noise ratio for Croissant 3. Comparison between 2023(2S) and 2025(4S) data

Figure 6.34 presents the representative signal-to-noise ratio (SNR) for Croissant 3 and illustrates a similar trend observed in the other two Croissants. It compares the 2023 dataset (recorded with 2 stacked and correlated sweeps) with the 2025 dataset (recorded with 4 stacked and correlated sweeps). The three plots show the SNR for the Vertical, Horizontal 1 (H1), and Horizontal 2 (H2) components. Across all components, there is a clear increase in SNR for the 2025 data compared to 2023. This improvement may be attributed not only to the higher number of sweeps, but also to improved coupling between the sensor and the ground over time. Signal to noise ratio for vertical component keeps the higher values compared to H1 and H2.

These observations suggest that after two years of burial, the Croissant sensors achieved better soil coupling, which contributed to enhanced seismic signal quality.

The key observations from the three tables presented in this section are as follows:

- 1. Increasing the number of stacked sweeps leads to an improvement in the signal-to-noise ratio (SNR).
- 2. Natural soil compaction over time enhances the coupling between the fiber and the ground, resulting in higher SNR in the acquired data.
- 3. The vertical component consistently shows higher signal-to-noise ratios compared to the horizontal components, suggesting better coupling or sensitivity for vertical ground motion—especially relevant for P-wave energy and source-receiver geometry.
- 4. SNR improvements are not uniform across all shots or components, indicating that local ground conditions, shot location, or sensor orientation may still play a role in SNR variability despite overall trends.

6.5.2 Stacked traces vs SNR

The current Croissant design uses approximately 28 meters of fiber-optic cable per component. This raises an important design question: can we reduce the total length of fiber used per component without significantly compromising signal quality?

As Hall et al., (2023) stated, "twenty-eight meters was chosen for the wrap because it is the same length as four 7 meters gauge lengths, giving us three-gauge lengths worth of data from the sensor that will be uninfluenced by fiber in the adjacent frames and trenches". Then "three-gauge lengths of worth data" are equivalent to approximately 21 traces, every 1 meter apart, where strain is reliably measured within the frame boundaries.

With this configuration in mind, the question becomes: how many of these 21 effective traces are necessary to maintain an acceptable signal-to-noise ratio (SNR)? Can we reduce the number of traces—and thus the required cable length—while still preserving data quality?

Stacking traces is a well-established technique for improving SNR. In fact, for the automatic first breaks, the traces were stacked by components to enhance the SNR, enabling more accurate picking.

Theoretically, the SNR increases proportionally to the square root of the number of stacked traces (\sqrt{N}) in Common Midpoint (CMP) stacking (Kumar and Sinha, 2008), where different source and receiver locations are used.

This relationship is based on two primary assumptions:

- The seismic signal is assumed to be identical and in phase across all traces being stacked.
 This coherence ensures constructive interference, allowing the signal amplitude to increase linearly with the number of traces.
- 2. The noise is assumed to be random, uncorrelated, and independent from one trace to the next. As a result, when the traces are summed, the noise components interfere destructively.

In this case, the evaluation and comparison of the SNR is conducted by stacking traces from a single shot for every component across independent receiver locations (Croissant 1, 2, and 3). For the vertical component, the signals appear to be fairly coherent, as observed in Figures 6.6, 6.10, and 6.12. This suggests that the assumption of signal coherence—necessary for constructive interference during stacking—holds reasonably well for this component. However, for the horizontal components, this assumption does not always apply. Variability in signal alignment and amplitude can lead to reduced coherence, undermining the effectiveness of stacking.

Furthermore, the assumption that noise is random, uncorrelated, and independent across traces cannot be fully justified in this experimental setup. In practice, coherent noise—such as surface waves, instrument noise, or environmental disturbances—may be present and correlated across receivers, not meeting the conditions required for destructive interference during stacking.

Even though the theoretical \sqrt{N} improvement in SNR may seem appropriate, the specific conditions of this experiment, including the single-shot configuration, variability in signal coherence, and the presence of coherent noise, suggest that this assumption may not hold strictly. Therefore, observed SNR improvements may deviate from the theoretical model.

Figure 6.35 presents representative SNR values as a function of the number of stacked traces, offering a practical framework to evaluate how much the cable length—and therefore the number of traces—can be reduced while still maintaining data quality.

The SNR was calculated within a 20 ms window, ensuring that the first full period of the wavelet corresponding to the first arrival was captured.

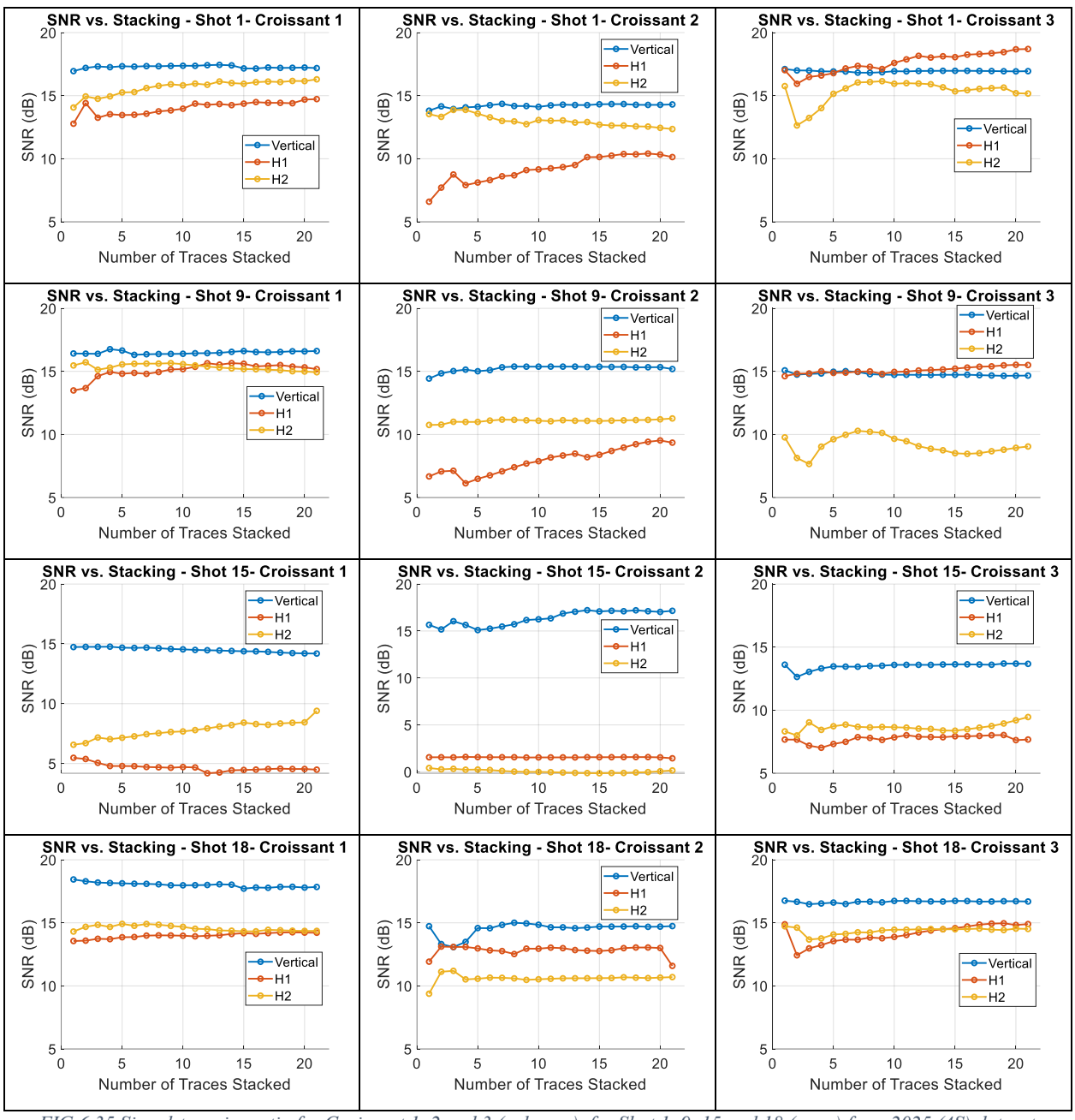


FIG 6.35 Signal-to-noise ratio for Croissant 1, 2 and 3 (columns), for Shot 1, 9, 15 and 18 (rows) from 2025 (4S) dataset

Figure 6.35 show that Vertical components consistently show higher SNR values than both horizontal components. Increasing the number of stacked traces (N) does not significantly increase the SNR for the component. A nearly constant SNR suggests that the vertical signal is coherent and stable, and that stacking doesn't enhance considerably.

Horizontal Components (H1 and H2) exhibit more variability and generally lower SNRs. In many cases (e.g., Shot 1 and 15 - Croissant 1; Shot 18 – Croissant 3), H1 and H2 show some improvement with stacking. In other cases, H1 and H2 remains relatively constant (e.g., Shot 15 - Croissant 2 and 3; Shot 18 – Croissant 1 and 2). This indicates that signal coherence is weaker in the horizontal components, possibly due to coherent noise.

The overall stability implies that the waveform within the selected time window (used for signal and noise calculation) is effectively the same across the stacked traces.

There is no consistent trend of increasing SNR across all components of a given Croissant for a specific shot. This variability among traces suggests that signal quality is highly dependent on local factors, making it difficult to accurately determine a specific amount of cable that could be reduced or increased without compromising data quality.

The vertical component appears more promising in terms of consistently higher signal-tonoise ratio (SNR) and greater stability. However, as demonstrated throughout the previous
analyses, this performance is ultimately influenced by local geological conditions. In this case, the
presence of strong refracted waves contributes to increased energy in the vertical component,
which explains its favorable SNR behavior. Therefore, for this project, the vertical component
naturally exhibits stronger and more stable signals.

Based on the 21 traces of worth data considered within the 1-meter frame for each component, it is evident that the SNR shows minimal improvement or change beyond a certain number of traces. The stable SNR across the 21 traces—equivalent to approximately three-gauge lengths—indicate that a significant portion of these traces present the same seismic signature and may be redundant.

This analysis suggests that at least one full gauge length of high-quality data—approximately 7 traces—may be sufficient to maintain signal integrity. Consequently, the required number of cable wraps could be reduced from the initial 28 meters per component to approximately 14 meters (around 7 wraps), without compromising data quality. This has significant implications for cost-effective and efficient sensor design, especially in applications where enabling rapid deployment is critical.

7. CHAPTER 7: Co-Located Geophone data

The inclusion of geophone data was a crucial step in validating and strengthening the interpretation of the DAS (Distributed Acoustic Sensing) recordings. Co-located geophones provide a valuable reference to assess the quality, fidelity, and signal characteristics of the DAS measurements.

Previous studies have shown encouraging comparisons between DAS and conventional seismic sensors. For example, Correa et al. (2017) demonstrated that field DAS data quality compares well with recordings from co-located geophones or seismometers. Similarly, Wang et al. (2018) presented a wiggle-by-wiggle match between DAS and a nodal array, revealing comparable noise levels. These findings are promising for the objectives of this study, which aims to evaluate whether the Croissant DAS configuration can function as a reliable point sensor—an assessment that is further supported by comparisons with co-located geophone data.

In this chapter, the co-located geophone data is analyzed and compared to the Croissant DAS recordings, providing insight into the trace's differences, amplitude scaling, frequency and signal-to-noise characteristics.

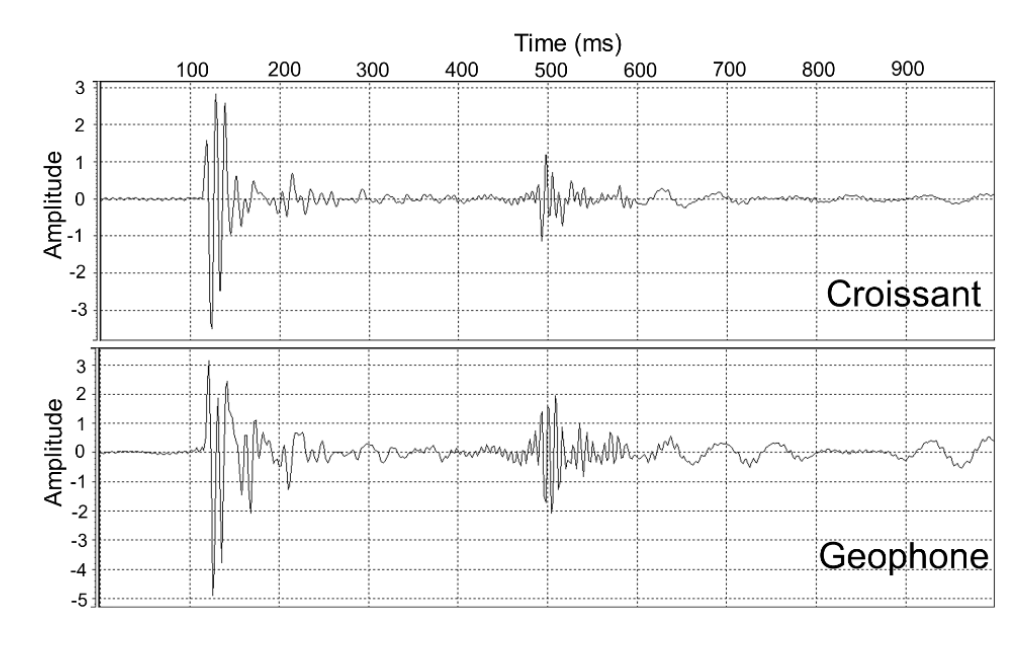


FIG 7.1. Trace comparison from Croissant and Geophone for shot 4, the farthest shot (vertical component of Croissant 1 and geophone in Croissant 1 location)

As described in Section 4.3.2 and shown in Figure 4.7, the raw traces from the nine colocated geophones were extracted for analysis. These are 3-component geophones, recording one vertical and two horizontal components. To preserve the acquisition geometry and allow for meaningful comparison with the DAS system, during the acquisition the horizontal geophone components were aligned with the H1 and H2 orientations of the Croissant sensors.

In Figure 7.1, a trace-by-trace comparison is presented for Shot 4, which corresponds to the farthest source-receiver offset in the acquisition setup.

The trace comparison reveals strong similarities between the Croissant DAS and geophone data in terms of first-break timing, phase alignment, and the arrival of S-waves and surface waves. However, the geophone traces exhibit higher frequency content, which is consistent with the broader bandwidth response of conventional point sensors.

Figure 7.2 shows the amplitude spectra for the co-located geophone (left) and a representative Croissant DAS trace (right). The geophone data clearly exhibit higher frequency content, with significant amplitude energy present above 20 Hz. In contrast, the Croissant DAS data show a concentration of energy predominantly below 20 Hz, indicating a more limited high-frequency response.

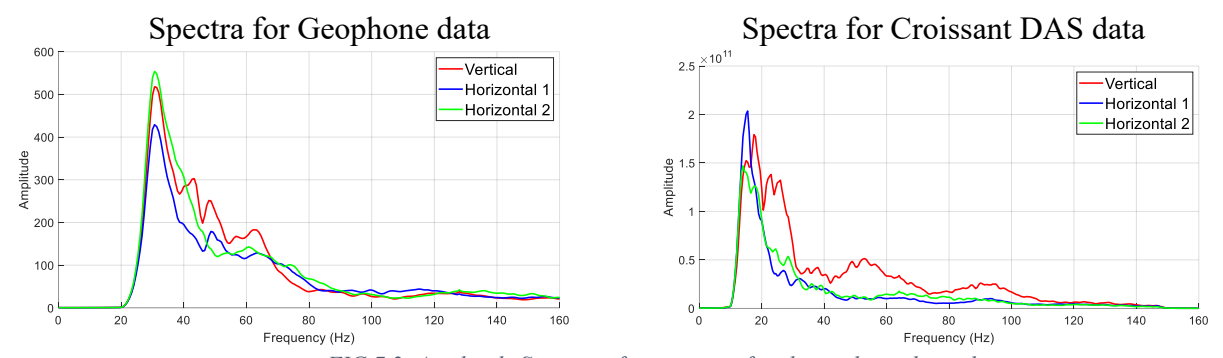


FIG 7.2. Amplitude Spectrum from traces of co-located geophone data.

7.1 Amplitude Analysis for Co-located Geophones

The amplitude analysis for the co-located geophone data will follow the same methodology as previously applied in Section 6.3 for the Croissant data, focusing on both first arrivals and surface waves.

As mentioned earlier, three 3-component (3C) geophones were co-located at the position of each Croissant sensor. Therefore, for each Croissant (referred to as a "sensor" in the following figures to avoid confusion with Croissant-specific data), there will be three vertical, three H1, and three H2 component traces. These traces will be analyzed in two separate time windows — one for the first arrivals and another for the surface waves — to evaluate the sensitivity and consistency of the geophones in comparison to the Croissant sensors.

i. First Arrival Analysis - Co-located Geophone data

The Figure 7.3 presents the amplitude analysis for the traces corresponding to the vertical component, the horizontal component aligned with the H1 component, as well as the component H2 for the twenty-four shots of L41 for the co-located geophone traces.

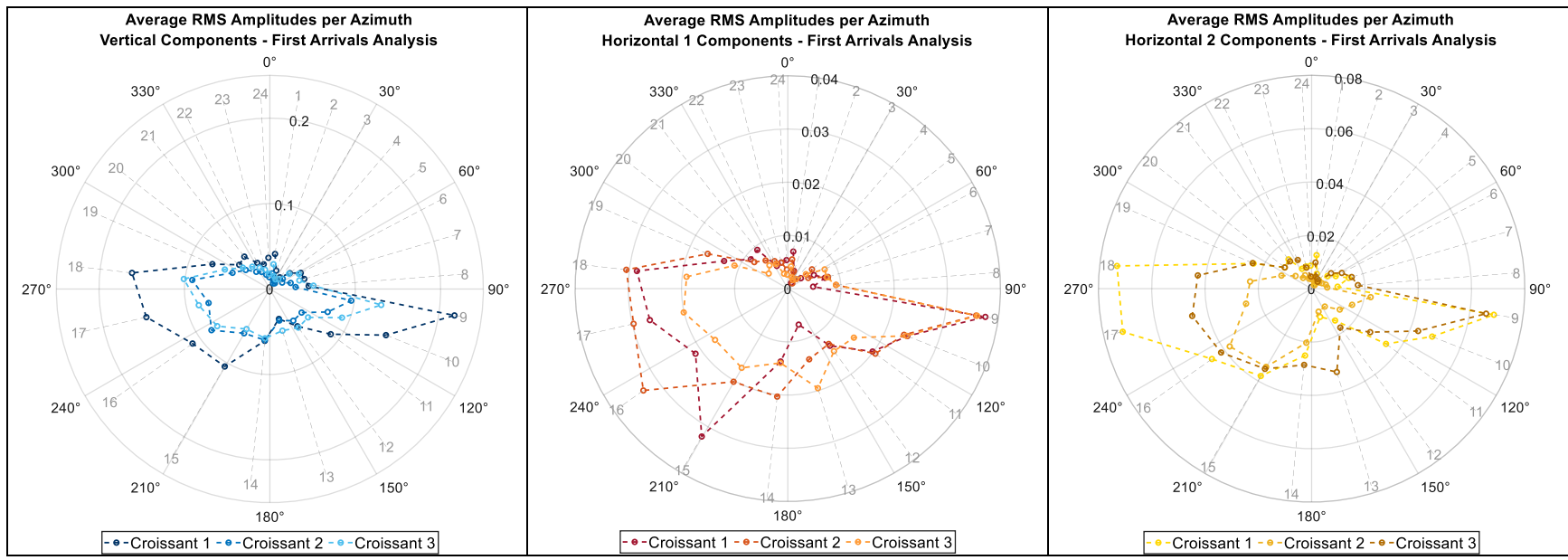


FIG 7.3 Average RMS Amplitudes per Azimuth for First Arrival Analysis (time window 30ms). Vertical, Horizontal 1 and Horizontal 2 traces from co-located geophones. In light gray are the shot numbers (1-24). Radial axes correspond to the average RMS amplitude.

The first notable observation from the co-located geophone data is the consistently high amplitudes across all three components for shots 9, 10, 17, and 18. These persistent anomalies are consistent with the high amplitudes observed in the Croissant DAS data. Wet ground conditions during the acquisition, resulting from snowmelt in low-elevation zones (as shown in Figure 6.25), may have further influenced energy transmission at these locations in the particle velocity response.

Regarding amplitude variation with offset, the geophone data exhibit the same trend observed in the Croissant DAS data: higher amplitudes at near source-receiver offsets and progressively lower amplitudes at greater offsets. This consistent pattern is in agreement with the expected effects of geometrical spreading of seismic energy.

To quantify this behavior, the average RMS amplitudes obtained from the first arrival time window were plotted against offset. From these results, the geometric spreading factor was derived for each trio of co-located geophone traces at every sensor (Croissant) position. For this analysis, only the vertical component data were used in calculating the geometric factor.

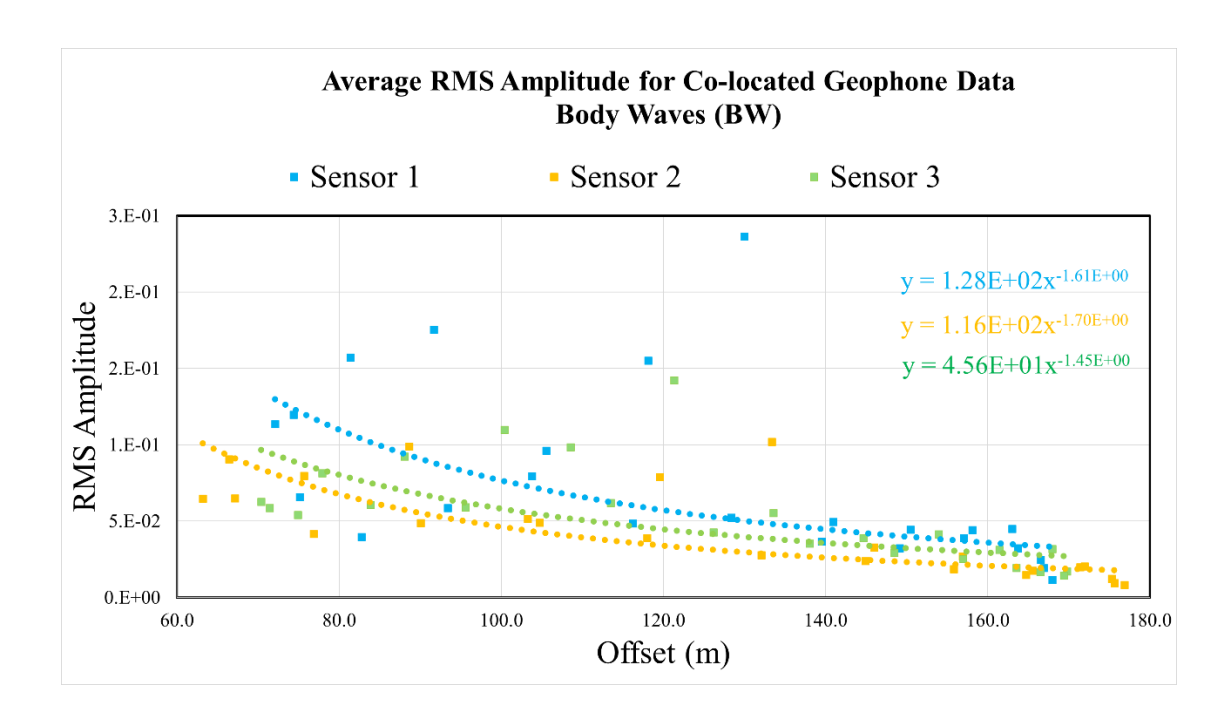


FIG 7.4. Average RMS amplitude vs Offset for the traces of the co-located geophones. Geometric correction obtained from a power trend for the first arrival time window.

A geometric spreading correction was applied (functions to the upper-right of Figure 7.4) to the data to account for amplitude decay with offset. Additionally, the four shots exhibiting anomalously high amplitudes—shots 9, 10, 17, and 18—were excluded from the analysis to avoid biasing the results.

As a result, Figure 7.5 shows just azimuthal behavior of co-located geophone raw data.

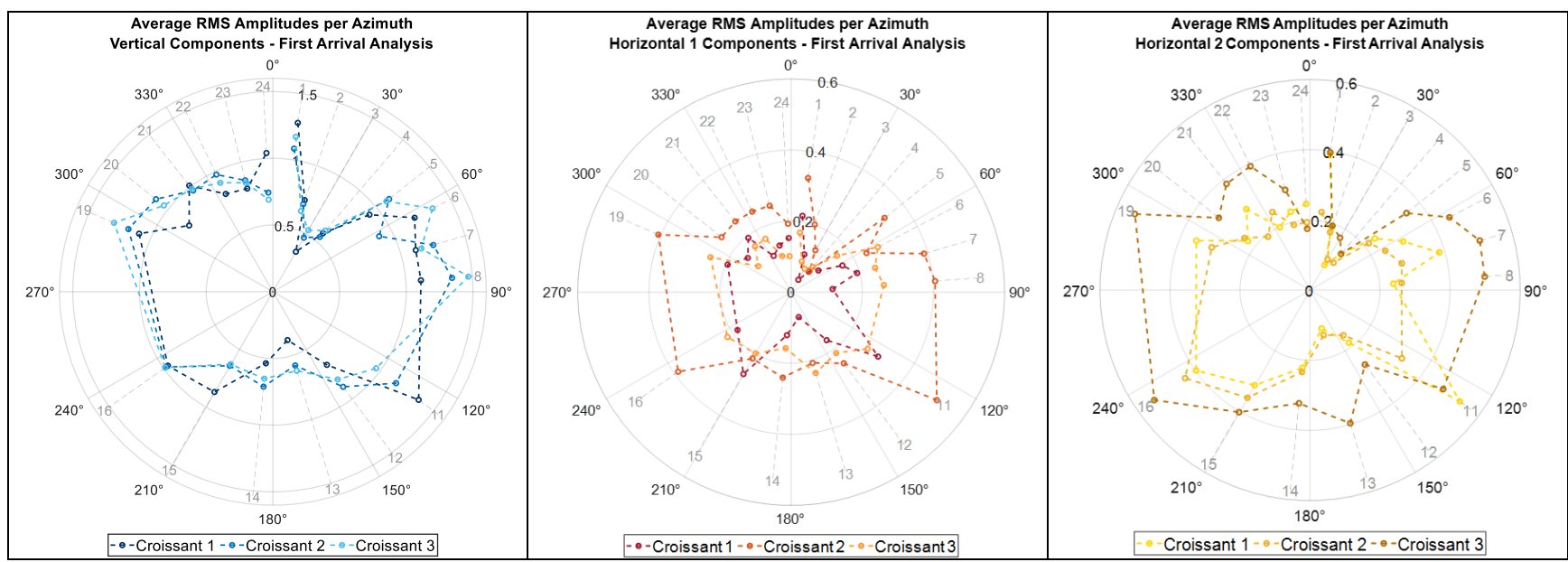


FIG 7.5 Average RMS Amplitudes per Azimuth for First Arrival Analysis (time window 30ms) corrected by geometrical factor. Vertical, Horizontal 1 and Horizontal 2 traces from co-located geophones. In light gray are the shot numbers (1-24). Radial axes correspond to the average RMS amplitude. Shots 9, 10, 17, and 18 deleted due to high amplitudes.

Figure 7.5 shows a more symmetric amplitude distribution in the vertical component. For the H1 and H2 components, there is no clear directional sensitivity or consistent azimuthal preference as expected and seen for the Croissant DAS data. This can be caused by several factors, such as sensor (geophone) orientation and coupling.

ii. Surface Wave Analysis - Co-located Geophone data

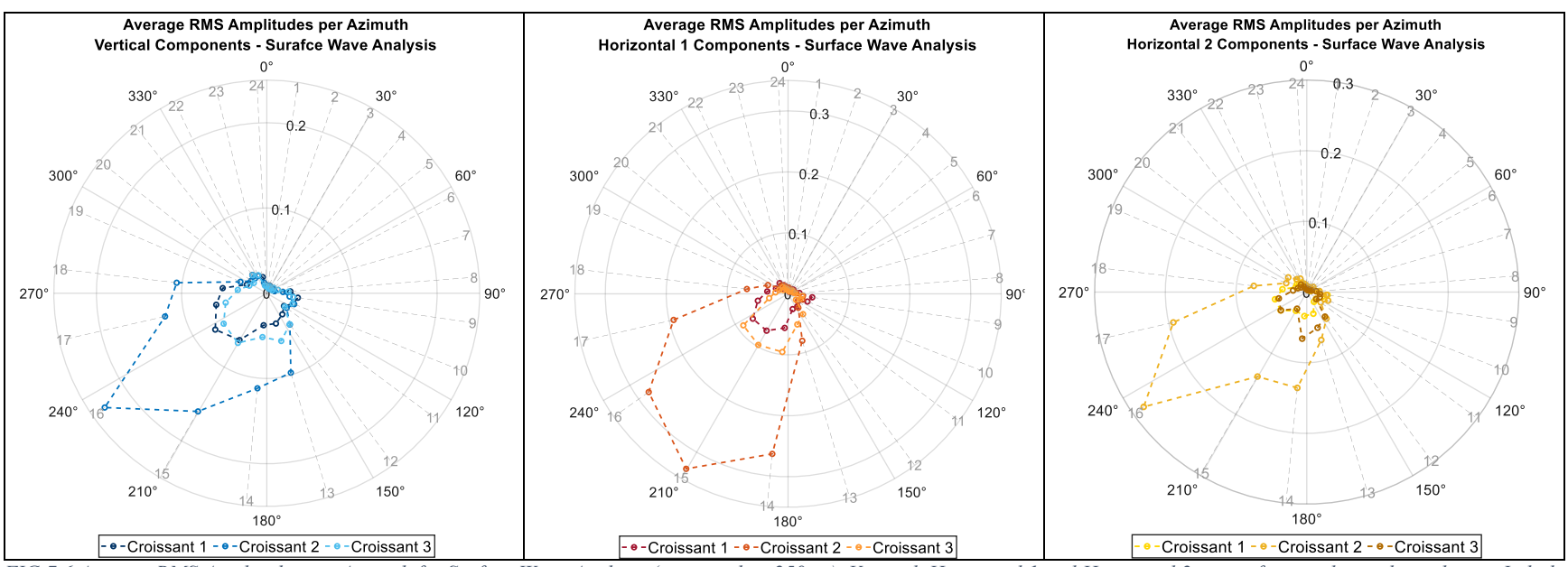


FIG 7.6 Average RMS Amplitudes per Azimuth for Surface Wave Analysis (time window 250ms). Vertical, Horizontal 1 and Horizontal 2 traces from co-located geophones. In light gray are the shot numbers (1-24). Radial axes correspond to the average RMS amplitude.

For surface waves, a general decrease in amplitude with increasing offset is observed across all three components, as shown in Figure 7.6. However, a noticeable trend of elevated amplitudes is present at near offsets—particularly for shots 13 to 18—across the vertical, H1, and H2 components. After applying the geometric spreading correction to the surface wave window and deleting the shot 9 due to presence of high amplitudes, the resulting data are presented in Figure 7.7, which highlights the azimuthal amplitude behavior.

Figure 7.7 shows a relatively symmetrical amplitude distribution across the vertical, H1, and H2 components. Rayleigh waves are characterized by elliptical particle motion in the vertical plane aligned with the direction of propagation. These waves primarily affect the vertical and in-line horizontal components, generating stronger responses when the sensor axis is aligned with the propagation

direction—as is the case for the H1 component in this configuration. For the H2 component, the behavior is less clear; however, a noticeable decrease in amplitudes is observed for shots 13 to 15, which are aligned with the H1 axis.

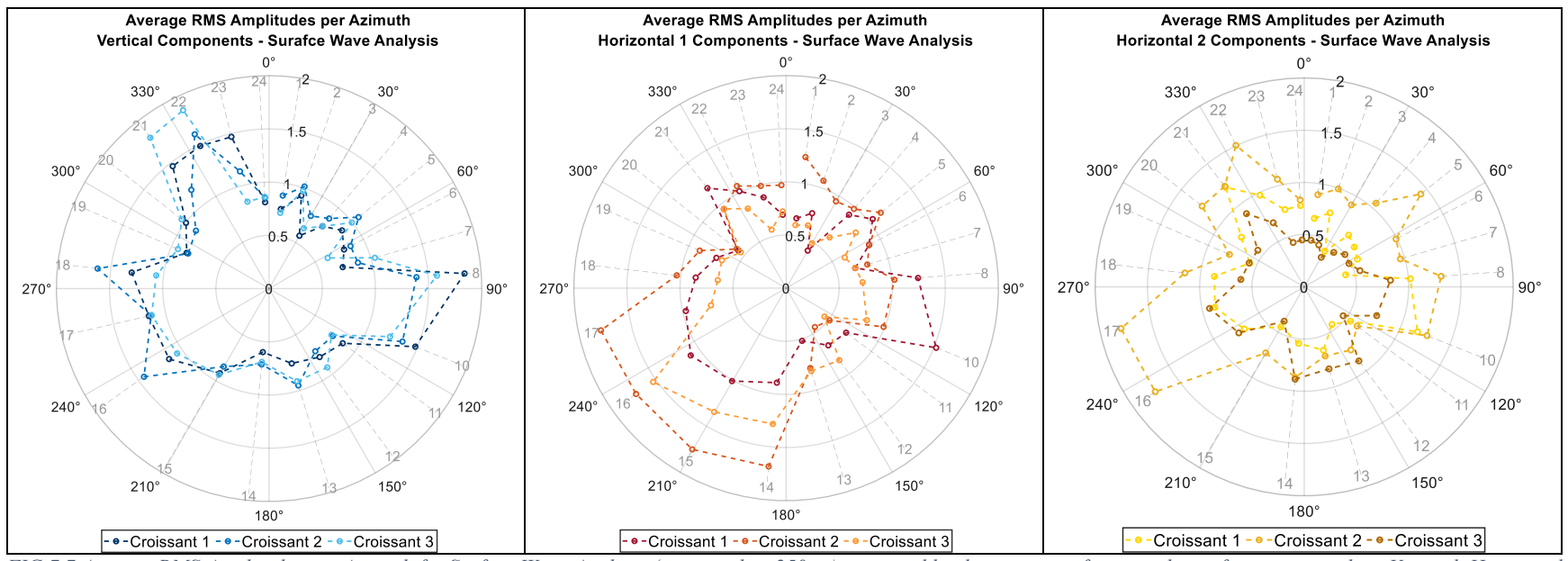


FIG 7.7 Average RMS Amplitudes per Azimuth for Surface Wave Analysis (time window 250ms) corrected by the geometric factor in the surface wave window. Vertical, Horizontal 1 and Horizontal 2 traces from co-located geophones. In light gray are the shot numbers (1-24). Radial axes correspond to the average RMS amplitude.

This observation supports the sensitivity of the 3C geophones along the H1 and H2 axes in the Croissant configuration. Furthermore, the elevated amplitudes in this dataset highlight how near-surface conditions and terrain characteristics can significantly influence amplitude response.

In conclusion, the amplitude analysis confirms that geophone orientation, source-receiver geometry, and local ground conditions all play critical roles in the amplitude behavior of surface waves and should be carefully considered in any interpretation or sensor comparison.

Conclusions

This thesis explored the feasibility of enhancing DAS systems through the integration of a compact, multi-component, point-based sensor referred to as the *Croissant*. DAS offers several well-known advantages—such as low cost, long-term monitoring capabilities, and the use of the same fiber, interrogator, and infrastructure—but it also has limitations, particularly its broadside sensitivity to seismic energy arriving perpendicular to the fiber. This work aimed to investigate whether single-component DAS data, despite their inherent directional limitations, can still be effectively used for seismic monitoring when supported by localized sensing of the full multicomponent seismic wave field.

Through a combination of experimental data acquisition (2023–2025), analytical modeling, and numerical simulations, I evaluated the directional sensitivity, amplitude response, and signal fidelity of the Croissant sensor under various subsurface and acquisition conditions. The goal was to determine whether this design could reliably capture multicomponent strain data in subsurface deployments and how well these measurements align with theoretical expectations and conventional geophone data.

Below, I present the key findings of this work:

- 1. Croissant as a multicomponent DAS sensor: the Croissant sensor successfully worked as a point-based, multicomponent DAS unit across all three acquisition years. Its ability to record vertical and horizontal strain components was consistent and reliable, providing interpretable and meaningful amplitudes with particularly strong vertical responses across all the shots, due to the geology in the area. These findings support the feasibility of its compact design for shallow-burial and permanent seismic monitoring.
- 2. **Modeling and parametrization:** A geometric DAS model was constructed by parameterizing the Croissant's fiber trajectory based on arc-length of cable used, physical dimensions, wrapping patterns and dimension layout. This model allowed the simulation of DAS responses in homogeneous and layered elastic media. These synthetic shot gathers were crucial in

- interpreting experimental data and understanding the role of body and surface waves in the sensor's response.
- 3. Synthetic vs. Experimental data consistency: Synthetic DAS data, generated using the ElasWave3D finite-difference software, aligned well with the experimental Croissant DAS data. Amplitude decay, and directional response showed strong agreement. For synthetic data, surface wave amplitudes followed a $1/\sqrt{r}$ decay trend, while body waves displayed 1/r behavior—both consistent with theoretical expectations. Experimental data followed a $1/\sqrt{r}$ decay trend for both first arrival and surface waves.
- 4. **Subsurface interpretation and critical distances:** By leveraging synthetic geophone outputs from *ElasWave3D*, I was able to estimate important seismic parameters including refractor depth, crossover and critical distance, and critical angle. These supported the hypothesis that refracted energy, particularly with a dominant vertical component, was being detected by the Croissants and co-located geophone experimental data.
- 5. **Amplitude behaviour by component and wave field interactions:** Amplitude and directionality analyses revealed that:
- The geometric correction factor was essential for removing offset-related effects from the average RMS amplitude versus azimuth plots. This correction enabled a clearer visualization of azimuthal amplitude behavior within the selected time windows.
- Local low-elevation areas showed a significant increase in transmitted energy, resulting in outliers within the recorded amplitude data for the first arrival analysis.
- The vertical components consistently showed stronger first arrivals, which supports the presence of near-vertical refracted (body) waves.
- The H1 component exhibited clear directionality along its axis in both surface and body wave analyses, reflecting expected behavior based on acquisition geometry and wave propagation.
- The H2 component showed less consistent directionality in the body wave window, likely due to lower energy levels recorded along this horizontal orientation. However, in the surface wave window, H2 displayed a clearer directional response, suggesting stronger surface wave interactions along its axis.

- 6. Signal-to-Noise enhancements: Comparing 2023-2024, and 2023-2025 data demonstrated measurable improvements in signal clarity, likely due to better coupling due to soil compaction. Additionally, stacking more sweeps before correlation during processing consistently enhanced signal-to-noise ratios.
- 7. **Design and practical considerations:** While each Croissant component currently utilizes approximately 28 meters of fiber, initial testing suggested this length may be reduced to 14 meters without sacrificing data quality. This reduced length still fits within the existing Croissant frame dimensions and includes one full gauge length of high-quality data, plus an additional gauge length to account for traces potentially affected by connector segments. This finding has meaningful implications for optimizing sensor design, cost-effectiveness and deployment.
- 8. Co-located geophone comparisons: Co-located geophone data played a crucial validation role. It confirmed key first arrivals and directional trends seen in the DAS data, though it also highlighted the Croissant's more limited high-frequency response. Amplitude anomalies were also observed, confirming the explanation in low-terrain areas what affected the signal in at specific shot locations (e.g., Shots 9, 10, 17 and 18).

Future work

I have demonstrated the feasibility and utility of the Croissant as a point-based, permanent, multicomponent DAS sensor, however, several ideas for future research remain:

- 1. **Optimization of fiber length for the Croissant:** Future work could explore modifications to the Croissant's frame dimensions, gauge length, and number of fiber wraps knowing that at least twice the gauge length of fiber optic cable can be used without compromising data quality by component. Such optimization could improve cost-effectiveness. It is important to note the limitations of fiber-optic cables, particularly their restricted bend radius. Excessive bending in the system can lead to signal attenuation or even physical damage to the fiber, complicating design and deployment strategies.
- 2. Rotation of horizontal components to radial and transverse: rotating the H1 and H2 components into radial and transverse coordinates (relative to source direction) could enhance the physical interpretability of the recorded data. A comparison with similarly rotated geophone data could clarify energy distribution and phase behavior. Some questions include:
 - Can a meaningful radial-transverse comparison be established between DAS and geophones?
 - Is there measurable energy loss or distortion in the DAS signal due to broadside sensitivity of the fiber?
- 3. **Estimation of the full 6-Component strain tensor**: future work could assess whether the Croissant sensor array configuration allows for the mathematical reconstruction of the full 6-component strain tensor. This would represent a significant advancement, enable comprehensive analysis of the full elastic wave field and potentially enhance applications in microseismic monitoring or full waveform inversion.
- 4. Conversion of geophone data to strain or strain rate: convert co-located geophone data to equivalent strain or strain-rate units would allow for direct amplitude comparisons with DAS data. This would provide a quantitative basis for evaluating measurement equivalency, validating DAS responses.

Bibliography

Ajo-Franklin JB, Dou S, Lindsey NJ, Monga I, Tracy C, Robertson M, Rodriguez Tribaldos V, Ulrich C, Freifeld B, Daley T, et al. 2019. Distributed Acoustic Sensing Using Dark Fiber for Near-Surface Characterization and Broadband Seismic Event Detection. Sci Rep. 9(1):1328. doi:10.1038/s41598-018-36675-8.

Aki K, Richards P. 2002. Quantitative Seismology. 2nd Edition. University Science Books.

Bakku SK. 2015. Fracture characterization from seismic measurements in a borehole. Massachusetts Institute of Technology.

Bakulin A, Silvestrov I, Pevzner R. 2020. Surface seismics with DAS: An emerging alternative to modern point-sensor acquisition. The Leading Edge. 39(11):808–818. doi:10.1190/tle39110808.1.

Becker MW, Ciervo C. 2018. A Slimhole Approach to Measuring Distributed Hydromechanical Strain in Fractured Geothermal Reservoirs. In: 43rd Workshop on Geothermal Reservoir Engineering. Stanford: Stanford University.

Benioff H. 1935. A linear strain seismograph. Bulletin of the Seismological Society of America. 25:238–309.

Correa J, Egorov A, Tertyshnikov K, Bona A, Pevzner R, Dean T, Freifeld B, Marshall S. 2017. Analysis of signal to noise and directivity characteristics of DAS VSP at near and far offsets

— A CO2CRC Otway Project data example. The Leading Edge. 36(12):994a1-994a7. doi:10.1190/tle36120994a1.1.

Daley T, Freifeld B, Ajo-Franklin J, Dou S, Pevzner R, Shulakova V, Kashikar S, Miller D, Götz J, Henninges J, et al. 2013. Field testing of fiber-optic distributed acoustic sensing (DAS) for subsurface seismic monitoring. The Leading Edge. 32:699–706. doi:10.1190/tle32060699.1.

Daley TM, Miller DE, Dodds K, Cook P, Freifeld BM. 2016. Field testing of modular borehole monitoring with simultaneous distributed acoustic sensing and geophone vertical seismic

profiles at Citronelle, Alabama. Geophys Prospect. 64(5):1318–1334. doi:10.1111/1365-2478.12324.

Dou S, Lindsey N, Wagner AM, Daley TM, Freifeld B, Robertson M, Peterson J, Ulrich C, Martin ER, Ajo-Franklin JB. 2017. Distributed Acoustic Sensing for Seismic Monitoring of The Near Surface: A Traffic-Noise Interferometry Case Study. Sci Rep. 7(1):11620. doi:10.1038/s41598-017-11986-4.

Eaid M, Innanen K. 2019. Coherent optical time domain relectometry: The theoretical basis for distributed acoustic sensing technologies. CREWES Research Report.

Eaid M, Li J, Innanen KA. 2018. Modeling the response of shaped DAS fibres to microseismic moment tensor sources. SEG Technical Program Expanded Abstracts 2018.:4698–4702. doi:10.1190/segam2018-2998378.1.

Evenden BS, Stone DR, Anstey NA. 1971. Seismic prospecting instruments. Berlin: Gebrueder Borntraeger.

Fenton MM, Waters EJ, Pawley SM, Atkinson N, Utting DJ, Mckay K. 2013. Surficial geology of Alberta.

Foti S, Lai C, Rix GJ, Strobbia C. 2014. Surface Wave Methods for Near-Surface Site Characterization. 1st Edition. London: CRC Press.

Hall K, Innanen K, Lawton D. 2022. The croissant: a smaller, fluffier, flakier pretzel. CREWES Research Report .

Hall KW, Bertram KL, Innanen KA, Lawton DC. 2023. Testing smaller permanent multicomponent optical fiber sensors . CREWES Research Report.

Hall KW, Innanen K, Lawton D. 2022. The croissant: a smaller, fluffier, flakier pretzel. CREWES Research Report.

Hall KW, Innanen KA, Lawton DC. 2020. Comparison of multi-component seismic data to fibre-optic (DAS) data. SEG Technical Program Expanded Abstracts 2020.:525–529. doi:10.1190/segam2020-3427754.1.

Hall KW, Innanen KA, Lawton DC. 2024. 9C DAS acquisition on the Pretzel and Croissant multi-component sensors. CREWES Research Report.

Harmon N, Rychert CA, Davis J, Brambilla G, Buffet W, Chichester B, Dai Y, Bogiatzis P, Snook J, van Putten L, et al. 2022. Surface deployment of DAS systems: Coupling strategies and comparisons to geophone data. Near Surface Geophysics. 20(5):465–477. doi:10.1002/nsg.12232.

Hou Y, Jiao R, Yu H. 2021. MEMS based geophones and seismometers. Sens Actuators A Phys. 318:112498. doi:10.1016/J.SNA.2020.112498. https://www.sciencedirect.com/science/article/pii/S0924424720318136.

Hu Q, Eaid M, Innanen K, Keating S, Cai X. 2024. Estimation of rock physics properties via full waveform inversion of vertical seismic profile data recorded by accelerometer and fiberoptic sensors. Geophys J Int. 237(2):805–817.

Hu Q, Innanen K, Macquet M. 2021. Rock physics analysis of well-log data. CREWES Research Report.

Innanen K. 2017 Aug 17. Determination of seismic-tensor strain from Helical Wound Cable-Distributed Acoustic Sensing cable with arbitrary and nested-helix winds. SEG Technical Program Expanded Abstracts 2017.:926–930. doi:10.1190/segam2017-17664060.1.

Innanen K, Lawton D, Hall K, Bertram K, Bertram M, Bland H. 2018. Design and deployment of a prototype multicomponent DAS sensor. CREWES Research Report.

Innanen KA. 2016. A geometrical model of DAS fibre response. CREWES Research Report.

Innanen KA, Lawton D, Hall K, Bertram KL, Bertram MB, Bland HC. 2019. Design and deployment of a prototype multicomponent distributed acoustic sensing loop array. SEG Technical Program Expanded Abstracts 2019.:953–957. doi:10.1190/segam2019-3216304.1.

Karrenbach M, Cole S, Ridge A, Boone K, Kahn D, Rich J, Silver K, Langton D. 2018. Fiber-optic distributed acoustic sensing of microseismicity, strain and temperature during hydraulic fracturing. Geophysics. 84(1):D11–D23. doi:10.1190/geo2017-0396.1.

Kearey P, Brooks M. 1987. Introduction to Geophysical Exploration. Blackwell Scientific Publications.

Kennett BLN. 2024. A Guide to the Seismic Wavefield as seen by DAS. The Australian National University.

Krebes E. 2019. Seismic Wave Theory. Cambridge University Press.

Kumar L, Sinha DP. 2008. From CMP to CRS - An Overview of Stacking Techniques of Seismic Data. In: 7th Biennial International Conference & Exposition on Petroleum Geophysics. Hyderabad: Society of Petroleum Geophysicists (SPG), India.

Kuvshinov BN. 2016. Interaction of helically wound fibre-optic cables with plane seismic waves. Geophys Prospect. 64(3):671–688. https://doi.org/10.1111/1365-2478.12303.

Labonne C, Sèbe O, Gaffet S. 2016. Seismic wavefield polarization – Part I: Describing an elliptical polarized motion, a review of motivations and methods. In: E3S Web of Conferences 12. i-DUST.

Lim Chen Ning I, Sava P. 2018. High-resolution multi-component distributed acoustic sensing. Geophys Prospect. 66(6):1111–1122. https://doi.org/10.1111/1365-2478.12634.

Lindsey NJ, Martin ER. 2021. Fiber-Optic Seismology. Annu Rev Earth Planet Sci. 49(Volume 49, 2021):309–336. doi:10.1146/annurev-earth-072420-065213. https://www.annualreviews.org/content/journals/10.1146/annurev-earth-072420-065213.

Lindsey NJ, Martin ER, Dreger DS, Freifeld B, Cole S, James SR, Biondi BL, Ajo-Franklin JB. 2017. Fiber-Optic Network Observations of Earthquake Wavefields. Geophys Res Lett. 44(23):11, 711–792, 799. doi:10.1002/2017GL075722. https://agupubs.onlinelibrary.wiley.com/doi/abs/10.1002/2017GL075722.

Lindsey NJ, Yuan S, Lellouch A, Gualtieri L, Lecocq T, Biondi B. 2020. City-Scale Dark Fiber DAS Measurements of Infrastructure Use During the COVID-19 Pandemic. Geophys Res Lett. 47(16):e2020GL089931. https://doi.org/10.1029/2020GL089931.

Lumens PGE. 2014. Fibre-optic sensing for application in oil and gas wells. [Eindhoven]: Technische Universiteit Eindhoven.

Macquet M, Kolkman-Quinn B, Lawton D. 2022. Carbon Management Canada CaMI Field Research Station: Advancing Monitoring Technologies for CCS. EAGE GeoTech 2022 Sixth EAGE Workshop on CO2 Geological Storage. https://api.semanticscholar.org/CorpusID:247879078.

Martin E, Biondi B, Karrenbach M, Cole S. 2017. Ambient Noise Interferometry from DAS Array in Underground Telecommunications Conduits. Vol. 2017. European Association of Geoscientists & Engineers. p. 1–5. http://www.earthdoc.org/publication/publicationdetails/?publication=88460.

Mateeva A, Lopez J, Potters H, Mestayer J, Cox B, Kiyashchenko D, Wills P, Grandi S, Hornman K, Kuvshinov B, et al. 2014. Distributed acoustic sensing for reservoir monitoring with vertical seismic profiling. Geophys Prospect. 62(4):679–692. https://doi.org/10.1111/1365-2478.12116.

Mechanics of Slender Structures. 2020. Mechanics of Materials: Strain. Boston University Mechanical Engineering. [accessed 2025 Jun 1]. https://www.bu.edu/moss/mechanics-of-materials-strain/.

Mestayer J, Cox B, Wills P, Kiyashchenko D, Lopez J, Costello M, Bourne S, Ugueto G, Lupton R, Solano G, et al. 2011 Jan. Field trials of distributed acoustic sensing for geophysical

monitoring. SEG Technical Program Expanded Abstracts 2011.:4253–4257. https://doi.org/10.1190/1.3628095.

O'DOHERTY RF, ANSTEY NA. 1971. REFLECTIONS ON AMPLITUDES*. Geophys Prospect. 19(3):430–458. doi:10.1111/j.1365-2478.1971.tb00610.x.

Papp B, Donno D, Martin JE, Hartog AH. 2017. A study of the geophysical response of distributed fibre optic acoustic sensors through laboratory-scale experiments. Geophys Prospect. 65(5):1186–1204. doi:10.1111/1365-2478.12471.

Sánchez Galvis I, Gonzalez-Alvarez H, Agudelo WM, Trad D, Sierra D. 2025. ElasWave3D: A GPU-accelerated 3D finite-difference elastic wave solver for complex topography using irregular subdomain index arrays. Comput Geosci. 205. doi:10.1016/j.cageo.2025.105994.

SEAFOM. 2024. Document No: SEAFOM Measuring Sensor Performance Document – (SEAFOM MSP-02 V2.0) DAS Parameter Definitions and Tests.

Shatalin S, Parker T, Farhadiroushan M. 2021. High Definition Seismic and Microseismic Data Acquisition Using Distributed and Engineered Fiber Optic Acoustic Sensors. In: Distributed Acoustic Sensing in Geophysics. (Geophysical Monograph Series). p. 1–32. https://doi.org/10.1002/9781119521808.ch1.

Shatalin S, Treschikov V, Rogers A. 1998. Interferometric optical time-domain reflectometry for distributed optical-fiber sensing. Appl Opt. 37:5600–5604. doi:10.1364/AO.37.005600.

Shearer PM. 2019. Introduction to Seismology. 3rd ed. Cambridge: Cambridge University Press. https://www.cambridge.org/core/product/C1471C1B553C05997E2BC7EB26D4C26D.

Sheriff RE, Geldart LP. 1995. Exploration Seismology. 2nd ed. Cambridge: Cambridge University

Press.

https://www.cambridge.org/core/product/CC00727A219943E62F6FF01426DBA9D2.

Spikes KT, Tisato N, Hess TE, Holt JW. 2019. Comparison of geophone and surface-deployed distributed acoustic sensing seismic data. Geophysics. 84(2):A25–A29. https://doi.org/10.1190/geo2018-0528.1.

Takekawa J, Mikada H, Xu S, Uno M, Kamei S, Kishida K, Azuma D, Aoyanagi M, Tanaka N, Ichikawa H. 2022. A new DAS sensor prototype for multicomponent seismic data. The Leading Edge. 41(5):338–346. https://doi.org/10.1190/tle41050338.1.

Tang J, Cai L, Li C, Yang M, Guo H, Gan W. 2021. Distributed acoustic sensors with wide frequency response based on UWFBG array utilizing dual-pulse detection. Optical Fiber Technology. 61:102452. doi:10.1016/J.YOFTE.2021.102452. [accessed 2025 Aug 28]. https://www.sciencedirect.com/science/article/pii/S1068520021000018.

Thevenaz L. 2011. Advanced Fiber Optics. 1st Edition. Thevenaz L, editor. New York: EPFL Press.

Wang H, Fratta D, Lord N, Zeng X, Coleman T. 2018. Distributed acoustic sensing (DAS) field trials for near-surface geotechnical properties, earthquake seismology, and mine monitoring. In: SEG Technical Program Expanded Abstracts 2018. Society of Exploration Geophysicists. (SEG Technical Program Expanded Abstracts). p. 4953–4957. https://doi.org/10.1190/segam2018-2997833.1.

Willis M. 2022. Distributed Acoustic Sensing for Seismic Measurements – What Geophysicists and Engineers Need to Know.

Wong J. 2023. Picking and fitting of first-break times measured on Gabor transforms of uncorrelated Vibroseis VSP signals . CREWES Research Report.

Yang J, Shragge J, Jin G. 2021. 4D DAS fiber-coupling effects in freezing near-surface ground conditions. In: First International Meeting for Applied Geoscience & Energy Expanded Abstracts. Society of Exploration Geophysicists. (SEG Technical Program Expanded Abstracts). p. 477–482. https://doi.org/10.1190/segam2021-3582508.1.

Yilmaz Ö. 2001. Seismic Data Analysis: Processing, Inversion, and Interpretation of Seismic Data. Society of Exploration Geophysicists. https://doi.org/10.1190/1.9781560801580.

Zhan Z. 2020. Distributed Acoustic Sensing Turns Fiber-Optic Cables into Sensitive Seismic Antennas. Seismological Research Letters. 91(1):1–15. https://doi.org/10.1785/0220190112.

Appendix

Croissant Loop Path Function

```
function [x,y,z,tx,ty,tz] = ParametricTrajectoryCorissant(sensor)
%This function generates the Croissant trajectory coordinates from the interrogator
%passing through the 3 sensors oriented in the H1, H2 and V components. The
%fiber is discretized every 'interval' value.
w = 1.0;
                            % Width
h = (4.0 * 2.54) / 100.0;
                            % Height in meters
r = h / 2;
                            % Radius
s = w - h;
                            % Straight segment length
c = 0.01;
                            % Constant for z variation
                            %Parametrization values in terms of distance
d1 = 0;
d2 = s * sqrt(1 + c^2);
d3 = d2 + pi * r;
d4 = d3 + s * sqrt(1 + c^2);
d5 = d4 + pi * r;
n_wraps = 14; %Number of wraps along the frame
d wrap = n wraps*d5; %distance in meters of the cable/fiber for the n wraps
interval = 0.005; %Interval of discretization in meters
di = 0:interval:d_wrap; %distance di start at zero and will increase each interval
value until reaches the distance d wrap
PLOT = false; %Make figures if PLOT = true
switch sensor
        case 1
            [x,y,z,tx,ty,tz] = mk_croissant_sensor1(di,r,s,c,h,w,PLOT); %If 1, it
will plot just Croissant 1
        case 2
            [x,y,z,tx,ty,tz] = mk_croissant_sensor2(di,r,s,c,h,w,PLOT); %If 2, it
will plot just Croissant 2
            [x,y,z,tx,ty,tz] = mk_croissant_sensor3(di,r,s,c,h,w,PLOT); %If 3, it
will plot just Croissant 3
        otherwise
            [x,y,z,tx,ty,tz] = mk_croissant_sensors(di,r,s,c,h,w,interval,PLOT);
%Otherwise, it will plot just Croissanttrajectory
end
end
%% Functions
function plot croissant_loop(x,y,z,s)
%function plot_croissant_loops(x,y,z,s)
% plot3 x,y,z coordinate vectors with title = s
    figure;
    plot3(x,y,z);
    hold
    plot3(x(1),y(1),z(1),'ro')
```

```
plot3(x(end),y(end),z(end),'r*')
    xlabel('x');
    ylabel('y');
    zlabel('z');
    title(s);
    axis equal;
end %end function plot_croissant_loop
function plot_croissant_sensor(x1,y1,z1,x2,y2,z2,x3,y3,z3,s)
    figure;
    plot3(x1,y1,z1,'r');
    hold
    plot3(x1(1),y1(1),z1(1),'r*');
    plot3(x1(end),y1(end),z1(end),'ro');
    plot3(x2,y2,z2,'k');
    plot3(x2(1),y2(1),z2(1),'k*');
    plot3(x2(end),y2(end),z2(end),'ko');
    plot3(x3,y3,z3,'b');
    plot3(x3(1),y3(1),z3(1),'b*');
    plot3(x3(end),y3(end),z3(end),'bo');
    xlabel('x');
    ylabel('y');
    zlabel('z');
    title(s);
    axis equal:
end %end function plot_croissant_sensor
function plot_croissant_sensors(x,y,z,s)
    figure
    plot3(x,y,z);
    xlabel('x');
    ylabel('y');
    zlabel('z');
    title(s);
    axis equal;
end %end function plot_croissant_sensors
function [x,y,z,tx,ty,tz] = mk_croissant_loop_carla(di,r,s,c,plane) %This is the
parametrization for the Croissant
d1 = 0;
d2 = s * sqrt(1 + c^2);
d3 = d2 + pi * r;
d4 = d3 + s * sqrt(1 + c^2);
d5 = d4 + pi * r;
d = mod(di, d5);
x1 = (d >= d1) .* (d < d2) .* (d ./ sqrt(1 + c^2));
x2 = (d \ge d2) .* (d < d3) .* (s + r * sin((d - d2) / r));
x3 = (d >= d3) .* (d < d4) .* (s - (d - d3));
x4 = (d >= d4) .* (-r * sin((d - d4) / r));
y1 = (d >= d1) .* (d < d2) .* (r);
```

```
y2 = (d >= d2) .* (d < d3) .* (r * cos((d - d2) / r));
y3 = (d >= d3) .* (d < d4) .* (-r);
y4 = (d >= d4) .* (-r * cos((d - d4) / r));
x = x1 + x2 + x3 + x4;
y = y1 + y2 + y3 + y4;
z = (c * di / sqrt(1 + c^2));
%Parametrization of the tangent vector
tx1 = (d >= d1) .* (d < d2) .* (1 / sqrt(1 + c^2));
tx2 = (d >= d2) .* (d < d3) .* ((cos((d - d2) / r)));
tx3 = (d >= d3) .* (d < d4) .* ((-sqrt(1 + c^2)) / sqrt(1 + 2*c^2));
tx4 = (d >= d4) .* (-cos((d - d4) / r));
ty1 = (d >= d1) .* (d < d2) .* (0);
ty2 = (d >= d2) .* (d < d3) .* (-sin((d - d2) / r));
ty3 = (d >= d3) .* (d < d4) .* (0);
ty4 = (d >= d4) .* (sin((d - d4) / r));
tz1 = (d >= d1) .* (d < d2) .* (c/sqrt(1 + c^2));
tz2 = (d >= d2) .* (d < d3) .* (0);
tz3 = (d >= d3) .* (d < d4) .* (c/ sqrt(1 + 2*c^2));
tz4 = (d >= d4) .* (0);
tx = tx1 + tx2 + tx3 + tx4;
ty = ty1 + ty2 + ty3 + ty4;
tz = tz1 + tz2 + tz3 + tz4;
% Switch planes based on the provided argument
switch (plane)
    case 'xy' % DONE
        % No change, use original x, y, z
    case 'xz'
        % Switch y and z
        temp = y; % Use a temporary variable for swapping
        y = z;
        z = temp;
        tempt = ty;
        ty = tz;
        tz = tempt;
    case 'yx'
        % Switch x and y
        temp = x;
        x = y;
        y = temp;
        tempt = tx;
        tx = ty;
        ty = tempt;
    case 'yz'
        % Switch x and z
        temp = x;
        x = z;
```

```
z = temp;
        tempt = tx;
        tx = tz;
        tz = tempt;
    case 'zy'
        % Switch z and y
        temp = z;
        z = y;
        y = temp;
        tempt = tz;
        tz = ty;
        ty = tempt;
    case 'zx'
        % Switch z and x
        temp = z;
        z = x;
        x = temp;
        tempt = tz;
        tz = tx;
        tx = tempt;
    otherwise
        error(["Error: Unknown plane '" plane "'\n"]);
end
end
function [xp,yp,zp] = rotate_coords(x,y,z,a,theta)
%function [x,y,z] = rotate_coords(x,y,z,a,theta)
% rotate x,y,z by angle theta around axis a = 'x','y','z'
switch a
    case 'x'
        xp = x;
        yp = y*cos(theta) -z*sin(theta);
        zp = y*sin(theta) +z*cos(theta);
    case 'y'
        xp = x*cos(theta) + z*sin(theta);
        yp = y;
        zp = -x*sin(theta) + z*cos(theta);
    case 'z'
        xp = x*cos(theta) - y*sin(theta);
        yp = x*sin(theta) + y*cos(theta);
        zp = z;
    otherwise
        error(["Coordinate rotation error: Unkown axis '" a "'\n"]);
end %end switch a
end
function [x,y,z,tx,ty,tz] = mk_croissant_sensor1(di,r,s,c,h,w,PLOT)
% Make a 3C croissant sensor path
   %H1 component as per Figure 8, Hall et al, 2023
    [x1,y1,z1,tx1,ty1,tz1] = mk_croissant_loop_carla(di,r,s,c,'xy');
```

```
z1 = z1+h;
    %V component
    [x2,y2,z2,tx2,ty2,tz2] = mk_croissant_loop_carla(di,r,s,c,'yz');
    x2 = x2+h;
    %H2 component
    [x3,y3,z3,tx3,ty3,tz3] = mk_croissant_loop_carla(di,r,s,c,'yx');
    [x3,y3,z3] = rotate_coords(x3,y3,z3,'z',2*pi);
    [tx3,ty3,tz3] = rotate_coords(tx3,ty3,tz3,'z',2*pi);
    y3 = y3 + h;
    z3 = z3 + h;
    if (PLOT)
        plot_croissant_sensor(x1,y1,z1,x2,y2,z2,x3,y3,z3,'Sensor 1');
    end
   x = [x1 \ x2 \ x3];
    y = [y1 \ y2 \ y3];
    z = [z1 \ z2 \ z3];
   tx = [tx1 tx2 tx3];
    ty = [ty1 ty2 ty3];
    tz = [tz1 tz2 tz3];
   % if (PLOT)
   %
          plot_croissant_loop(x,y,z,'Sensor 1');
    % end
end
function [x,y,z,tx,ty,tz] = mk_croissant_sensor2(di,r,s,c,h,w,PLOT)
% Make a 3C croissant sensor path
    %H1 component as per Figure 8, Hall et al, 2023
    [x1,y1,z1,tx1,ty1,tz1] = mk_croissant_loop_carla(di,r,s,c,'xy');
    [x1,y1,z1] = rotate_coords(x1,y1,z1,'z',pi);
    [tx1,ty1,tz1] = rotate_coords(tx1,ty1,tz1,'z',pi);
    x1 = x1+w-h;
    z1 = z1+h;
   %V component
    [x2,y2,z2,tx2,ty2,tz2] = mk_croissant_loop_carla(di,r,s,c,'yz');
    x2 = x2+h;
    %H2 component
    [x3,y3,z3,tx3,ty3,tz3] = mk_croissant_loop_carla(di,r,s,c,'yx');
    y3 = y3 + h;
   z3 = z3 + h;
        plot_croissant_sensor(x1,y1,z1,x2,y2,z2,x3,y3,z3,'Sensor 2');
    end
    x = [x1 \ x2 \ x3];
```

```
y = [y1 \ y2 \ y3];
    z = [z1 \ z2 \ z3];
    tx = [tx1 tx2 tx3];
    ty = [ty1 ty2 ty3];
    tz = [tz1 tz2 tz3];
   % if (PLOT)
    %
          plot_croissant_loop(x,y,z,'Sensor 2');
    % end
end
function [x,y,z,tx,ty,tz] = mk_croissant_sensor3(di,r,s,c,h,w,PLOT)
% Make a 3C croissant sensor path
    %H2 component as per Figure 8, Hall et al, 2023
    [x1,y1,z1,tx1,ty1,tz1] = mk_croissant_loop_carla(di,r,s,c,'yx');
    [x1,y1,z1] = rotate coords(x1,y1,z1,'z',pi);
    [tx1,ty1,tz1] = rotate coords(tx1,ty1,tz1,'z',pi);
    y1 = y1 + w;
    z1 = z1 + h;
    %V component
    [x2,y2,z2,tx2,ty2,tz2] = mk croissant loop carla(di,r,s,c,'zx');
    [x2,y2,z2] = rotate_coords(x2,y2,z2,'z',pi/2);
    [tx2,ty2,tz2] = rotate_coords(tx2,ty2,tz2,'z',pi/2);
    y2 = y2+1.5*h;
    %H1 component
    [x3,y3,z3,tx3,ty3,tz3] = mk_croissant_loop_carla(di,r,s,c,'xy');
    [x3,y3,z3] = rotate_coords(x3,y3,z3,'z',pi);
    [tx3,ty3,tz3] = rotate coords(tx3,ty3,tz3,'z',pi);
    x3 = x3 + w - h;
    z3 = z3 + h;
    if (PLOT)
        plot_croissant_sensor(x1,y1,z1,x2,y2,z2,x3,y3,z3,'Sensor 3');
    end
    x = [x1 \ x2 \ x3];
    y = [y1 \ y2 \ y3];
    z = [z1 \ z2 \ z3];
    tx = [tx1 tx2 tx3];
    ty = [ty1 ty2 ty3];
    tz = [tz1 tz2 tz3];
   % if (PLOT)
    %
          plot_croissant_loop(x,y,z,'Sensor 3');
    % end
end
function [x,y,z,tx,ty,tz] = mk_croissant_sensors(di,r,s,c,h,w,interval,PLOT)
```

```
[x1,y1,z1,tx1,ty1,tz1] = mk_croissant_sensor1(di,r,s,c,h,w,PLOT);
[x2,y2,z2,tx2,ty2,tz2] = mk_croissant_sensor2(di,r,s,c,h,w,PLOT);
[x3,y3,z3,tx3,ty3,tz3] = mk_croissant_sensor3(di,r,s,c,h,w,PLOT);
%translate sensors
x2 = x2 - 10.0;
y3 = y3 - 10.0;
%make connectors
cxs = 10.0;
cys = 00.0;
czs = h;
cx23 = 0;
cy23 = 0;
cz23 = h;
cx31 = 0;
cy31 = -10;
cz31 = h;
cxe = cxs;
cye = cys;
cze = czs;
vectorx s2 = cxs:-interval:x2(1);
vectory s2 = zeros(size(vectorx s2));
vectorz_s2 = zeros(size(vectorx_s2));
[tx_s2, ty_s2, tz_s2] = tangent_straight_segments(vectorx_s2, vectory_s2,
vectorz_s2);
vectorx 223 = x2(end):interval:cx23;
vectory_223 = zeros(size(vectorx_223));
vectorz 223 = zeros(size(vectorx 223));
[tx_223, ty_223, tz_223] = tangent_straight_segments(vectorx_223, vectory_223,
vectorz 223);
vectory_233 = cy23:interval:y3(1);
vectorx_233 = zeros(size(vectory_233));
vectorz_233 = zeros(size(vectory_233));
[tx_233, ty_233, tz_233] = tangent_straight_segments(vectorx_233, vectory_233,
vectorz_233);
vectory_31 = y3(end):interval:y1(1);
vectorx 31 = zeros(size(vectory 31));
vectorz_31 = zeros(size(vectory_31));
[tx 31, ty 31, tz 31] = tangent straight segments(vectorx 31, vectory 31,
vectorz_31);
vectorx 1e = x1(end):interval:cxe;
vectory_1e = zeros(size(vectorx_1e));
vectorz 1e = zeros(size(vectorx 1e));
[tx_1e, ty_1e, tz_1e] = tangent_straight_segments(vectorx_1e, vectory_1e,
vectorz_1e);
```

```
x = [vectorx_s2 x2 vectorx_223 vectorx_233 x3 vectorx_31 x1 vectorx_1e];
y = [vectory_s2 y2 vectory_223 vectory_233 y3 vectory_31 y1 vectory_1e];
z = [vectorz_s2 z2 vectorz_223 vectorz_233 z3 vectorz_31 z1 vectorz_1e];
tx = [tx_s2 tx_2 tx_223 tx_233 tx_3 tx_31 tx_1 tx_1e];
ty = [ty_s2 ty2 ty_223 ty_233 ty3 ty_31 ty1 ty_1e];
tz = [tz_s2 tz2 tz_223 tz_233 tz3 tz_31 tz1 tz_1e];
function [tx, ty, tz] = tangent_straight_segments(x, y, z)
% Preallocate tangent vectors
tx = zeros(size(x));
ty = zeros(size(y));
tz = zeros(size(z));
for ii = 1:length(x)-1
    % Compute the differences between consecutive points
    dx = x(ii+1) - x(ii);
    dy = y(ii+1) - y(ii);
    dz = z(ii+1) - z(ii);
    % Normalize the tangent vectors
    tlength = sqrt(dx^2 + dy^2 + dz^2);
    % Compute unit tangent vectors and scale by di
    tx(ii) = dx / tlength;
    ty(ii) = dy / tlength;
    tz(ii) = dz / tlength;
end
end
%rotate sensors
[x,y,z] = rotate\_coords(x,y,z,'z',pi/4);
[tx,ty,tz] = rotate_coords(tx,ty,tz,'z',pi/4);
if (PLOT)
    plot_croissant_sensors(x,y,z,'Croissant Fiber Loop')
end
end %end mk_croissant_sensors
```